

**A framework to assess the climate impact of non-CO₂ emissions
of Switzerland - Executive and Technical Summaries**

Zürich, December 18, 2024

Commissioned by the Federal Office for the Environment (FOEN)

Impressum

Imprint

Commissioned by: Federal Office for the Environment (FOEN), Climate Division, CH 3003 Bern

The FOEN is an agency of the Federal Department of the Environment, Transport, Energy and Communications (DETEC).

Contractor: Prof. Dr. Mazzotti Marco, ETH Zürich

Author: Vittoria Bolongaro, Viola Becattini, Marco Mazzotti

FOEN support: Martin Jiskra (FOEN), Roger Ramer (FOEN), Regine Röthlisberger (FOEN), Thomas Kellerhals (FOEN), Daniel Bretscher (Agroscope), Christoph Ammann (Agroscope), Theo Rindlisbacher (FOCA)

Note: This study/report was prepared under contract to the Federal Office for the Environment (FOEN). The contractor bears sole responsibility for the content.

1 Introduction

To limit global warming to 1.5°C, global CO₂ emissions have to decrease by half by 2030 and reach net-zero by 2050. In compliance with the Paris Agreement, the Swiss government has adopted a long-term climate strategy in 2021.

In June 2023, the Climate and Innovation law (Klima- und Innovationsgesetz, KIG) was approved in a referendum, defining Switzerland's long-term efforts to react to climate change. This law sets the target of net-zero "climate effects" by 2050 (Art. 3.1b). This formulation refers to the wording in the indirect counter proposal to the glacier initiative (indirekter Gegenvorschlag), which sets the net-zero goal that the *climate effect* of man-made GHG emissions within Switzerland has to be zero.

The long-term climate strategy of Switzerland lays out scenarios to reach the *net-zero* target by primarily reducing GHG emissions in all sectors. Despite these GHG emissions reductions, there will remain hard-to-abate emissions primarily from cement production, waste incineration and agriculture that have to be removed at the point source by carbon capture and storage (CCS, fossil or process emissions) or balanced by negative emission technologies (NET).

The Energy Perspectives 2050+ (EP2050+) estimated a total demand of 12 Mio tCO₂-eq of hard-to-abate emissions that have to be addressed by CCS and NET. This includes a demand of 5 Mio tCO₂-eq from the agricultural sector, which has been calculated from the conversion of non-CO₂ emissions, namely methane and nitrous oxide, using the GWP₁₀₀ metric.

In the last years, shortcomings associated to the use of the GWP₁₀₀ metric to convert short-lived, and long-lived, GHG into CO₂-eq have been analysed and discussed in the scientific literature, and alternative approaches such as the GWP* model were developed. The Swiss Academy of Sciences (SCNAT) has published a communication in 2022¹, concluding that "die Formulierung des langfristigen Klimaziels der Schweiz, die Treibhausgasemissionen bis 2050 auf netto null zu senken, müsste präzisiert werden. Abhängig davon, mit welcher Metrik CO₂-Äquivalent-Emissionen berechnet werden, sind unterschiedlich grosse Mengen negativer CO₂-Emissionen nötig, um netto null zu erreichen". This statement indicates that the Swiss long-term climate goals, to reach net-zero GHG emission by 2050 should be further specified, also considering the effect of different CO₂ equivalence metrics when calculating Carbon Dioxide Removal (CDR) requirements.

The goal of this study is to assess the climate impact of Switzerland's long-term climate strategy by taking into account relevant emission reduction pathways, and related agriculture and aviation policies.

The specific objectives of the study, as spelled out in the project description, are the following four.

Objective 1 – Conceptual framework [Milestone 1, December 2022]

Establishing a conceptual and (simplified) modeling framework, in which to assess the climate impact of Swiss emissions from different sectors, particularly agriculture and aviation. This will be done by:

- modeling the correlation between GHG emissions and their concentration in the atmosphere;
- establishing the relationship between Swiss GHG emissions, their contribution to altering the GHG concentration in the atmosphere, and their impact on radiative forcing;
- clarifying the difference between CO₂ emissions (long-lived climate pollutants) and non-CO₂ emissions (short-lived climate pollutants);
- assessing the accuracy of the simplified modeling framework by comparison with results from metrics calculation and available climate models, e.g., FAIR model.

Objective 2 – CO₂-equivalence for non-CO₂ emissions [Milestone 2, March 2023]

Establishing CO₂-equivalence between non-CO₂ emissions and CO₂-emissions for the two sectors of interest, i.e., agriculture and aviation. This will be done by:

- considering different time horizons (not only from 1990 to 2060 as in the EP 2050+, but also extending backward in the past, and further into the future);
- considering different reference conditions (1990 emissions levels, pre-industrial emissions levels, no emissions);
- using different scenarios, e.g., Net Zero 2050 Standard, Business as Usual as to EP 2050+, among others;
- applying different equivalence metrics, i.e., GWP₁₀₀, GWP₂₀, GWP* and LWE;
- developing and implementing methodologies relevant for the different approaches, that are used not only in this study, but possibly also in future studies based on scenario analysis.

Objective 3 – Demand for NETs [Milestone 3, June 2023]

Determining the demand for Negative CO₂ Emissions (NETs) to compensate for remaining GHG emissions for all the different cases considered above. This will be done by:

- targeting the objective of net-zero GHG emissions by 2050, employing the equivalence metrics introduced in the previous milestones;
- assessing the impact of different equivalence metrics on CDR requirements and on the climate
- assigning different time horizons and time windows for the compensation;

Objective 4 – Climate strategy implications [Milestone 4, October 2023]

Assessment of the implications for Swiss climate policy building on established climate strategies (i.e. longterm climate strategy, sector strategies for aviation and agriculture). This will be done by:

- taking into consideration the different objectives above, i.e., (i) net-zero GHG emissions by 2050 referring to the Swiss long-term climate strategy and (ii) net-zero climate forcing of emissions by 2050 referring to the climate and innovation law;
- making a comparative assessment of the policies implications of the use of the different approaches, i.e., models and metrics, in defining the CO₂-equivalence for non-CO₂ emissions in the two sectors considered;
- exploiting exchanges and discussions with the sectoral experts and with BAFU, that should take place in the second part of the project) to fully appreciate the opportunities and the challenges created by the use of the current metric in defining climate objectives, as compared to those yielded by the utilization of the alternative approaches considered in thus study.
- evaluating the different approaches, i.e. metrics, models and time references while considering recent discussions and recommendations on metrics of IPCC AR6.
- providing a recommendation to FOEN for the best suitable method for quantification of NET demand to achieve the net zero target as defined in the longterm climate strategy and the climate and innovation law and discussing the implications for Swiss climate policy, in particular for the two sectors (agriculture and aviation).

This report documents the results achieved in the scope of the activities aimed at reaching the four project milestones.

Part I

Milestone 1 - Conceptual modeling framework

2 Generalities of climate modeling

Climate models are computational tools used to simulate and predict various aspects of the Earth's climate system, including the impact of different pollutants (called also climate forcers) on the climate.

Global Climate Models (GCMs) simulate the entire Earth's climate system, dividing the planet into a three-dimensional grid, representing atmosphere, oceans, land, and ice. GCMs incorporate physical equations to simulate atmospheric processes, ocean circulation, heat transfer, and other climate-related phenomena. Regional Climate Models (RCMs) focus instead on specific regions or smaller geographic areas, providing a higher spatial resolution and assessing local or regional climate impacts and variability.

Earth System Models (ESMs) are an extension of GCMs that include additional components to represent the Earth's carbon cycle, ecosystems, and other biogeochemical processes. ESMs integrate various Earth system components to simulate and study climate and environmental processes, helping our understanding of the Earth's complex climate system and its responses to external factors. ESMs incorporate complex models for the atmosphere, oceans, land surface, ice sheets, and biogeochemical cycles; these complex models are designed to simulate the Earth's climate system and provide valuable insights into past, present, and future climate dynamics. As stated in Leach et al.², "while ESMs are integral to our current understanding of how the climate system responds to greenhouse gas (GHG) and aerosol emissions and provide the most comprehensive projections of what a future world might look like, they are so computationally expensive that only a limited set of numerical experiments can be run during a CMIP (Coupled Model Intercomparison Project). This limitation indicates the important role of simpler models to provide probabilistic assessments and to explore additional hypotheses and scenarios. These models, often referred to as simple climate models (SCMs), are typically calibrated to emulate the response of more complex models."

SCMs have the advantage of being considerably less complex than ESMs, for example by parameterizing many processes, and computationally less demanding.² "Simple climate models can be valuable if they are able to replicate aspects of complex fully coupled earth system models"³, e.g., by providing a good replication of the emissions-concentration-radiative forcing-temperature response pathways.

In this work, we focus on identifying a minimum level of structural complexity in the model, thus creating a transparent Simplified Linear Climate Model (SLCM), able to emulate other well-established SCMs, such as FAIR (Finite Amplitude Impulse Response climate model).

The fundamentals of the modeling approach followed in this study are summarized here:

1. The model proposed here determines the climate impacts of climate forcers (CFs, e.g., greenhouse gases, GHGs), both long-lived CFs (LLCFs) and short-lived CFs (SLCFs), during a specified time span through the following chain of causality (Figure 1):
 - A climate forcer identified with the label i (i.e., CF_i) alters its concentration (c_i) in the atmosphere, which is considered well-mixed, due to its emissions (E_i); both c_i and E_i are function of time. Formally, the relation between the two quantities can be expressed by writing $c_i(t) = H_i(E_i(t))$, where $H_i(\cdot)$ is a functional, integral operator.
 - CF_i causes radiative forcing (F_i); the latter is a function of the concentration of CF_i . Such relationship can be expressed as $F_i(t) = f_i(c_i)$, where $f_i(\cdot)$ is a monotonically increasing function.

In this study, indirect effects are not considered, hence the forcing of a pollutant i is only a function of the atmospheric concentration of i and does not depend on those of other pollutants j .

- Assuming superposition of effects, the overall radiative forcing is the sum of the contributions due to all CFs, plus the contributions of other climate effects, for which one can establish a direct relationship between radiative forcing and extent of the activity causing climate impact, e.g., the generation of cirrus clouds by aviation. This relationship links directly the extent of such activity to radiative forcing, i.e., $F_j(t) = H'_j(E_j(t))$, where $H'_j(\cdot)$ would be a functional operator different than the previous.
2. Through the chain of causality and subject to the assumptions inherent in the SLCM, an explicit equivalence between emissions of non-CO₂ pollutants ($E_i(t)$) and CO₂ ($E_C(t)$) can be established. This is the principle of the LWE (Linear Warming Equivalent) model.
 3. Let us consider the climate impacts of individual emitters, countries or sectors, whereby the corresponding emissions of the i -th GHG are a small percentage of the global emissions (i.e., in the order of a few percent or less). Then such emissions can be considered as a perturbation of all the other global emissions, which leads to a differential variation of the corresponding i -th concentration (i.e., Δc_i) which in turn yields a differential variation of the radiative forcing caused by that GHG (ΔF_i).
 4. Based on these considerations, the definition of the LWE can be revised and interpreted as the equivalence between the forcing differential of the CF _{i} and that of the CO₂ (i.e., $\Delta F_i = \Delta F_C$), both calculated with respect to a background forcing caused by the global emissions and the associated evolution of global concentrations. The background does not need to be defined quantitatively for such "differential equivalence" concept to be applicable.
 5. For the aviation sector specifically, it is important to consider that its climate impact meaningfully arises from both its GHGs emissions and the "non-GHG effects" generated by the release of cirrus clouds. The radiative forcing resulting from this latter climate effect is not a formation of the climate forcer's concentration, but is determined instead by local conditions (e.g., meteorological background, location and time of the emissions). As we are interested in the average impact of (Swiss) aviation on the climate, rather than the radiative effect of a specific flight, we can simplify this issue of heterogeneity by employing an averaging approach, as previously assumed in relevant state of the art references⁴⁻⁶ and global climate models. Further explanations are provided in Section 3.2.2.

A schematic depicting the modeling approach followed in this study is shown in Figure 1.

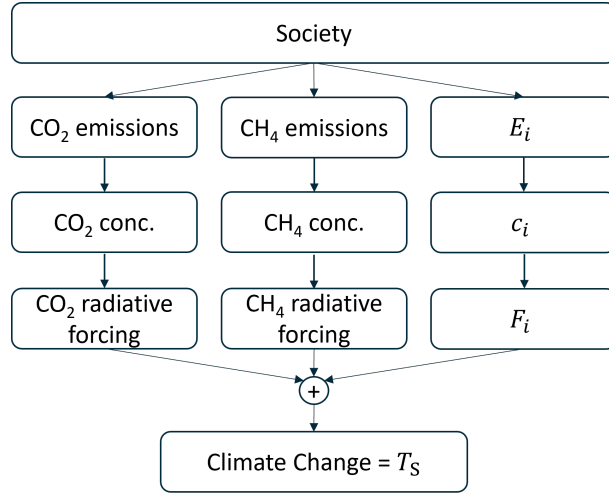


Figure 1. Schematic of the "chain of causality" modeling approach (inspired by earlier literature⁷). The following elements of the chain can be observed: (i) the emitters (i.e. society), (ii) the emissions generated, (iii) the resulting atmospheric concentration levels, (iv) the corresponding, specific radiative forcings, (v) the total radiative forcing, where specific forcing from different GHGs are summed up by exploiting the superposition principle, and (vi) the final temperature anomaly, i.e., the global warming as manifestation of climate change.

3 Model equations

3.1 From emissions to atmospheric concentrations

3.1.1 The case of a generic non-CO₂ GHG

All non-CO₂ GHGs, either LLCF or SLCF, are assumed to be decaying in the atmosphere following a first-order kinetics independent of the composition of the atmosphere itself. Hence the evolution of their concentration is characterized by a single characteristic time, τ_i , that is assumed to be independent of the atmosphere's composition, and is described by the following single order ordinary differential equation (ODE):

$$\frac{dc_i}{dt} = -\frac{c_i}{\tau_i} + E_i(t) \quad (1)$$

where $E_i(t)$ is defined as mass (or moles) of i emitted, per unit time and unit volume of the receiving atmosphere. Such equation is integrated once for the initial condition $c_i(0) = c_{i,0}$, thus obtaining:

$$c_i(t) = c_{i,0} \exp\left(-\frac{t}{\tau_i}\right) + \int_0^t E_i(t') \exp\left(\frac{t' - t}{\tau_i}\right) dt' \quad (2)$$

$$\stackrel{E=const}{=} c_{i,0} \exp\left(-\frac{t}{\tau_i}\right) + E_i \tau_i \exp\left(-\frac{t}{\tau_i}\right) \left[\exp\left(\frac{t}{\tau_i}\right) - 1 \right]$$

The evolution of the concentration is given by two contributions, namely the initial concentration decaying exponentially with a characteristic time, τ_i , and the convolution integral of the emissions' profile. The right hand side of the last equation is the $H_i(\cdot)$ functional operator that acts on the function $E_i(t)$, as mentioned in the previous section.

GHGs with a characteristic decay time around that of methane (i.e., about 10 years, and generally less than 20 years) are considered short-lived, in brief SLCF; those with a higher value are considered long-lived, in brief LLCF (e.g., N₂O). The difference in the behavior of LLCFs and SLCFs is only quantitative; they can

both be described by exactly the same Equation (1) with the only difference being their characteristic time τ_i .

It is worth underlining that the evolution of the CF_i in time depends on its initial concentration $c_{i,0}$, which is chosen as starting point of the integration, and on the evolution of its global emissions from that initial time to any following time of interest, t . It is also worth noting that the starting time can be very far in the past (e.g., before anthropogenic emissions of GHGs have become relevant) or much closer in time (e.g., either at a time where climate policies have been introduced, or at a point in time that is considered to be an important reference). Further discussion on the choice and implications of the reference, initial time point are presented in Appendix B.3.

3.1.2 The case of carbon dioxide

Carbon dioxide behaves differently than the GHGs described in the previous section: it is emitted into the atmosphere only, but it partitions itself in four different compartments, namely the atmosphere (where it contributes to the overall radiative forcing, and therefore climate change), the shallow and deep oceans, and the biota. Carbon dioxide does not decay, but it is conserved, while it is exchanged among compartments. Such transfer can be described with acceptable accuracy as a function of the CO_2 concentration in each compartment through linear transfer relationships. As a consequence, the CO_2 distribution in the four compartments is characterized by four concentrations (i.e., one for each compartment) and its evolution is described by a system of four first order ODEs. In vector form, this reads:

$$\frac{d\mathbf{c}}{dt} = \mathbb{A}\mathbf{c} + \mathbf{E}(t) \quad (3)$$

Whereby:

- the first component of the four-dimensional vector \mathbf{c} is the CO_2 concentration in the atmosphere. This scalar will be called $c_C(t)$ in the following sections;
- the first component of the four-dimensional vector \mathbf{E} is the only non-zero component, which represents the CO_2 emissions into the atmosphere. This scalar will be called $E_C(t)$ in the following sections;
- because CO_2 is conserved through the exchanges among the four compartments, the sum of the CO_2 concentrations in the four compartments is constant in time. Therefore, the four ODEs are not linearly independent and the matrix of coefficients \mathbb{A} has rank 3 and zero determinant. It follows that one of the four eigenvalues of the matrix \mathbb{A} is zero; the other three eigenvalues are real and negative. The zero eigenvalue is referred to as λ_0 in this study.

The evolution of \mathbf{c} in time is given by the solution of Equation (3), i.e., by:

$$\mathbf{c}(t) = \exp(t\mathbb{A})\mathbf{c}_0 + \int_0^t \exp((t-t')\mathbb{A})\mathbf{E}(t')dt' \quad (4)$$

where \mathbf{c}_0 is the vector consisting of the initial CO_2 concentrations in the four compartments (we'll call $c_{C,0}$ the corresponding initial value in the atmospheric compartment). Note that the exponential matrix is calculated as:

$$\exp(t\mathbb{A}) = \mathbb{S} \text{diag}[\exp(\lambda_0 t), \dots, \exp(\lambda_3 t)] \mathbb{S}^{-1} \quad (5)$$

where the columns of the matrix \mathbb{S} consist of the eigenvectors of the matrix \mathbb{A} .

It is worth noting that if the initial time (i.e., time zero, $t = 0$) is chosen as the time when anthropogenic emissions were still absent and natural emissions insignificant (in net terms), the initial vector \mathbf{c}_0 corresponds to the steady state attained by the planet when $\mathbf{E} = \mathbf{0}$. This is given by the solution of the system $\mathbb{A}\mathbf{c}_{ss} = \mathbf{0}$, which

is non-trivial because of the singularity of the matrix \mathbb{A} . The solution is any vector parallel to the eigenvector, \mathbf{z}_0 , belonging to the zero eigenvalue, λ_0 , of the matrix \mathbb{A} . In this case, it can be proven that $\exp(t\mathbb{A})\mathbf{c}_{ss} = \mathbf{c}_{ss}$.

The evolution of the (scalar) CO₂ concentration in the atmosphere, $c_C(t)$, from the time zero defined as discussed above is then written as:

$$\begin{aligned} c_C(t) &= c_{C,ss} + \int_0^t E_C(t') \sum_{j=0}^3 a_j \exp(\lambda_j(t-t')) dt' \\ &= c_{C,ss} + \int_0^t E_C(t') \left(a_0 + \sum_{j=1}^3 a_j \exp\left(\frac{t'-t}{\tau_j}\right) \right) dt' \\ &\stackrel{E_C=const}{=} c_{C,ss} + E_C \left(- \sum_{j=1}^3 a_j \tau_j \exp\left(\frac{-t}{\tau_j}\right) + \sum_{j=1}^3 a_j \tau_j + a_0 t \right) \end{aligned} \quad (6)$$

where λ_j is the j -th eigenvalue (with $\lambda_0 = 0$), $\tau_j = -1/\lambda_j$ (for $j > 0$) is the corresponding characteristic decay time, and the constant a_j is a coefficient estimated by fitting climate data. In particular, $a_0 \approx a_1 \approx 0.22$ and $a_2 \approx a_3 \approx 0.28$, whereas $\tau_1 \approx 395$, $\tau_2 \approx 37$, and $\tau_3 \approx 4.3$ (Table 2 in the Appendix reports the current best estimates, which were employed in this study).

Equation (6) demonstrates that the climate impact of CO₂ is indeed cumulative, namely because of the permanence of the initial condition and of the infinitely long decay time associated to the zero eigenvalue. From a physical point of view this is justified by the fact that CO₂ is simply exchanged among compartments, but it can never leave the planetary system. It is worth noting that there is a simple approximation of the values of the parameters above, which is easy to memorize: $a_0 \approx a_1 \approx a_2 \approx a_3 \approx 1/4$, whereas $\tau_1 \approx 400$, $\tau_2 \approx 40$, and $\tau_3 \approx 4$.

3.2 Radiative forcing

3.2.1 From concentration to radiative forcing

As already explained through the chain of causality (Figure 1), emissions of a CF_{*i*} generate a corresponding radiative forcing (F_i), which is a function of the concentration of that pollutant (c_i) (and possibly of the concentrations of other GHGs, a feedback that for the sake of simplicity but without loss of generality is neglected in our simplified LCM), but not of its evolution. Such relationship can be expressed in the LCM as $F_i(t) = f_i(c_i)$, where $f_i(\cdot)$ is a function specific of the CF_{*i*} under consideration, namely a nonlinear monotonically increasing function. The overall radiative forcing of the atmosphere is given by the sum of the radiative forcings of all GHGs (and of the other climate forcers), as established by the superposition principle.

Assessing the precise magnitudes of radiative forcing associated with individual greenhouse gases (GHGs) or the cumulative impact on the entire atmosphere poses a formidable challenge. It necessitates the utilization of an atmospheric model that exhibits a high degree of accuracy not only for the GHG of interest but also for all other relevant GHGs. Central to this challenge are two crucial elements: firstly, a rigorous characterization of the non-linear relationship between radiative forcing (F_i) and the concentration of the GHG (c_i), potentially accounting for interactions with other GHGs; and secondly, the availability of precise data regarding the temporal evolution of emissions from all GHGs, spanning from the start of the integration (as indicated in Equations (1) and (3)) to the final time (t) of the radiative forcing evaluation.

In light of this approach, determining the extent of contribution to atmospheric radiative forcing, temperature anomalies, and climate change attributed to a specific emitter, such as an economic sector or a country, over a limited time interval, demands the formulation of rules for allocating these effects to the specific emitter. This allocation would depend on various factors, including the emitter's absolute and relative

location, emission profile, and other relevant considerations. Undoubtedly, this task is complex. Nevertheless, we posit that such detailed attribution may not always be necessary, especially when dealing with relatively small emitters, particularly within the broader context of formulating effective climate policies.

The approach that we propose is that of considering the differential contribution of the specific emitter mentioned above to the concentration of a given CF_i , i.e., Δc_i , (where i refers to any GHG, including carbon dioxide) and, subsequently, the differential contribution of the CF emissions to the radiative forcing, i.e., ΔF_i .

The aforementioned approach of using differential contributions enables a focused analysis on specific emissions of interest, without necessitating the calibration of the model with regard to the initial state or the temporal evolution of past and future background emissions. This differential perturbation approach proves especially promising when examining emissions from specific economic sectors within a country (such as Switzerland) with total emissions of the order of 0.1% of the global level. Moreover, this approach becomes even more relevant when the objective is to chart pathways towards achieving net-zero emissions in terms of greenhouse gases expressed in CO₂ equivalents. Such assessments play a crucial role in informing and supporting climate policy decisions. The differential perturbation approach adopted in this work will be further discussed in Section 3.3.

The governing mathematical relationships defining the radiative forcing from the concentration of a polluter i are as follows:

$$F_i = f_i(c_i) \quad (7)$$

$$\Delta F_i = \frac{df_i}{dc_i} \Delta c_i = A_i \Delta c_i \quad (8)$$

where we assume for simplicity that the radiative forcing of a CF_i depends only on its concentration and not on those of the other GHGs. The derivative df_i/dc_i is the so called radiative forcing efficiency, A_i , or ERF. Its value depends on c_i ($A_i = df_i/dc_i$); in general A_i changes slowly with c_i , due the relatively weak non-linearity of $f_i(c_i)$. Therefore, in the scope of this work, we will treat A_i as a constant, at least locally, and particularly over the specified time intervals (as illustrated in Figure 2). The values of A_i used for different climate forcers are specified in ?? and Table 6 in the Appendix.

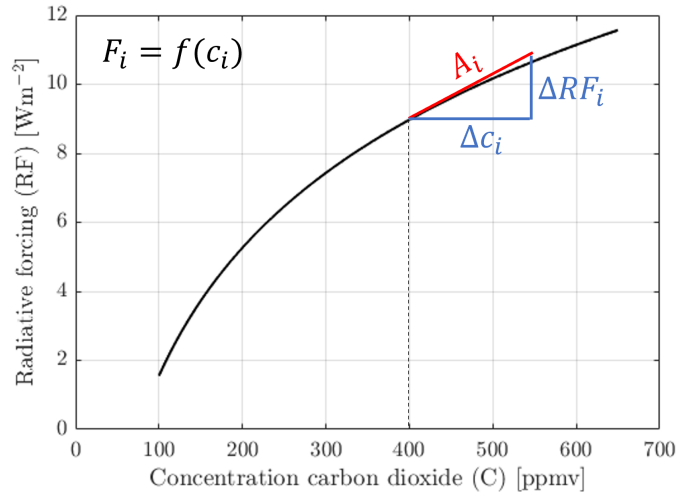


Figure 2. Radiative forcing as a function of the concentration⁸ and representation of the local linearization of the radiative forcing efficiency, A_i .

Specifically for carbon dioxide, it is worth noting that there are several expressions for the radiative forcing as a function of the CO₂ concentration in the atmosphere. In the context of climate models, often the

following single-parameter logarithmic expression is used:

$$F_C(c_C) = \frac{\Delta F^{2 \times CO_2}}{\ln 2} \ln \left(\frac{c_C}{c_{C,ss}} \right) \quad (9)$$

where $c_{C,ss}$ represents the pre-industrial steady-state CO₂ concentration (typically 280 ppm), and the parameter $\Delta F^{2 \times CO_2}$ is the net change in radiative forcing associated with a doubling of the atmospheric CO₂ concentration (i.e., $\Delta F^{2 \times CO_2} = F_C(2w) - F_C(w)$, for any value of w).⁹ Note that the expression above results in a zero radiative forcing when $c_C = c_{C,ss}$ (i.e., representing a change of radiative forcing due to anthropogenic perturbations with respect to the unperturbed pre-industrial state).

Combining Equation (8) and Equation (9) yields the following expression for the CO₂ radiative efficiency:

$$A_C = \frac{\Delta F^{2 \times CO_2}}{c_C \ln 2} \quad (10)$$

which does not depend on the reference CO₂ concentration, as required.

3.2.2 From non-GHG climate effects to radiative forcing

Aviation contributes to climate change through emissions of CO₂ and of short-lived GHGs such as NO_x, SO₂, black carbon (BC) and water vapour (H₂O).⁴ These "non-CO₂" SLCFs are released in the atmosphere and contribute to the increase in total radiative forcing. The understanding of these non-CO₂ impacts has advanced over time, making it possible to characterize, with acceptable accuracy, the radiative efficiency describing the relationship between atmospheric non-CO₂ SLCF emissions and the associated increase in radiative forcing.^{4,10-12}

Nonetheless, the climate impact of the aviation sector is also considerably determined by "non-GHG climate effects" such as the formation of cirrus clouds.⁴ Cirrus clouds are extremely short-lived climate forcers and their evolution and behavior can be described in terms of their characteristic time, τ_{cc} , and their mixing time, t_{cc} . For these non-GHG effects it can be assumed that $\tau_{cc} \ll t_{cc}$, leading to an heterogeneity in their atmospheric mixing. Therefore, the resulting radiative forcing, F_{cc} , is not a function of the climate forcer's concentration, but rather of the local conditions at the time of the emissions.

Following the relevant state of the art⁴⁻⁶, and being one of the objectives of this modeling approach to assess the global climate impact of the Swiss aviation sector, rather than the impact of a specific flight, we simplify the behavior of these very short-lived cirrus clouds by parametrizing their radiative forcing in terms of kilometers of air traffic volume. Then, following the assumption of superposition of effects, these parametrized forcings are summed to the other GHG contributions to obtain an overall radiative forcing.

Though local, flight cirrus effects are averaged globally, where the parametrization of their total radiative forcing based on the kilometers flown is a justified and consistent choice in literature and global climate models. In fact, despite being a critical parameter, the radiative forcing potential of these very-short lived "non-GHG effects" presents a significant uncertainty stemming from the undetermined time-dependent and location-dependent conditions leading to their formation.⁴ Due to the lack of information and comprehensive models accurately describing the mechanisms and effects influencing the formation and radiative forcing potential of cirrus clouds, parametrization in terms of kilometers of air traffic volume currently remains the only meaningful approach to determine the climate impact of "non-GHG effects" in this study. A future sensitivity analysis may also be conducted to determine the level of uncertainty introduced by this simplification and homogenization approach.

With an improved understanding over time of the optoelectronic properties of cirrus clouds and their climate

impact potential, important mitigation measures (e.g., changes in flight operation, the so called "navigational avoidance") may be introduced, leading to a lower uncertainty and, possibly, a lower absolute climate impact associated with these "non-GHG effects".

3.3 Differential perturbation approach

The emission profile of a CF_i can be split in two contributions, namely the emissions of the specific agent or emitter that must be considered ($E_{i,s}$, with s standing for "specific") and the global emissions ($E_{i,g}$, with g standing for "global") which cannot be controlled by the specific emitter (Swiss agriculture emitters have no control over global agriculture emissions). The overall emissions are the sum of the two contributions and can be written as follows:

$$E_i(t) = E_{i,g}(t) + E_{i,s}(t) \quad (11)$$

In this context, the emissions from the specific agent are regarded as a relatively minor perturbation to the global background emissions. The specific agent under consideration could be, for example, the agricultural sector in Switzerland or a particular industrial plant, e.g., a cement plant located for instance in Canton Aargau.

Substituting this last equation into Equation (2) (or Equation (6) for carbon dioxide) yields the following expression for the concentration of the CF_i :

$$\begin{aligned} c_i(t) &= c_{i,0} \exp\left(-\frac{t}{\tau_i}\right) + \int_0^t (E_{i,g}(t') + E_{i,s}(t')) \exp\left(\frac{t' - t}{\tau_i}\right) dt' \\ &= c_{i,0} \exp\left(-\frac{t}{\tau_i}\right) + \int_0^t E_{i,g}(t') \exp\left(\frac{t' - t}{\tau_i}\right) dt' + \int_0^t E_{i,s}(t') \exp\left(\frac{t' - t}{\tau_i}\right) dt' \\ &= c_{i,g}(t) + \Delta c_{i,s}(t) \end{aligned} \quad (12)$$

where $\Delta c_{i,s}(t)$ is the differential concentration perturbation of a CF_i due to the emissions perturbation, $E_{i,s}(t)$, from a specific agent:

$$\Delta c_{i,s}(t) = \int_0^t E_{i,s}(t') \exp\left(\frac{t' - t}{\tau_i}\right) dt' \quad (13)$$

It is worth emphasizing that this expression is independent both of the initial value of CF_i concentrations, which may be uncertain, and of the trajectory of global CF_i emissions, which can be challenging to accurately determine over the specified time interval of interest.

From Equation (13), the expression of the differential perturbation in the radiative forcing of CF_i attributable to its specific emissions is straightforwardly obtained:

$$\Delta F_{i,s}(t) = A_i \Delta c_{i,s}(t) = A_i \int_0^t E_{i,s}(t') \exp\left(\frac{t' - t}{\tau_i}\right) dt' \quad (14)$$

The following similar expression can be obtained for carbon dioxide, through the same derivation:

$$\Delta F_{C,s}(t) = A_C \Delta c_{C,s}(t) = A_C \int_0^t E_{C,s}(t') \left(a_0 + \sum_{j=1}^3 a_j \exp\left(\frac{t' - t}{\tau_j}\right) \right) dt' \quad (15)$$

As previously mentioned, we can aggregate all the specific radiative forcing values to compute a total radiative forcing differential:

$$\Delta F_s(t) = \sum_i \Delta F_{i,s}(t) \quad (16)$$

This total radiative forcing perturbation can be used to solve planetary energy balances and compute the final temperature anomaly, hence climate change, due to specific emissions of different GHGs i . Further information on the calculation of the temperature anomaly are provided in Section 3.5.

3.4 Linear Warming Equivalent (LWE)

Before discussing the modeling equations to compute the temperature anomaly given a certain total radiative forcing perturbation $\Delta F_s(t)$, it is important to discuss the principle of the Linear Warming Equivalent (LWE) model, introduced by Myles Allen and collaborators¹²

Its physical basis is the fact that the temperature anomaly depends on the overall radiative forcing over time due to all climate forcers in the atmosphere. In other words, the left hand side of Equation (16), i.e., the term that counts in determining the temperature anomaly, is indifferent to which climate forcer is responsible for each individual contribution in the right hand side, i.e., the individual radiative forcings. Therefore, if one substitutes the radiative forcing $\Delta F_{i,s}(t)$ due to the forcer CF_i with the same quantity but generated by the forcer CF_j , i.e., where $\Delta F_{j,s}(t) = \Delta F_{i,s}(t)$, the overall radiative forcing, $\Delta F_s(t)$, remains identical, and so does the corresponding temperature anomaly. If CF_j is CO_2 , then the LWE principle allows to establish a radiative forcing equivalence between any pollutant CF_i and in fact CO_2 , hence an explicit equivalence between CF_i and CO_2 in terms of warming. This can be written as:

$$\Delta F_{i,s}(t) = \Delta F_{C,s}(t) \quad (17)$$

Since radiative forcing depends on emissions, LWE can be established by determining the CO_2 emission profile yielding the same radiative forcing as the given CF_i emission profile by substituting Equation (14) or Equation (15) into Equation (17), thus obtaining:

$$\Delta F_{i,s}(t) = A_i \int_0^t E_{i,s}(t') \exp\left(\frac{t' - t}{\tau_i}\right) dt' = A_C \int_0^t E_{C,s}(t') \left(a_0 + \sum_{j=1}^3 a_j \exp\left(\frac{t' - t}{\tau_j}\right) \right) dt' = \Delta F_{C,s}(t) \quad (18)$$

This equation can be used to determine the CO_2 emission profile, i.e., $E_{C,s}(t)$, for a given CF_i emission profile, i.e., $E_{i,s}(t)$. Such mathematical inversion constitutes a linear problem, that can be solved directly through simple matrix inversion when the integrals above are calculated numerically through simple quadrature formulas, e.g., the trapezoid rule.

This is a very important result, because the CO_2 emission profile thus calculated through the LWE principle can be used as a CDR (carbon dioxide removal) profile implemented to generate the NET (negative emissions) profile needed to compensate the climate impact of the given CF_i emission profile. This is a unique opportunity offered by the possibility of removing CO_2 from the atmosphere with one or the other of the NET solutions. And this is obviously a key instrument to be used in defining any path towards net-zero climate impacts and in implementing the associated strategy.

3.5 Temperature anomaly

The temperature anomaly or temperature response (i.e., the temperature difference between its level at any chosen time and its value at a pre-industrial equilibrium state) can be determined by solving planetary energy balances that account for the effective radiative forcing (F) caused by the different climate forcers, whose combined effect is obtained by summing the individual radiative forcings. There are two state-of-the-art models that differ in how they partition the control volume, i.e., the planetary domain within which climate models enforce energy conservation and describe the temperature evolution, i.e., the atmosphere and the oceans. These are the two-layer and the three-layer models.

3.5.1 Two-layer model

The two-layer model considers a surface layer, including the atmosphere and the upper part of the ocean, (with global average temperature anomaly given by T_s , where s stands for "surface") and a deep-ocean layer

(with temperature anomaly T_d , where d stands for "deep")¹³. The two layers have heat capacities C_s and C_d , respectively, with $\epsilon = C_s/C_d \approx 0.07 \ll 1$.⁹ These two layers exchange heat at a rate proportional to their temperature difference and to a heat exchange coefficient, γ , that accounts for all processes transporting heat between the two layers.

The equations of the two-layer model are written as:

$$C_s \frac{dT_s}{dt} = F - \lambda T_s - \gamma(T_s - T_d) \quad (19)$$

$$C_d \frac{dT_d}{dt} = \gamma(T_s - T_d) \quad (20)$$

In this context, F represents the effective radiative forcing, which refers to the global average planetary energy imbalance resulting from the elevated levels of greenhouse gases, and other forcers, in the atmosphere compared to the pre-industrial equilibrium state. The parameter λ is commonly referred to as the equilibrium sensitivity parameter (with units [$\text{Wm}^{-2}\text{K}^{-1}$]); it represents the additional rate at which energy is radiated from the Earth to space for each degree of temperature anomaly. Lastly, the parameter γ denotes the heat exchange coefficient governing the interaction between the surface and the deep-layer.

Equation (19) and Equation (20) constitute a system of two ordinary differential equations. In the absence of radiative forcing, i.e., when $F = 0$, this system possesses a single stable equilibrium point at $T_s = T_d = 0$. Indeed, both eigenvalues, denoted as λ_k with $k = 1, 2$, associated to this system are real and negative. The reciprocals of the absolute values of the eigenvalues define two characteristic time constants, called s_k . These timescales govern the rate at which the system responds to perturbations in radiative forcing, consequently influencing the evolution of warming over time. In more detailed discussions to follow, we will observe that the temperature anomaly evolution is governed by two characteristic timescales, namely, the fast timescale, s_1 , and the slow timescale, s_2 . The fast timescale, s_1 , arises from the rapid adjustment of the upper thermal layer to perturbations in radiative forcing. Conversely, the slow timescale, s_2 , reflects the fact that the transfer of excess heat from the upper layer to the deep oceans is a slow process; this lower thermal layer exhibits a considerably greater degree of inertia, leading to a delayed response to perturbations in radiative forcing.

In the presence of forcing, i.e., when $F > 0$, the global average surface temperature anomaly evolves from the time when anthropogenic GHG emissions become non-negligible, set at $t = 0$, according to the following relationship:

$$T_s(t) = \sum_{k=1}^2 b_k \left(\int_0^t F(t') \exp\left(\frac{t' - t}{s_k}\right) dt' \right) \quad (21)$$

As seen in Equation (21), the temperature anomaly depends on the radiative forcing caused by the ensemble of GHGs present in the atmosphere (F). Indeed, if two different climate forcers, CF_i and CF_j , generate the same radiative forcing profile during the observed time period ($F_{i,s} = F_{j,s}$), then, by definition, their impact on the temperature anomaly is equivalent. In simpler terms, when comparing emissions from various climate forcers, it is sufficient to assess the radiative forcing they produce to determine their relative contributions to the temperature anomaly. Therefore, having the same radiative forcing implies an identical effect on the temperature anomaly, highlighting the fundamental principle that equal radiative forcing leads to the same temperature anomaly contribution. This concept is essential for understanding and comparing the climate impact of various greenhouse gases and emissions sources (see also the discussion around the LWE approach in Section 3.4).

Because of the linear relationship between temperature anomaly and radiative forcing, the same differential perturbation approach, as employed in Section 3.3 for the radiative forcing, can be applied to the temperature anomaly. Namely, the temperature anomaly can be split into a global contribution and a specific contribution:

$$T_s(t) = T_{s,g}(t) + \Delta T_{s,s}(t) \quad (22)$$

For a specific, total radiative forcing differential, denoted as ΔF_s (as defined in Equation (16)), we can rewrite Equation (21) to represent the specific differential surface temperature anomaly, denoted as $\Delta T_{s,s}$, in the following manner:

$$\Delta T_{s,s}(t) = \sum_{k=1}^2 b_k \left(\int_0^t \Delta F_s(t') \exp\left(\frac{t' - t}{s_k}\right) dt' \right) \quad (23)$$

The parameters b_k are calculated from the eigenvectors belonging to the eigenvalues associated to the system and have units of $[\text{m}^2 \text{K W}^{-1} \text{yr}^{-1}]$.

$$b_1 = \frac{-\phi_2}{C_s(\phi_1 - \phi_2)} \quad (24)$$

$$b_2 = \frac{\phi_1}{C_s(\phi_1 - \phi_2)} \quad (25)$$

where ϕ_1 and ϕ_2 are the first components of the eigenvectors associated to the timescales s_1 (fast characteristic time) and s_2 (slow characteristic time) of the system, respectively.

When the radiative forcing remains constant at a steady state value F^{SS} , Equation (19) converges to a stable equilibrium state where T_s equals T_d , and this occurs over a timescale approximately of the same order of magnitude as s_2 . The temperature anomaly at this steady state, denoted as T_s^{SS} , corresponding to the constant radiative forcing F^{SS} , can be determined by solving Equation (19) with the condition $T_s = T_d = \text{constant}$. The steady state temperature solution is given by the following equation, where F^{SS} is split into the global background contribution and the perturbation due to a specific emitter:

$$T_s^{SS} = \frac{F^{SS}}{\lambda} = \frac{F_g^{SS}}{\lambda} + \frac{\Delta F_s^{SS}}{\lambda} \quad (26)$$

Two other important quantities are the Equilibrium Climate Sensitivity (ECS) and the Transient Climate Response (TCR)^{3,13}. On the one hand, ECS is defined as the equilibrium mean surface air temperature anomaly resulting from a doubling of the atmospheric carbon dioxide radiative forcing. In other words, it quantifies the long-term temperature change that would occur when the concentration of atmospheric carbon dioxide doubles, assuming all other climate-related factors remain constant. ECS is a key measure to understand the potential long-term impacts of CO₂- or CO₂-eq.-induced climate change. On the other hand, TCR is defined as the transient climate response resulting from a 1% increase in atmospheric CO₂ concentration per year, until it reaches twice its initial value (2× CO₂), followed by the stabilization of this concentration. TCR provides insights into the short-to-medium-term temperature response to CO₂ and CO₂-eq. forcing and is particularly relevant to understand climate changes over the coming decades. These two temperatures are essential for characterizing different aspects of the Earth's climate response to changing CO₂-eq. levels and radiative forcing. They are valuable tools for climate scientists and policymakers in assessing and addressing the challenges posed by global warming.

The mathematical expressions for the ECS, T_{ECS} , and for the TCR, T_{TCR} , are derived from Equation (23) and are obviously consistent with corresponding relationships reported in the literature^{3,13}. One obtains:

$$T_{ECS} = \Delta F^{2 \times \text{CO}_2} (b_1 s_1 + b_2 s_2) = \Delta F^{2 \times \text{CO}_2} (q_1 + q_2) = \frac{\Delta F^{2 \times \text{CO}_2}}{\lambda} \quad (27)$$

$$T_{TCR} = \Delta F^{2 \times \text{CO}_2} \left[q_1 \left(1 - \frac{s_1}{D} \left(1 - \exp\left(-\frac{D}{s_1}\right) \right) \right) + q_2 \left(1 - \frac{s_2}{D} \left(1 - \exp\left(-\frac{D}{s_2}\right) \right) \right) \right] \quad (28)$$

where q_k are parameters defined as $q_k = b_k s_k$ and are expressed in units of $[\text{m}^2 \text{KW}^{-1}]$. It is worth noting that the reciprocal of the sum of the q_k parameters equals the equilibrium sensitivity parameter, i.e., $\lambda = \left[\sum q_k \right]^{-1}$.

The parameter D is defined as $D = \log(2)/\log(1.01) = 69.7$ yr as a result of the TCR definition, hence it indicates the time required to double the CO_2 concentration, c_C , when it grows with an yearly rate of 1%. Finally, $\Delta F^{2 \times \text{CO}_2}$ is the change in radiative forcing due to a doubling of the CO_2 concentration (Section 3.2), which is equal to 3.71 W m^{-2} .¹⁴

As previously mentioned, the impact of radiative forcing on the surface temperature anomaly occurs on a rather short (s_1) and on a very long timescale (s_2). Given values of λ , γ , C_s and C_d (Equation (19)), it is possible to calculate the eigenvalues (λ_k) and components of the eigenvectors (ϕ_k) associated to the system. From these, the climate response timescales (s_k) and the parameters b_k and q_k can be determined. The values of these parameters are reported in the literature^{15,16} and are: $q_2 = 0.429 \text{ K W}^{-1} \text{ m}^2$, $q_1 = 0.631 \text{ K W}^{-1} \text{ m}^2$, $s_2 = 409.5$ yr, $s_1 = 8.4$ yr.

Alternatively, the values of q_1 and q_2 can be determined, for given s_k values, by solving Equation (27) and Equation (28) for specified values of ECS and TCR. Following the FAIR v1.3 model³, the characteristic timescale can be set as $s_1 = 4.1$ yr and $s_2 = 239$ yr. In line with the "very likely" ranges reported by the IPCC AR6 assessment, T_{ECS} and T_{TCR} were set equal to 2.8°C and 1.5°C , respectively; q_2 and q_1 assume then the values of 0.245 and $0.51 \text{ K W}^{-1} \text{ m}^2$, respectively. From the values of s_1 , s_2 , q_1 and q_2 the model parameters λ , γ , C_s and C_d can be calculated.

3.5.2 Three-layer model

The three-layer model has been recently introduced to better characterize the planetary energy balances and heat exchanges^{17,18}. In the three-layer climate model the first layer represents the atmosphere and the uppermost layer of the ocean (with temperature anomaly T_s , similarly to the two-layer model), while the deep ocean is partitioned in two distinct layers: a mid-ocean zone and an abyssal-ocean zone, with temperature anomalies T_m and T_a , respectively. The equations of the three-layer model are written as:

$$C_s \frac{dT_s}{dt} = F - \lambda T_s - \gamma_1(T_s - T_m) \quad (29)$$

$$C_m \frac{dT_m}{dt} = \gamma_1(T_s - T_m) - \gamma_2(T_m - T_a) \quad (30)$$

$$C_a \frac{dT_a}{dt} = \gamma_2(T_m - T_a) \quad (31)$$

The current version of FAIR (version 2, Leach et al.²) is based on a three-layer climate model. The three-layer and the two-layer model share the same mathematical structure, with the three layer model having three eigenvalues and three eigenvectors instead of only two. The surface temperature anomaly calculated with a three-layer model, given an assigned radiative forcing perturbation, and assuming the differential perturbation approach, can be written as follows:

$$\Delta T_{s,s}(t) = \sum_{k=1}^3 b_k \left(\int_0^t \Delta F_s(t') \exp\left(\frac{t' - t}{s_k}\right) dt' \right) \quad (32)$$

The thermal response parameters are set as follows: $s_1 = 0.903$, $s_2 = 7.92$ and $s_3 = 355$ yr, $q_1 = 0.180$, $q_2 = 0.297$ and $q_3 = 0.386 \text{ K W}^{-1} \text{ m}^2$ (for ECS=3.24 K and TCR=1.79 K). The equilibrium sensitivity parameter, λ , can be determined from the ratio of the effective radiative forcing at CO_2 doubling ($\Delta F^{2 \times \text{CO}_2} = 3.76 \text{ W m}^{-2}$ in Leach et al.²) and the ECS, hence λ exhibits the value of $1.16 \text{ W m}^{-2} \text{ K}^{-1}$.

The values of the thermal response parameters (i.e., b_k and s_k) are set equal to those of the FAIR model² so as to allow for comparison with the model results obtained in this study.

4 Comparison with the FAIR climate model

The simplified linear climate model (SLCM) utilized in this study is here compared with the Finite Amplitude Impulse Response (FaIR) climate model. FaIR is a well-established climate model that has been utilized in various scientific studies and has also been used as a trustworthy reference in the body of work considered in the latest IPCC AR6¹⁹. This comparison allows for a thorough evaluation of the simplified model's performance and accuracy compared to FaIR.

The simplified model approach proposed in this study is, as mentioned in the sections above, built on the concept of a chain of causality. In this framework, the radiative efficiency A_i is assumed to be constant and non-linear feedbacks between different greenhouse gases are not considered explicitly. These assumptions lead to a linear, simplified model dependent on fewer parameters. In the scope of climate policies, this enables a more transparent understanding of the effects related to climate change. On the contrary, FAIR does include feedbacks and indirect effects when assessing the forcing and warming of a pollutant i .

The following remarks on FaIR are worth making. FaIR, like many climate models, acknowledges the presence of significant uncertainty in its input parameters, and therefore in its output. This uncertainty has various causes, including uncertainties in the Effective Radiative Forcing (ERF) of different pollutants (e.g., greenhouse gases) and the climate response parameters, such as Equilibrium Climate Sensitivity (ECS) and Transient Climate Response (TCR). For example, Table 6 in Leach et al.² provides an indication of the large uncertainties of the ERF for different pollutants (e.g., $\pm 28\%$ for CH₄, $\pm 20\%$ for N₂O, $\pm 75\%$ for contrails, as a result of the total NO_x emitted and the aviation NO_x fraction). It is worth mentioning that, due to the linearity of our model, the uncertainties of the Effective Radiative Forcings (ERF) are reflected proportionally on the radiative forcing efficiencies of each pollutant i , A_i .

To address parameter uncertainty, FaIR employs ensemble simulations. These involve varying one or more input parameters within a predefined range or distribution (i.e., based on the assessments reported in the literature and compiled in the IPCC reports). These parameters can include emission scenarios, radiative efficiencies, climate response parameters, and more. For each combination of parameter values within the specified range, the model is run to simulate the climate response. Each run represents a different scenario or trajectory. By running multiple simulations with different parameter combinations, researchers can explore the range of possible climate outcomes and assess their likelihood. This ensemble approach helps provide a more comprehensive view of climate predictions, including their uncertainties.

Incorporating uncertainty by assigning a probability distribution to the values of the model parameters and by analyzing ensemble simulations using statistics is a sensible and effective way to acknowledge the multi-scale complexity of the climate system and the inherent impossibility of modeling it in a physically rigorous manner.

Forcing and warming simulation results from the simplified, linear climate model proposed in this study (herein referred to as Linear Climate Model, LCM) are comparatively assessed with respect to those obtained with the FaIR climate model by following the five-step procedure described herewith:

1. FaIR is employed to simulate the forcing and temperature anomaly curves for different GHGs emission profiles of interest in this study. For N₂O, CH₄ and CO₂, the corresponding EP2050+ ZeroBasis agriculture emission profiles are employed (starting from 1760); for NO_x the ZeroBasis aviation emission profile is selected (starting from 1950). Additional information on data collection for the different emission profiles is provided in Section 6.1, for Swiss agriculture, and Section 7.1, for Swiss aviation. FaIR simulations were conducted using version v2.1.0 of the python package, calibration version v1.1.0 and aligning global background emissions to the SSP1-2.6 IPCC scenario. The warming attributed to Swiss emissions is calculated as a delta relative to global emissions; hence, the SSP1-2.6 was first simulated and then Swiss emissions were subtracted from global emissions and simulations

were repeated: the difference in temperature between the two cases was attributed to the warming from Swiss emissions. As Switzerland does not have control over global future scenarios, assessing the influence of various background projections on the climate impact of Swiss emissions, as a result of feedback effects, was beyond the scope of this project.

2. Ensemble simulations and the obtained distribution of outcomes (expressed in terms of 5% and 95% quantiles around the 50% quantile, considered the reference value) were generated with FAIR, in order to assess the uncertainty around the temperature anomaly results from this model.
3. The same emissions profiles, as discussed in point 1), are analyzed with the simplified linear climate model (LCM) proposed in this study, for both the two-layer model (LCM - 2L) and the three-layer model (LCM - 3L). Simulations with the LCM model are found to be well within the uncertainty range provided by FAIR, though underestimating the 50% quantile of FAIR results.
4. LCM results are better aligned to the 50% FaIR quantile results by accounting for the indirect effects through an empirical model calibration. The correction improves the LCM-simulated absolute values of forcing and climate impact, aligning the simplified model results more closely with the 50% FaIR quantile. The calibration is chosen as trade-off between short-time versus long-time agreement with the FAIR warming evolution. It is important to reiterate that achieving an exact match with the FAIR results is not a strict requirement, as these outcomes are subject to significant uncertainties stemming from inherent uncertainties in future emissions scenarios and in climate system models' predictions, as discussed earlier. Calibration of the LCM temperature anomaly results is performed by adjusting the radiative forcing efficiency of different pollutants (A_i) within the uncertainty of the effective radiative forcing (ERF) as provided by FaIR². In fact, due to the linearity of the LCM model, the uncertainties of the ERFs are reflected on the radiative forcing efficiencies of each pollutant (A_i). Calibration factors for each GHG are provided in Table 1.
5. The temperature anomaly curve of the calibrated forcing is provided only for the LCM 3-layer model, as this will be employed in this study to ensure consistency with the latest version of the FaIR model (further explanation in Section 3.5).

Table 1. Radiative forcing efficiencies (A_i) and their uncertainties, as provided by Forster et al.¹⁹ for CH₄, N₂O and CO₂ and Sacchi et al.⁶ for NO_x, ERF uncertainty as provided by Leach et al.² (FaIR v2.0) and the calibration factor employed to empirically account for indirect effects within the simplified LCM presented in this study. The calibration factors selected are well within the uncertainty ranges listed.

	A_i (LCM-3L) [W m ⁻² kg ⁻¹]	A_i uncertainty [W m ⁻² kg ⁻¹]	ERF uncertainty ²	Calibration factor used in the LCM
CH ₄	2.0×10^{-13}	$\pm 0.5 \times 10^{-13}$	$\pm 28\%$	+20%
N ₂ O	3.6×10^{-13}	$\pm 1.4 \times 10^{-13}$	$\pm 20\%$	+5%
CO ₂	1.70×10^{-15}	$\pm 0.21 \times 10^{-15}$	$\pm 20\%$	+0%
NO _x	1.67×10^{-12}	-	$\pm 20\%$	-10%

Visual representation of the LCM-FaIR results comparison, and calibration of LCM to align the simplified model results more closely with the 50% FaIR quantile is shown for CH₄ and N₂O. The resulting methane-induced forcing is shown in Figure 3a.1), while the corresponding warming is shown in Figure 3a.2). Similarly, the emissions-induced forcing and associated warming for nitrous oxide are displayed in Figure 3b.1) and b.2), respectively. Simulations from FAIR are shown in black, while the results from the LCM with a two-layer model (2L) are plotted in red, and with a three-layer climate model (3L) in blue. For the FaIR-simulated warming, the model's uncertainty is quantified through ensemble simulations, with the 5% and 95% quantiles represented in gray, and the uncertainty area shaded; the FAIR-calculated warming (black curves of Figure 3a.2

and Figure 3b.2) corresponds to the 50% quantiles.

The FaIR-simulated forcing and warming curves encompass the climate impacts induced both directly by the pollutant in question (i.e., CH₄ or N₂O) and indirectly through feedback effects (such as an increase in atmospheric ozone concentration resulting from CH₄ emissions). In contrast, the LCM-simulated forcing and warming curves consider only the climate impact of CH₄ and N₂O, as our simplified model does not account for non-linear feedbacks within the climate system.

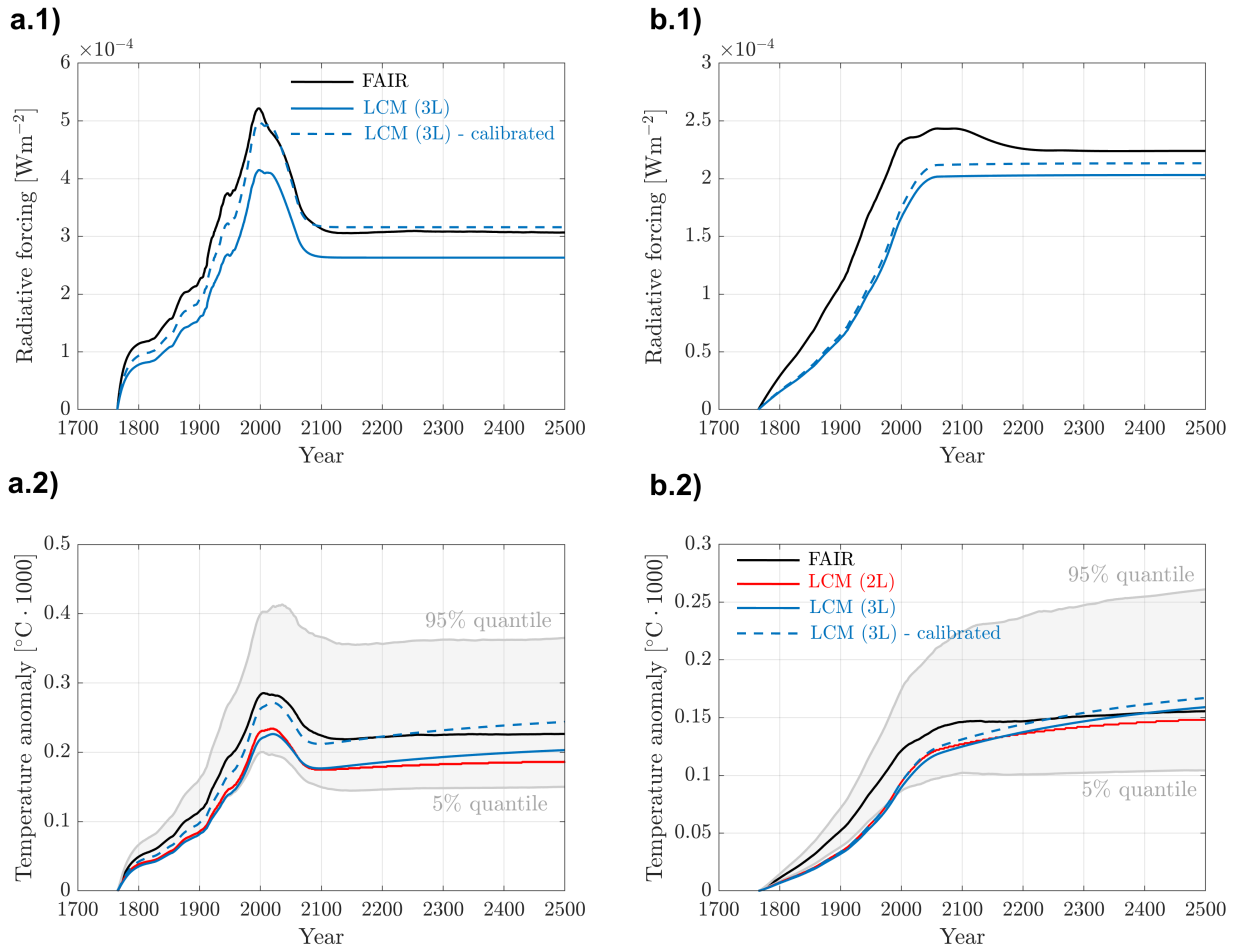


Figure 3. Methane-induced forcing is illustrated in Figure 3a.1), while the corresponding warming is depicted in Figure 3a.2). The emissions-induced forcing and associated warming for nitrous oxide are displayed in Figure 3b.1) and b.2), respectively. Simulations from FAIR are shown in black, while the results from the simplified Linear Climate Model (LCM) are plotted in red for two-layer temperature anomaly modeling (L2), or in blue for a three-layer (3L) modeling. For the FaIR-simulated warming, the model’s uncertainty is quantified through ensemble simulations, with the 5% and 95% quantiles represented in gray, and the uncertainty area is shaded. Model simulations are performed for the agriculture methane and nitrous oxide emissions following the ZeroBasis EP2050+ scenario (for further information refer to Section 6.1). Lastly, calibration of the LCM (L3) results to get closer to the 50% quantile of the FaIR model are highlighted showed with dashed-blue lines.

The results, as illustrated in Figure 3a.2) and b.2), demonstrate little differences between the outcomes of the LCM (2L), plotted as a solid red line, and the LCM (3L), plotted as a solid blue line. The most evident difference has to do with the ultimate equilibrium temperature anomaly, which is higher for the LCM (3L).

This difference arises from the higher values of the Equilibrium Climate Sensitivity (ECS), and therefore of the climate feedback parameter (λ), in the 3L model. Additionally, the LCM (3L) takes a longer time to reach this equilibrium due to the larger value of the longer time scale ($s_3 = 355yr$ in the LCM-L3 model instead of $s_2 = 239yr$ in the LCM-L2 model).

The necessity for a calibration factor was also analyzed for aviation-induced GHGs emissions that have a non-negligible climate impact, namely CO_2 and NO_x . The carbon dioxide generated warming, as simulated by the LCM (3L) model, perfectly aligns with that predicted by FaIR. Instead, for NO_x a calibration factor of 0.9 was implemented, effectively decreasing the radiative forcing efficiency by 10%.

Overall, the LCM-simulations show a good agreement with the FaIR results, both qualitatively and quantitatively, especially when employing an empirical calibration to account for, in a simplified way, non-linear feedback effects of the climate system.

Following the chain of causality as described in Section 3, we have developed a simplified, linear and easily tuneable model that can be utilized to analyze the climate effect of different polluters, different emissions scenarios and different policy objectives, but also the effect of the system's climate adaptation and variations within these model parameters.

Part II

Milestone 2

CO₂-equivalence for non-CO₂ emissions

5 The effect of lifetime and radiative forcing efficiency of a GHG

5.1 General considerations

Greenhouse gasses (GHGs) can be classified as (i) cumulative pollutants that do not decay on the timescale of interest in climate policy (i.e., only CO₂), (ii) long-lived (LLCF, long-lived climate forcers), when their life time is in the order of centuries (e.g., N₂O), (iii) short-lived (SLCF), when their lifetime is in the order of one to two decades (e.g., CH₄), and (iv) very short-lived (VSLCF, this is a new acronym introduced in this study for convenience), when their life time is in the order of days or months (e.g., aviation non-CO₂ pollutants).

GHGs, i.e., climate forcers, cause radiative forcing, hence an impact on the temperature anomaly and on the climate. A change in radiative forcing due to a climate forcer is approximately proportional to a change in its atmospheric concentration, or abundance, and to its specific radiative efficiency, which is a molecular property of that substance. Its change in concentration over a given time interval is obtained as a convolution integral (a linear operator) of its amount emitted during the same time interval, as discussed in Part I. Therefore the larger the emissions and the radiative efficiency, the larger the climate impact of that climate forcer. This looks obvious, but the effect of the lifetime of the climate forcer is subtler and should not be ignored when conceptualizing the behavior and the impact of different climate forcers. The longer the lifetime of a climate forcer, the larger its accumulation before it is removed via chemical degradation, hence the larger its climate impact. For similar amounts of emissions and similar radiative efficiencies the longer-lived climate forcer has a larger climate impact than the shorter-lived one. This is demonstrated with the following simple calculations, whose results are illustrated in Figure 4a and in Figure 4b.

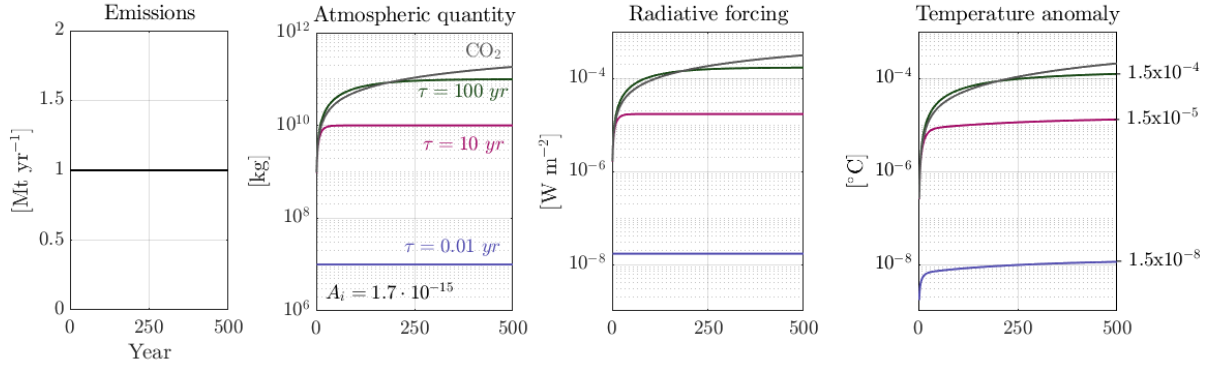
In Figure 4a the concentration, radiative forcing and temperature anomaly are calculated for CO₂ and for three climate forcers, all with the same radiative efficiency ($A = 1.7 \times 10^{-15} \text{ Wm}^{-2}\text{kg}^{-1}$, equal to that of CO₂), but with different lifetimes, namely $\tau = 0.01 \text{ yr}$, $\tau = 10 \text{ yr}$ and $\tau = 100 \text{ yr}$; these are not real compounds, but their lifetimes are similar to that of a VSLCF among those emitted by flights, to that of methane, and to that of nitrous oxide, respectively. The emission profile is the same for all, and corresponds to a step change from 0 to a constant value of 1 Mt/yr.

In Figure 4b the concentration, radiative forcing and temperature anomaly are calculated for four fictitious climate forcers, all with the same lifetime and emission profile, namely $\tau = 100 \text{ yr}$ and 1 Mt/yr, respectively, but different radiative efficiencies, namely from $A = 1.7 \times 10^{-15} \text{ Wm}^{-2}\text{kg}^{-1}$ to $A = 1.7 \times 10^{-9} \text{ Wm}^{-2}\text{kg}^{-1}$, each one hundred times larger than the previous.

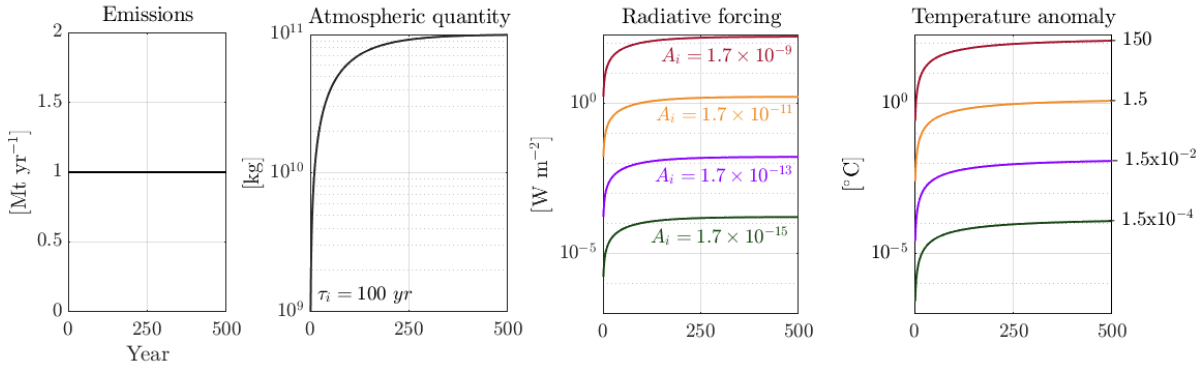
A few remarks are worth making.

- For same constant level of emissions and same lifetime the concentration stabilizes at the same level (see second panel from the left in Figure 4b). But the concentration stabilizes at different levels for non-CO₂ climate forcers that are emitted at the same rate but have different lifetimes (see second panel from the left in Figure 4a). The steady state concentration is that, at which the emission rate equals the rate of decay, which is lower for shorter-lived climate forcers. Such steady state concentration is attained sooner or later the shorter or the longer the lifetime of the climate forcer (see second panel from the left in Figure 4a).

- CO₂ reaches neither a steady state concentration nor a steady state radiative forcing as it accumulates in the atmosphere (see second and third panel from the left in Figure 4a).
- Radiative forcing follows concentration for climate forcers with the same radiative efficiency (third panel from the left in Figure 4a), while it scales with radiative efficiency when it differs (third panel from the left in Figure 4b).
- Temperature anomaly follows radiative forcing, but its time scale is longer, hence its time evolution is that from the three-layer climate model (Section 3.5) summed to the lifetime of the climate forcer (fourth panel from the left in Figure 4a). Also in this case CO₂ behaves differently since its lifetime is infinitely long, hence longer even of the timescale of the temperature anomaly (fourth panel from the left in Figure 4a).
- The final steady state temperature anomaly is determined by the final constant forcing values, following Equation (26).
- Changes in short-lived climate pollutants' emission rates have a dominant impact on the temperature response while those emission rates are changing. However, over the long term, the temperature response is primarily governed by the system's adjustment to the climate impact of previous emissions. This adjustment involves the transfer of excess heat from the surface to the deep oceans, a process that occurs on the order of magnitude of centuries.
- When there is a substantial momentary cooling, and the final constant forcing level is sufficiently low, the rate of change of temperature (dT_s/dt , as expressed in Equation (19)) becomes negative, and the steady-state temperature value (Equation (26)) is reached from above. Conversely, if there is a momentary temperature decrease due to reductions in short-lived climate pollutant emissions rates, but the final constant forcing level is not sufficiently low, dT_s/dt remains positive, and the temperature anomaly eventually increases again, reaching the steady state from below.
- One can use Figure 4a to conceptualize the behavior of methane and nitrous oxide, which have similar radiative efficiency and lifetime of about 10 and about 100 years, respectively. Same emissions of these two gases yield higher atmospheric abundance, radiative forcing and climate impact for nitrous oxide than for methane. It is worth noting that in the case of the Swiss agriculture two thirds and one third of the climate impact are due to methane and nitrous oxide, respectively.



(a) Concentration, forcing and temperature anomaly given same emissions of CO_2 (a cumulative polluter, a long-lived GHG ($\tau = 100 \text{ yr}$), a short-lived on ($\tau = 10 \text{ yr}$) and a very short-lived polluter ($\tau = 0.01 \text{ yr}$). The radiative forcing efficiency and molar mass of all pollutants are set equal to those of CO_2 , namely $A_i = 1.7 \times 10^{-15} \text{ Wm}^{-2}\text{kg}^{-1}$ and $MM = 44.01 \text{ g/mol}$ respectively.



(b) Concentration, forcing and temperature anomaly given same emissions of a long-lived GHG ($\tau = 100 \text{ yr}$) with radiative forcing efficiency varying from $A_i = 1.7 \times 10^{-15}$ to $1.7 \times 10^{-9} \text{ Wm}^{-2}\text{kg}^{-1}$. The molar mass of all pollutants is set equal to $MM = 44.01 \text{ g/mol}$.

Figure 4. Effect of the lifetime (τ) and radiative forcing efficiency (A_i) of a pollutant on the forcing and hence temperature anomaly it generates.

5.2 Swiss agriculture as a concrete example

The consequences of the general considerations above are clearly visible in Figure 5, where the results of simulations of the impact of methane, nitrous oxide and carbon dioxide emissions from the Swiss agriculture sector are presented.

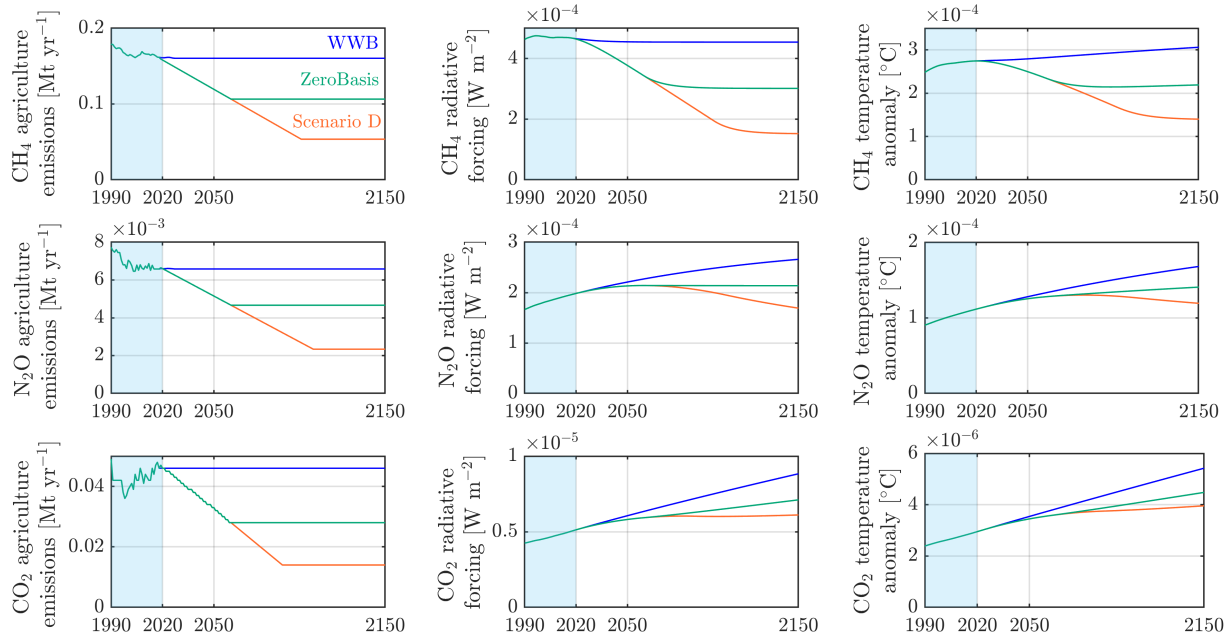


Figure 5. Emissions of CH₄, N₂O and CO₂ are shown in the first column from top to bottom, respectively. Their resulting radiative forcing is plotted in the second column, followed by the caused temperature anomaly in the third column. The three considered future scenarios, namely WWB, ZeroBasis and Scenario D, are shown in their respective colors, blue, green and orange. The curves are simulated for emissions starting from 1690 and are shown from 1990 to 2150; the region of past emissions is shadowed in light blue.

Here the three gasses behave differently for the same trend of emissions projections. Starting from the WWB blue scenario, where GHG emissions remain constant from now onward, it is possible to observe that constant CO₂ emissions result in a continuously increasing radiative forcing, and hence climate impact, as a result of the cumulative nature of this pollutant. For the constant WWB projections of CH₄ and N₂O, the generated radiative forcing differential stabilizes to a constant value on a shorter and longer timescale, respectively, as a result of their different life times.

In the ZeroBasis projection, where emissions of all pollutants continuously decrease from now until 2060 and are held constant afterwards, it can be observed that the radiative forcing of the short-lived CH₄ quickly adapts to follow the trend in the emissions. For N₂O this behavior cannot be detected and the radiative forcing perturbation keeps increasing despite decreasing N₂O emissions. This is because the long life time of nitrous oxide results in a sluggish behavior of this GHG, where the transient phase towards achieving the first radiative forcing equilibrium due to increasing historical N₂O emissions is not yet finished. The reduction in emissions helps however to reduce the final radiative forcing steady state level, explaining why also for N₂O the ZeroBasis radiative forcing is lower than that of WWB. A similar behavior can be witnessed for CO₂, where however the radiative forcing keeps increasing at a steeper rate as long as emissions are positive.

Lastly, in the Scenario D projection, where emissions further decrease after 2060, the radiative forcing of CH₄ again quickly adapts to follow the trend in the emissions. For N₂O, the reduction in emissions is in this case enough to counterbalance the sluggish behavior with which the radiative forcing of N₂O was still increasing from past emissions (before 2020), resulting therefore in an overall reduction of the radiative forcing. Finally, the radiative forcing of CO₂ is found again to increase, even if at a much reduced rate now. In fact, only if CO₂ emissions were to become zero and maintain that level for a sustained time, the

radiative forcing curve of this GHG would reach a steady state, correspondent to the level of carbon dioxide concentration accumulated in the atmosphere.

Moreover, important to notice is that the temperature anomaly stabilization occurs on a longer timescale than that required by radiative forcing to stabilize; this delay is a key feature of the climate system and can be explained by the heat transfer mechanisms involved. The delayed adjustment of temperature anomalies is due to the presence of both short and long characteristic timescales in the climate system's response to radiative forcing perturbation. These timescales are mathematically described by Equation (21), which governs the temperature response.

- **Short Timescale (Immediate Response):** The short timescale reflects the almost immediate impact of radiative forcing perturbations on the energy balance of the upper thermal layer of the Earth. In other words, changes in radiative forcing affect the surface temperature relatively quickly.
- **Long Timescale (Deep Ocean Adjustment):** The long timescale is a consequence of the much slower transfer of excess heat into the deep ocean. The deep ocean acts as a thermal buffer, absorbing heat over an extended period. This means that even after radiative forcing has been altered by anthropogenic greenhouse gas emissions, the climate system remains out of equilibrium for a long time.

The delayed adjustment of temperature to changes in radiative forcing is a fundamental aspect of climate science. It highlights the inertia of the climate system and the long-term consequences of greenhouse gas emissions. Understanding these timescales is crucial for assessing the long-term impacts of emissions and developing effective climate policies.

6 Results for the Swiss agriculture sector

6.1 Data collection

This section details the data collection process and the construction of future and historical scenarios for greenhouse gas (GHG) emissions from the Swiss agriculture sector.

In Figure 6, we present the time series of methane (CH_4), nitrous oxide (N_2O), and carbon dioxide (CO_2) emissions from Swiss agriculture. These emissions data span from 1690 and extend into projections until 2150. Notably, methane and nitrous oxide emissions from Swiss agriculture reached their peak around 1990, gradually decreasing by slightly more than 10% until 2000. Since then, they have maintained a relatively stable plateau. In contrast, carbon dioxide emissions experienced a peak around 1980, followed by a rapid 20% decrease until 1990, and by a further increase, resulting in a new peak.

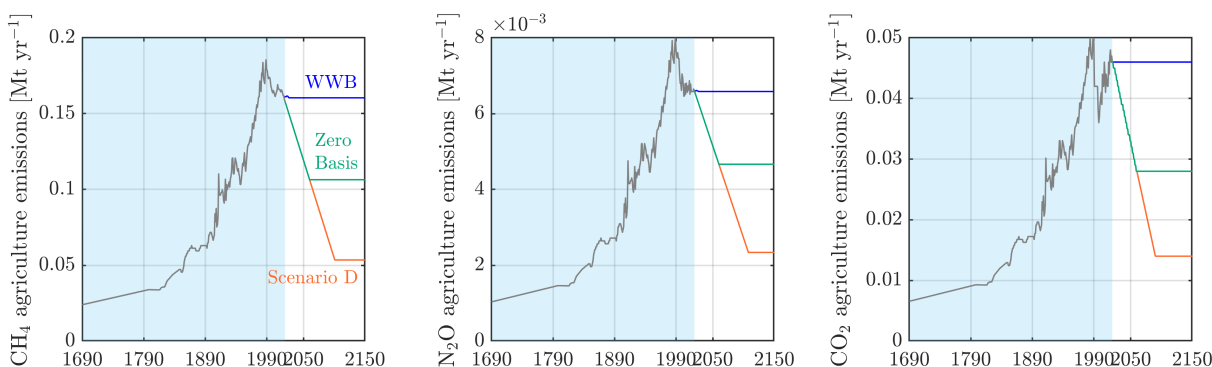


Figure 6. Methane (CH_4), nitrous oxide (N_2O) and carbon dioxide (CO_2) emission profiles of the Swiss agriculture sector. Past emissions (from 1690 to 2020) are highlighted by a light blue background, while three different projections are shown for future emissions: WWB (“Weit Wie Bisher”, in blue) a business as usual scenario where emissions are kept constant after 2020, ZeroBasis (in green) where emissions are decreased until 2060 and then kept constant afterwards, and Scenario D (“Deeper reduction”, in orange) where emissions follow the ZeroBasis scenario until 2060, but further decrease until a level of emissions that is half that of 2060 is reached. The WWB and ZeroBasis projections are taken from the *Energieperspektive 2050+* (EP2050+), while Scenario D is further provided for comparison purposes.

6.1.1 Historical scenario (1690-1990)

The emissions data for agriculture from 1848 to 1989 were calculated by analyzing the volume-index of the total production value of the agricultural sector in Switzerland. The volume-index values were sourced from the document titled “Landwirtschaftliche Gesamtrechnung: Produktionswert der Landwirtschaft: historische Zeitreihen” (document code: je-d-07.04.02.08). It is assumed that emissions scale proportionally with the volume-index, which had a value of 102.3 in 1990. The resulting historical data for agriculture emissions aligns well, both in terms of trend and magnitude, with the estimations published in the 8th Swiss National Communication. For the period from 1690 to 1847, emission estimations are based on the population numbers in Switzerland. This approach operates under the assumption that emissions are correlated with production volume and that the volume-index is associated with population changes.

6.1.2 Data points (1990-2019)

Data point from 1990 to 2019 are taken from the *EP2050+ Ergebnissynthese*²⁰, as reported by *Tabelle 02: Entwicklung der Treibhausgasemissionen nach CRF-Kategorie*.

6.1.3 Future projections (2020-future)

In this study, future projections for agriculture emissions are based on scenarios from the *EP2050+ Ergebnissynthese*, specifically the WWB and ZeroBasis scenarios. The WWB scenario, represented in blue, is a business-as-usual projection, where emissions remain constant from 2020 to 2060. The ZeroBasis scenario, shown in green, involves emissions reductions until 2060, and stabilization thereafter. The projected data points from 2020 to 2060 are collected from the *Tabelle 02: Entwicklung der Treibhausgasemissionen nach CRF-Kategorie* of the corresponding EP2050+ scenarios. For agriculture, the EP2050+ ZERO-A, ZERO-B and ZERO-C scenarios are not presented as they project the same levels of CO_2 , N_2O and CH_4 emissions as the ZeroBasis case.

In this work we also extend the time further into the future (until 2150, or 2300) to assess the climate impact of the specific Swiss agriculture on a longer time horizon. This is done by keeping the emissions value

constant from 2060 onward for each scenario.

For comparison purposes, an additional scenario called Scenario D (“Deeper emissions reduction”) is included. In this scenario, emissions follow the ZeroBasis trajectory until 2060 but continue to decrease until they reach a level that is half of the 2060 emissions level. This scenario provides insights into the climate impact of deeper emissions reductions.

The analysis conducted in Milestone 2 regarding the CO₂-equivalences of non-CO₂ emissions from the Swiss agriculture sector is based on the data collected, calculated, or projected as previously described. While it is possible that different or updated datasets may be considered in the future, it is important to note that the fundamental reasoning and key observations drawn from the results of Milestone 2 are not expected to change significantly. This is because the three projected scenarios already encompass a wide range of potential climate impacts associated with the Swiss agriculture sector.

6.2 From emissions to radiative forcing and temperature anomaly

In this section, we report and discuss the emissions, CH₄, CO₂ and N₂O, the radiative forcing, and the temperature anomaly caused by the agriculture sector in Switzerland starting in 1690 and projected into the future based on the historical data mentioned above and according to the three future scenarios described above.

Figure 7, left panel, shows the total emissions, which scale in mass terms approximately as follows: CH₄ emissions are ten times those of CO₂, which are ten times those of N₂O (see Figure 6 for the individual emissions). From the specific emissions of each pollutant, $E_{i,s}(t)$, the corresponding specific atmospheric concentration differential, $\Delta c_{i,s}(t)$, is calculated using Equation (13). Following the chain of causality presented in Milestone 1, the atmospheric concentration of each pollutant is then used to obtain the differential radiative forcing perturbation, $\Delta F_{i,s}(t)$, as shown in Equation (14). The specific radiative forcing perturbations are summed to find the overall impact induced by the Swiss agriculture sector, as a result of its CH₄, N₂O and CO₂ emissions, which is plotted in Figure 7, middle panel. This total radiative forcing perturbation is, in turn, used to calculate the final contribution of Swiss agriculture to the total temperature anomaly, shown in Figure 7, right panel. Here the timeline is extended to 2300 in order to better visualize the longer time scale required by the temperature anomaly to stabilize after radiative forcing has been altered by anthropogenic GHG emissions. Discussion on the specific forcing and warming perturbation generated by each pollutant is provided in Section 5. It is worth noting that because of the different features of the three GHGs emitted by agriculture practices, two thirds of the climate impact (radiative forcing and temperature anomaly) is approximately due to methane, while only one third is due to nitrous oxide, with the CO₂ being negligible. The swap in climate impact importance between N₂O and CO₂ when going from rate of emissions and radiative forcing is remarkable, and is a consequence of their very different radiative efficiency (A_i of the different agriculture-induced pollutants are reported in ??).

Let us now look at the total radiative forcing in the different scenarios, which comes from the superposition of the methane and nitrous oxide forcings as shown in Figure 6:

- WWB and Scenario D experience a continual increase and decrease, respectively, of the radiative forcing until 2300, primarily due to the slow response of N₂O forcing to emission changes. In fact, in both scenarios CH₄ forcing quickly stabilizes to follow the emissions pathway, but N₂O forcing keeps increasing in WWB, and respectively decreasing in Scenario D.
- ZeroBasis scenario shows an initial decrease in the total forcing perturbation, which is driven by short-lived methane forcing reduction to follow the decrease in emissions. From 2100, total ZeroBasis radiative forcing maintains a stable plateau as both CH₄ and N₂O forcings remain constant; the stability

of the latter is also a result of emissions reduction, which are however not enough to decrease forcing (as would be in Scenario D).

Finally, looking at the total temperature anomaly curves, it is clear that stabilization of temperature anomaly takes longer compared to radiative forcing (especially evident in the ZeroBasis case). Worth discussing is the temperature anomaly minimum in the ZeroBasis scenario:

- The final constant forcing value after 2060 leads to a final steady-state temperature anomaly higher than the local warming minimum.
- The final steady state temperature anomaly associated with the ZeroBasis scenario is also higher than the warming value in 1990, even if emissions were higher at that time. This is because the warming level reached in 1990 was not yet the steady state value associated to the emissions of that time; that steady state temperature anomaly is the one of the WWB scenario.

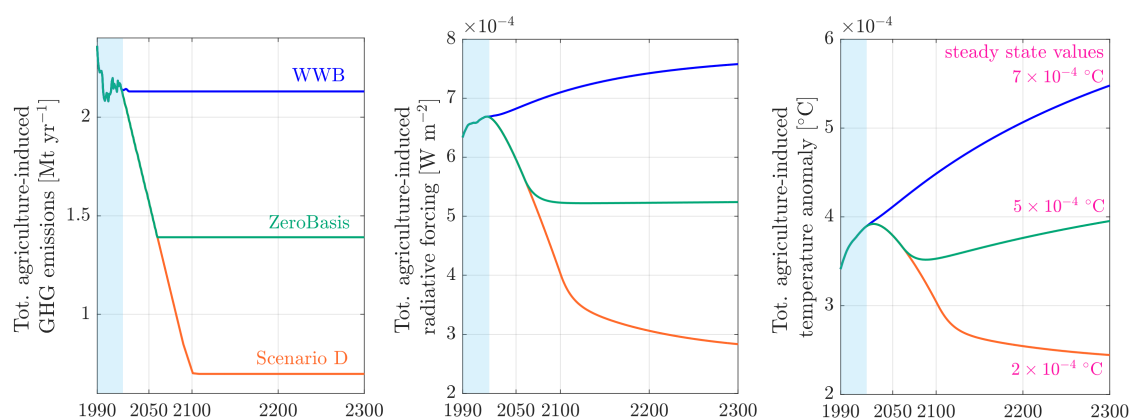


Figure 7. Total curves of radiative forcing perturbation and temperature anomaly as a result of the CH₄, N₂O and CO₂ emissions from Swiss agriculture practices since 1690. The three considered future scenarios, namely WWB, ZeroBasis and Scenario D, are shown in their respective colors, blue, green and orange. The curves are shown from 1990 to 2300. The extended timeline is chosen to better visualize the longer time scale required by the temperature anomaly to stabilize after radiative forcing has been altered by anthropogenic GHG emissions. Long-term steady state temperature anomalies are shown in pink.

7 Results for the Swiss aviation sector

7.1 Data collection

Data collection and construction of future and historical scenarios for the climate forcers emissions from the Swiss aviation sector (international flights) are presented in this section.

The time series of emissions encompassing CO₂, NO_x, SO_x, BC (black carbon), and H₂O from Swiss aviation, spanning from 1950 to projected figures until 2150, are graphically displayed in Figure 6. It is worth noting that emissions of methane and nitrous oxide stemming from aviation practices are negligible and are not included in this report. Furthermore, it is important to highlight that, contrary to agriculture, most GHG emission categories from aviation continue to experience an upward trajectory, with a projected peak in emissions expected in the future.

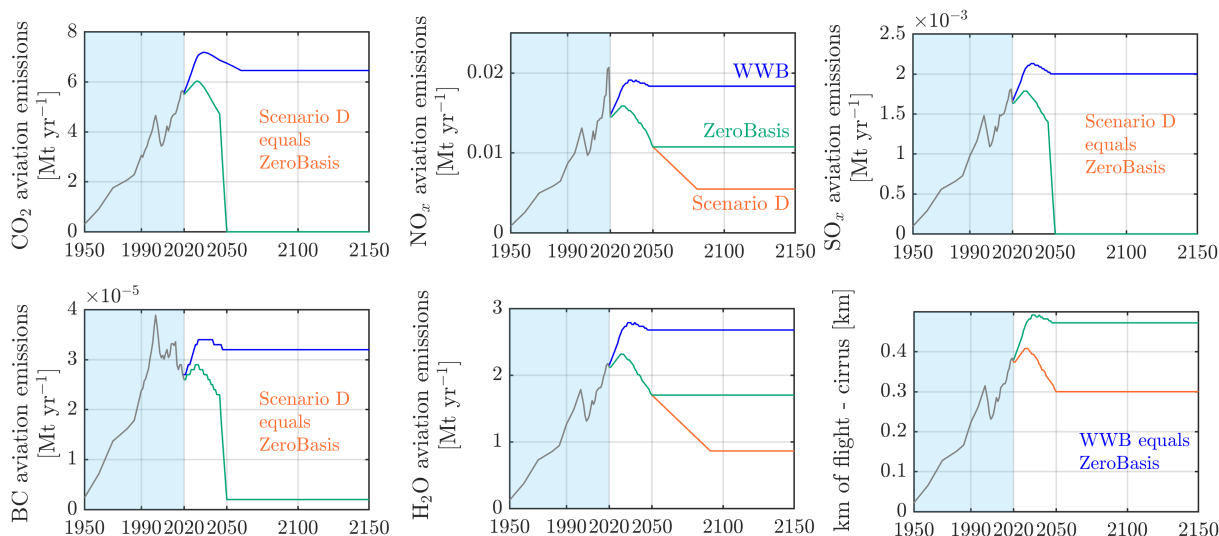


Figure 8. CO₂, NO_x, SO_x, BC and H₂O emission from the Swiss aviation sector, as well as the profile of kilometers of flights. Past emissions (from 1950 to 2020) are highlighted by a light blue background, while three different projections are shown for future emissions: WWB (“Weit Wie Bisher”, in blue) a business as usual scenario where emissions are kept constant after 2020, ZeroBasis (in green) where emissions are decreased until 2060 and then kept constant afterwards, and Scenario D (“Deeper reduction”, in orange) where emissions follow the ZeroBasis scenario until 2060, but further decrease until a level of emissions that is half that of 2060 is reached. The WWB and ZeroBasis projections are taken from the Energieperspektive 2050+ (EP2050+), while Scenario D is further provided for comparison purposes. For pollutants where the ZeroBasis scenario project a decrease in emissions to (approx.) zero no scenario D is provided. Lastly, the projected kilometers of flight in the WWB and ZeroBasis cases are the same.

7.1.1 Historical scenario (1950-1990)

Emissions data from 1950 to 1989 are calculated assuming that emissions scale with the number of landings and take-offs from national airports. Flight movements data is collected from the *Schweizerische Zivilluftfahrtstatistik 2021 - 4. Bewegungen*²¹ (document code: su-b-438-11.7.AV-e-4).

7.1.2 Data points (1990-2019)

The data for emissions of CO₂, NO_x, SO_x, BC, H₂O, and for air traffic volume in the Swiss aviation sector have been collected as follows:

- CO₂ data points from 1990 to 2019 have been sourced from the *EP2050+ Ergebnissynthese*²⁰, specifically from the report’s “Tabelle 02: Entwicklung der Treibhausgasemissionen nach CRF-Kategorie.”
- NO_x, SO_x, and BC emissions data spanning the years 1990 to 2019 have been obtained from Table T7.1 of the “Schweizerische Zivilluftfahrt - 7. Treibstoffverbrauch und Emissionen” (document code: su-b-438-11.7.AV-e-7). In cases where specific years lack measurement data, interpolation methods have been employed to estimate values for those years.
- H₂O emissions have been calculated by assuming a proportional relationship with aviation fuel consumption. This assumption is based on a factor of 1.2 kg H₂O per kg of fuel, as referenced in the literature^{6,11}. Data regarding aviation fuel consumption from 1990 to 2019 has been sourced from “Tabelle 6: Passagieraufkommen, Verkehrsleistung, Treibstoffverbrauch und THG-Emission von internationalen Flügen” in the *EP2050+ Ergebnissynthese* report²⁰.

- The number of kilometers of air traffic volume, necessary for calculating the radiative forcing associated with cirrus clouds, has been estimated based on the amount of aviation fuel consumed in the WWB scenario. This estimation takes into account a fuel consumption parameter per passenger and per 100 kilometers, as well as passenger data retrieved from "Abbildung 10: Entwicklung Luftverkehr" in the EP2050+ "Technischer Bericht: Abbildungen und zugehörige Daten - Kap. 1-7"²⁰.

7.1.3 Future projections (2020-future)

For the projection of future CO₂ emissions in the Swiss aviation sector, we have considered two scenarios: the WWB and ZeroBasis scenarios from the EP2050+ *Ergebnissynthese*²⁰. Data points from 2020 to 2060 have been obtained from "Tabelle 02: Entwicklung der Treibhausgasemissionen nach CRF-Kategorie" in the corresponding EP2050+ scenarios. Additionally, we extended the time frame beyond 2060 to assess the climate impact of the Swiss aviation sector on a longer horizon. In these extended scenarios, emissions are held constant from 2060 onward.

For emissions of NO_x, SO₂, BC, and H₂O from aviation, we assumed a scaling relationship with aviation fuel consumption. Fuel consumption projections from 2020 to 2050 under the WWB scenario were collected from "Tabelle 6: Passagieraufkommen, Verkehrsleistung, Treibstoffverbrauch und THG-Emission von internationalen Flügen" in the EP2050+ *Ergebnissynthese* report²⁰. Beyond 2050, fuel consumption data points were assumed to remain constant.

The estimation of air traffic volumes (kilometers travelled) is derived from projected fuel consumptions, taking into account a fuel consumption parameter per passenger and per 100 kilometers, as well as projected passenger numbers. Within the ZeroBasis scenario, a more optimistic assumption regarding the annual increase in transport energy efficiency is applied from 2020 onward compared to the WWB scenario. This accounts for the decrease in expected fuel consumption in the ZeroBasis scenario while keeping the number of passengers and flight distances the same as in the WWB projections.

For comparison, we have introduced an additional scenario labeled "Scenario D" (Deeper emissions reduction). In this projection, GHG emission levels follow the ZeroBasis scenario until 2060 but continue to decrease steadily until emissions reach a level that is half of the 2060 value. For pollutants where the ZeroBasis scenario projects emissions to decrease to approximately zero (e.g., BC, SO_x, and CO₂), no Scenario D is provided.

It is important to note that the Milestone 2 analysis on CO₂-equivalence between non-CO₂ and CO₂ emissions from the Swiss aviation sector has been conducted based on the emission data collected, calculated, or projected as described above. While it is possible that different or updated datasets may be considered in the future, the fundamental reasoning and key observations from the results of Milestone 2 are unlikely to change significantly.

7.2 From emissions to radiative forcing and temperature anomaly

Figure 9, left panel, reports the total GHG emissions, kilometers of air traffic volumes (related to cirrus clouds formation), radiative forcing and temperature anomaly caused by the aviation sector in Switzerland.

To determine the overall climate impact of the Swiss aviation sector, we can sum the radiative forcing perturbations caused by all forcers, following the superposition principle discussed above. This allows us to assess the combined impact of CO₂, NO_x, SO_x, BC, H₂O, and cirrus emissions from Swiss aviation practices since 1950. The total curves of forcing and temperature perturbation resulting from Swiss aviation activities are presented in Figure 9, middle and right panels, respectively. The timeline is extended to 2300 to visualize

the longer timescale required for the temperature anomaly to stabilize after radiative forcing has been altered by anthropogenic greenhouse gas emissions. Discussion on the specific forcing and warming perturbation generated by each pollutant is provided in Appendix B.2.1.

Analyzing the radiative forcing curves for different scenarios, several trends become evident:

- In the WWB scenario (blue), radiative forcing exhibits a continuous increase throughout the coming centuries. This increase can be mostly attributed to the ongoing rise in perturbation caused by CO₂ emissions, which accumulate over time.
- The ZeroBasis scenario (green) experiences a somewhat rapid decrease in radiative forcing after 2050. This decline can be primarily attributed to the short-lived pollutants from aviation practices, which exhibit a swift response to emission reductions. After the initial drop, radiative forcing in the ZeroBasis scenario slowly decreases in the following centuries. This behavior is linked to the radiative forcing of CO₂, which, after cease of emissions due to the EP2050+ ZeroBasis assumption of 100% implementation of SAFs, is still affected by the partitioning of atmospheric CO₂ into other terrestrial compartments. Although this decrease is gradual, it contributes to the slow reduction in radiative forcing over time, ultimately reaching a steady state level from above.
- Scenario D (orange) follows a radiative forcing trajectory similar to that of the ZeroBasis projection over the long run. This similarity arises from the fact that emissions of CO₂ in Scenario D match those in the ZeroBasis projection. However, Scenario D exhibits a more pronounced reduction in radiative forcing compared to ZeroBasis. This reduction is attributed to the greater expected decrease in emissions of NO_x, H₂O, and cirrus formation in Scenario D.

Let us now consider the temperature anomaly curves:

- In the WWB scenario, the temperature anomaly continuously increases due to the ongoing rise in radiative forcing. This increase is a direct consequence of the cumulative emissions of CO₂.
- Both the ZeroBasis and Scenario D scenarios experience a decrease in temperature anomalies from 2050 to approximately 2100 (less and more pronounced, respectively). This decline results from reduced emissions of short-lived non-CO₂ pollutants, which have a swift impact on temperature with a similar trend. However, in the long run, both scenarios show a renewed increase in temperature. This long-term warming is primarily driven by cirrus clouds, followed by NO_x emissions. The reduction in emissions projected by these scenarios is insufficient to maintain the achieved momentary cooling effect.

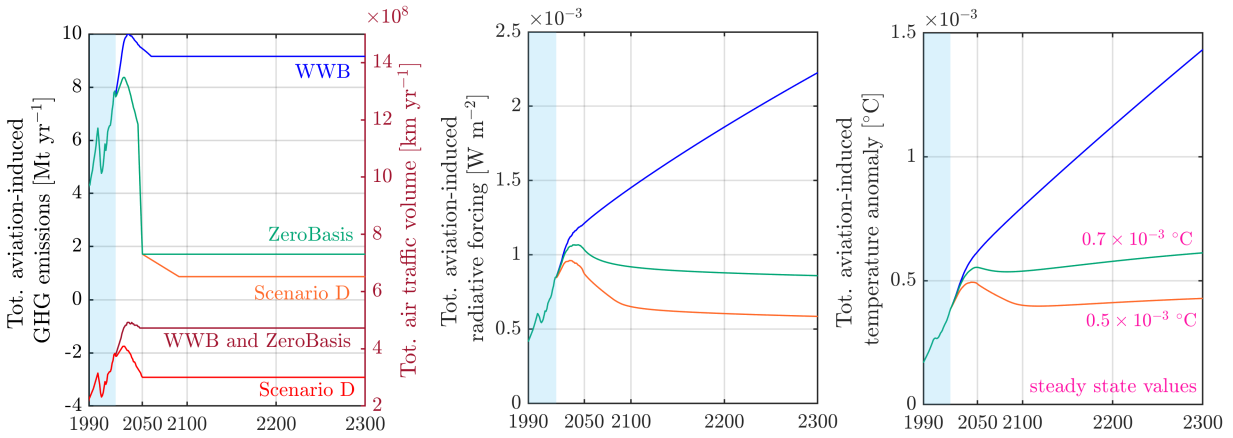


Figure 9. Total curves of radiative forcing perturbation and temperature anomaly as a result of the CO₂, NO_x, SO_x, BC and H₂O emissions, as well as cirrus clouds formation, from Swiss aviation practices since 1950. The three considered future scenarios, namely WWB, ZeroBasis and Scenario D, are shown in their respective colors, blue, green and orange. The curves are shown from 1990 to 2300. The extended timeline is chosen to better visualize the longer time scale required by the temperature anomaly to stabilize after radiative forcing has been altered by anthropogenic GHG emissions. Long-term steady state temperature anomalies are shown in pink for ZeroBasis and Scenario D; in the WWB case, forcing and temperature anomaly do not stabilize a result of the continued CO₂ emissions.

Worth highlighting is that of the total mass of GHG emissions, CO₂ and H₂O are the primary contributors. These pollutants are emitted in substantial quantities by aviation practices. However, when considering radiative forcing, which directly affects the climate impact, the primary contributors are CO₂, NO_x, and cirrus clouds. These pollutants have a significant impact on warming. The impact of H₂O is less than 10% and that of SO_x and BC can be neglected. Visual representation of this is provided in Appendix B.2.2.

Part III

Milestone 3 -

Demand for negative emissions: A case study

8 Determining CDR requirements

In this section, emissions data from the Swiss agriculture sector is utilized to build an example scenario of emissions reduction together with deployment of CDR to achieve the Paris Agreement target of net-zero emissions in 2050. The CDR necessary to convert the agriculture methane and nitrous oxide emissions into CO₂-equivalents and required to comply with the reference objective scenario is calculated by means of the different equivalence metrics, namely GWP₂₀, GWP₁₀₀, GWP*, as well as using the LWE approach.

The example scenario defines a "top-down" profile for emissions reduction, where emissions need to be reduced by 50% in 2030 compared to 1990 levels and reach a 100% reduction by 2050, in alignment with the Paris Agreement. This top-down curve is represented by the black line in Figure 10. Additionally, a "bottom-up" profile is outlined, which is defined as the maximum decarbonization and GHG reduction expected for Swiss agriculture as to the EP2050+ ZeroBasis scenario (green curve in Figure 10).

It is obvious that there is a gap between the two emissions profiles, which is quite general of sectors where emissions are hard-to-abate. In other words, top-down net-zero pledges reflecting a must-do approach ("what we want", $E_{top-down}$, showed by the black curve of target emissions reduction) require more ambitious climate actions than the bottom-up decarbonization measures reflecting a can-do attitude ("what we can", $E_{bottom-up}$, showed by the green curve), which reflect past experience of gradual sectoral transformation. In a nutshell, the climate emergency requires unprecedented speed in taking climate action. Such gap needs to be filled by generating carbon dioxide removal quantities (CDR) and/or by purchasing emissions avoidance certificates. In the scope of this study, the gap between emissions of the bottom up curve and target reductions set by the top-down curve, highlighted in light blue in Figure 10, defines the CDR requirements (shown as a light blue area in Figure 10):

$$E_{CDR}(t) = E_{bottom-up}(t) - E_{top-down}(t) \quad (33)$$

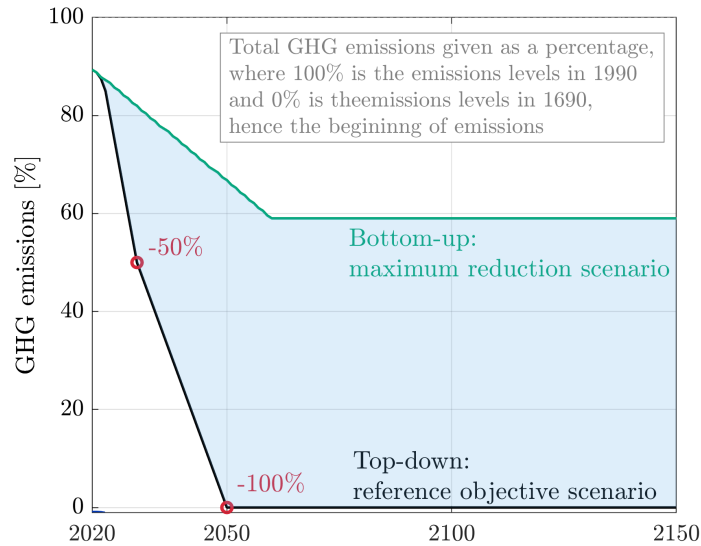


Figure 10. Top-down, example curve of target emissions reduction in line with a reference objective scenario (in black). Bottom-up curve of maximum projected emissions reduction, here specifically the EP2050+ ZeroBasis scenario of emissions reduction from the Swiss agriculture sector (in green). The difference between the green and black curves define the carbon dioxide removal required in order to comply with the emissions reduction targets set by the top-down curve. The left vertical axis shows the total GHG emissions from agriculture, namely emissions of CH₄, N₂O and CO₂, as a percentage of the total emissions levels in 1990 (100% corresponds to the total value of emissions in 1990, and 0% corresponds to the total value of emissions at the beginning of the climate activity of agriculture, i.e. 1690).

The following analysis will provide a comparative assessment of these equivalence metrics within the context of a CDR compensation strategy, specifically for the example of Swiss agriculture and its emissions reduction target defined by the top-down curve. The conclusions drawn from this analysis regarding the suitability of different equivalence metrics for CDR scenarios can also be applied to other emissions scenarios for the same sector and to other sectors.

9 The impact of different equivalence approaches on CDR requirements: simulations for the Swiss agriculture sector

As illustrated in Figure 41, the climate impact of Swiss agriculture is primarily attributed to methane (CH₄), accounting for approximately two-thirds of the impact, and nitrous oxide (N₂O), contributing to one-third of the impact. Over time, the relative contribution of nitrous oxide increases compared to methane. Carbon dioxide (CO₂) emissions from agriculture have a negligible climate impact.

Given the challenges associated with reducing certain emissions from agriculture, as demonstrated in Figure 10 and reiterated in Figure 11, there is a need for carbon dioxide removal (CDR) to offset both agricultural CO₂ emissions and non-CO₂ emissions. To quantify the required CDR deployment, we consider four equivalence approaches introduced in previous sections: the GWP₁₀₀ and GWP₂₀ metrics, and the GWP* and LWE models. The corresponding CO₂ removal values to compensate for the residual agricultural CO₂ and non-CO₂ emissions, as calculated using these approaches, are shown in Figure 11. These values are represented by the dashed-dotted line for GWP₁₀₀, the dashed line for GWP₂₀, the dotted line for GWP*, and the solid line for LWE.

In the following analysis, we will examine the differences in CDR requirements resulting from these different equivalence metrics, providing insights into their implications for CDR strategies in the context of agricultural emissions reduction.

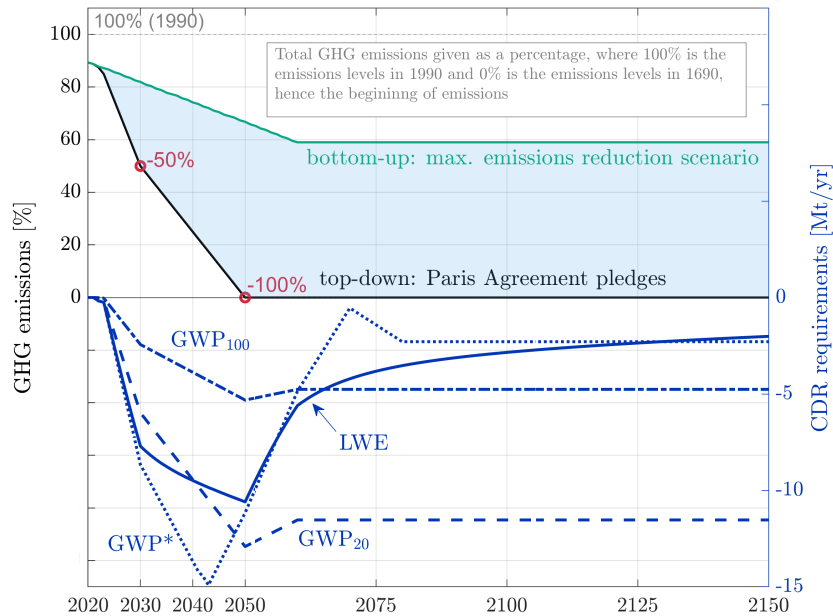


Figure 11. Determination of the CDR compensation strategy depending on the CO₂ equivalence approach employed in the calculations. Total GHG agricultural emissions (i.e. CH₄, N₂O and CO₂ emissions) to be compensated, hence the difference between the maximum reduction scenario (bottom-up curve) and climate targets in line with the reference objective scenario (top-down curve), are illustrated on the left vertical axis, as a percentage of the total emissions levels in 1990. The right vertical axis shows the yearly carbon dioxide removal, in negative values, required to compensate the blue area of residual emissions, as calculate by the different equivalence metrics to assess CO₂-equivalents for CH₄ and N₂O.

Only the deployment of CDR, as calculated by means of the LWE model, would ensure exact compensation of the climate impact (radiative forcing) of the light blue area, hence of the remaining agricultural emissions that need to be actively compensated in order to comply with the top-down emissions reduction targets. All other metrics (GWP_{20} , GWP_{100} and GWP^*) under- and overestimate the required CO₂ removal at some point in time.

The analysis of the CDR requirements, as calculated using different equivalence approaches, reveals important insights into the strategies for addressing agricultural emissions in the context of carbon dioxide removal. Here are the key observations:

- **LWE model:** When CDR is deployed according to the curve calculated with the LWE model, it ensures exact compensation of the radiative forcing and, consequently, the climate impact generated by the light blue area. The LWE model provides an accurate representation of the temporal dynamics of emissions and their impact, making it a suitable choice for precise CDR planning.
- **GWP₁₀₀ metric:** The GWP_{100} metric only matches the correct CO₂ equivalence calculation at specific points in time when its curve intersects with the LWE profile. Before this intersection, it underestimates the CDR requirement compared to the LWE metric. Afterward, it overestimates the CDR requirement. The GWP_{100} metric does not provide an accurate representation of the evolving emissions and radiative forcing, making it less suitable for long-term CDR planning.

- **GWP₂₀ Metric:** The GWP₂₀ metric exhibits a similar behavior to GWP₁₀₀ but with a shorter time frame. It matches the correct CO₂ equivalence calculation at an earlier point in time when it intersects with the LWE profile. However, it still underestimates the CDR requirement before this intersection and overestimates it afterward. Like GWP₁₀₀, GWP₂₀ is not suitable for long-term CDR planning.
- **GWP* Model:** The GWP* model approaches the correct-LWE deployment but overreacts to discontinuous variations in the amount of residual emissions to compensate. While it provides a better estimate than GWP₁₀₀ and GWP₂₀, it still falls short of the precision offered by the LWE metric. GWP* may be a reasonable choice for CDR planning (upon correct calibration of this empirical metric, Appendix B.4) but may fall short in cases with significant emission fluctuations.

In summary, the choice of equivalence approach significantly impacts the calculation of CDR requirements to offset agricultural emissions. The LWE model provides the most accurate and consistent representation of emissions and radiative forcing over time, making it the preferred choice for CDR planning. GWP* generally provides a good enough estimate, when correctly calibrated.

The yearly rate of necessary CDR deployment in 2050, differs greatly for the different equivalence approaches. A GWP₁₀₀-CDR strategy results in approximately, 5 Mt/yr in 2050, underestimating the 9 Mt/yr of CO₂ removal indicated by the LWE model. The GWP* aligns well with LWE in 2050, while a GWP₂₀-CDR strategy would require 13 Mt/yr in 2050, due to the large and rapid overestimation in which this metric incurs when assessing the climate impact of methane and nitrous oxide.

It is also important to note, as highlighted in Figure 11, that not only does the extent of CDR deployment in 2050 change for different CDR strategies, but also the rate of CDR deployment strongly differs among equivalence metrics, with LWE and GWP* projecting a sharp increase early on (e.g. already from 2020 to 2030) compared to the other two metrics.

By means of the chain of causality and climate model introduced in Part I, the temperature anomaly curves corresponding to the different CDR strategies analyzed in Figure 11, are calculated and showed in Figure 12.

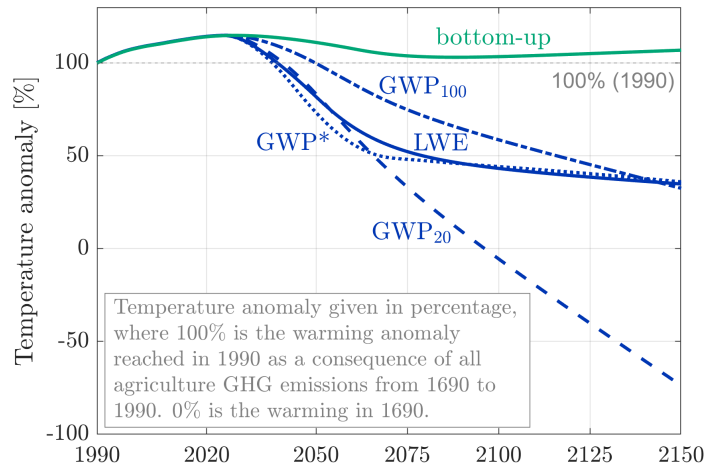


Figure 12. Temperature anomaly as a consequence of all agriculture emissions from 1690 onward, expressed in percentage of the warming in 1990 (where 100% corresponds to the warming in 1990 and 0% is the temperature anomaly in 1690, hence the beginning of agriculture anthropogenic activity). Temperature anomaly curves are shown for five different scenarios. The green curve shows the warming resulting from the EP2050+ ZeroBasis emissions scenario, where no CDR compensation is undergone (this curve corresponds to the green curve previously shown in Figure 7). The other four curves exhibit the development of the temperature anomaly, related to Swiss agriculture emissions from 1690 onward, when the GWP₁₀₀- (dashed-dotted line), GWP₂₀- (dashed line), GWP*- (dotted line) and LWE-CDR strategies (solid line) are implemented from 2020 onward. The metric-specific CDR strategies are shown in Figure 11.

Firstly, it is possible to observe that only following the ZeroBasis projected emissions reduction and deploying no CDR strategy to compensate for the residual emissions (green, bottom-up curve) would result only in a momentary decrease in the temperature anomaly, which however undergoes a renewed increase in the long run to reach the steady state, as previously discussed in Section 6.2. Instead, the climate impact of a Swiss CDR strategy, to align the agriculture sector to the top-down targets, highly differs depending on the equivalence metric implemented. Nevertheless, it is evident that all CDR strategies, regardless of the metric used, enable the anticipation and reduction of the peak temperature anomaly compared to the scenario without CDR.

Figure 12 clearly shows that LWE is the only metric allowing to perfectly stabilize the temperature anomaly to a constant value, as this is the only metric ensuring exact climate compensation of the light blue area pictured in Figure 11.

Instead, as mentioned above, GWP₁₀₀ strongly underestimates the required CO₂ negative emissions for a prolonged time, effectively increasing the temperature anomaly by approximately 20% on average and also slightly postponing the time of peak warming, compared to LWE. The temperature anomaly of the LWE-CDR strategy and that of the GWP₁₀₀-CDR strategy only cross around 2150. Afterwards, the temperature associated to the GWP₁₀₀-CDR strategy would continue to decrease linearly due to over-deployment of CO₂ removal. This can be clearly seen in the GWP₂₀-CDR strategy where the overcompensation with negative emissions starts sooner, as previously indicated in Figure 11. Here the temperature anomaly decreases rapidly, and somewhat uncontrollably, reaching the temperature values of 1690 (0%) around 2100 and plummeting below this level afterwards.

Overall, one might conclude that employing GWP₂₀ and GWP₁₀₀ metrics would undermine the effectiveness and stability of any CDR strategy, and hence climate policy.

Lastly, with a GWP*-CDR strategy the temperature anomaly can also be quite accurately stabilized to the asymptotic final value associated to the LWE-CDR strategy. It is important to highlight, however, that this is only the case for stable and continuous negative emissions requirements, as is the light blue area between 2050 and 2150 (Figure 11), paired with a correct calibration of the GWP* definition for long-lived climate forcers.

Looking at the cumulative carbon removal requirements, as shown in Figure 13, paints a rather challenging picture indicating an extremely large necessity of CDR deployment just to allow the Swiss agriculture sector to comply with reduction targets in line with the reference objective scenario and reach net-zero emissions in 2050 (top-down curve in Figure 10). Until 2050, just under 100 Mt of CO₂ removal would have been cumulatively required by a GWP₁₀₀-CDR strategy, while a LWE- and a GWP₂₀-CDR strategy would overlap at 200 Mt, followed by a GWP*-CDR strategy requiring just shy of 300 Mt, cumulatively.

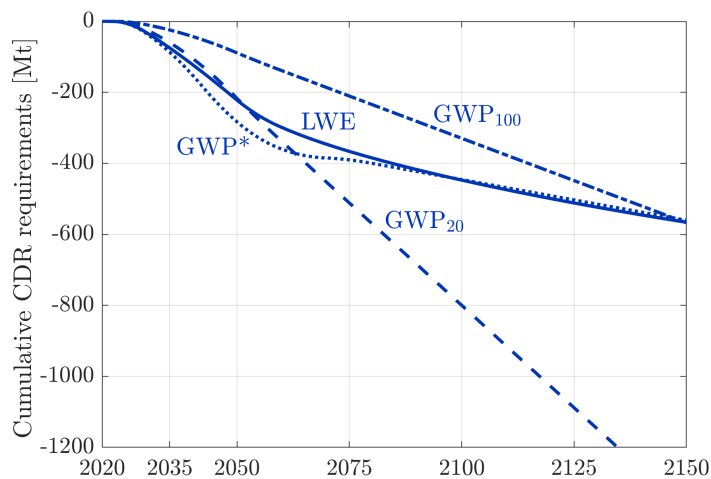


Figure 13. Cumulative CDR requirement, from 2020 to 2150, for the CDR strategies as following the four different equivalence metrics.

As previously mentioned and highlighted in Figure 11, the extent of carbon dioxide removal (CDR) deployment not only varies depending on the equivalence metric employed but also exhibits significant differences in the rate of CDR deployment until 2050. Specifically, the LWE and GWP* metrics project a more rapid deployment of carbon removal early on (e.g., from 2020 to 2030) compared to the other two metrics. This raises a critical question regarding the potential consequences for the temperature anomaly in the event that CDR cannot be deployed as rapidly as required by the CDR strategies outlined in Figure 11. This question is further explored in the following section.

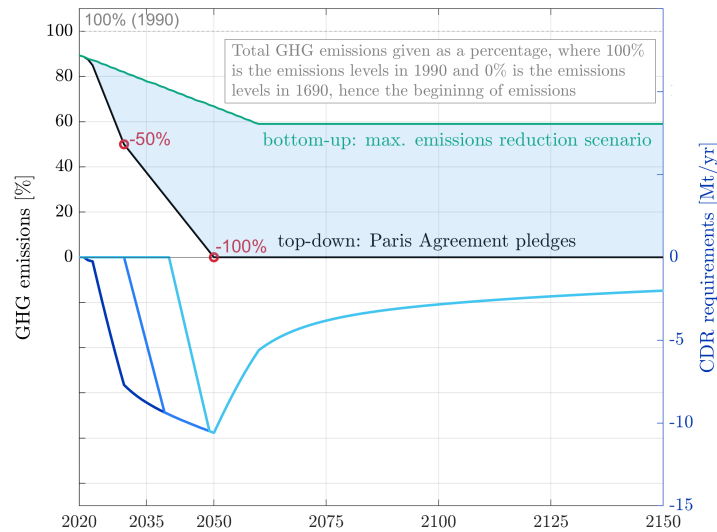
9.1 Delaying CDR intervention: the effect on the temperature anomaly

We analyze four cases of delayed CDR intervention:

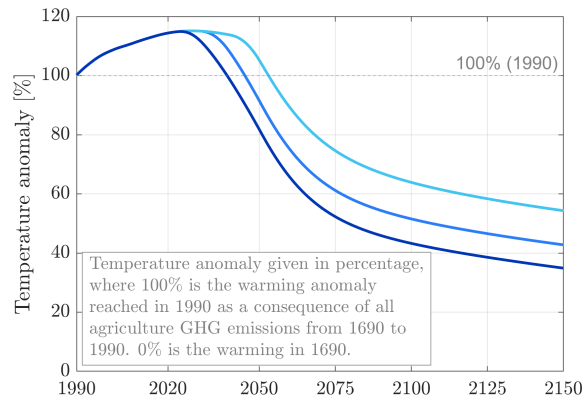
1. intervention is delayed until 2030, then regaining CDR deployment rate
2. intervention is delayed until 2040, then regaining CDR deployment rate
3. intervention is delayed until 2030, then regaining CDR deployment rate and cumulative CDR
4. intervention is delayed until 2040, then regaining CDR deployment rate and cumulative CDR

Analysis of delayed CDR deployment is performed only with the LWE model, for the sake of simplicity.

The first two cases of delayed compensation, and their respective temperature anomaly profiles, are showed in Figure 14 (in blue and light blue, respectively) together with the curve of prompt CDR deployment starting from 2020 (in dark blue).



(a) Delaying of CDR deployment



(b) Effect on the temperature anomaly

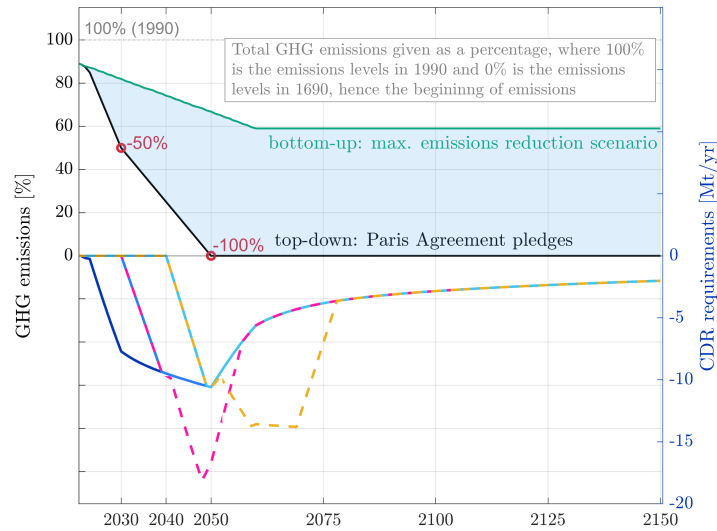
Figure 14. Delaying compensation by 10 years (i.e. until 2030, blue curve) and 20 years (i.e. until 2040, light blue curve), followed by CDR intervention with the same deployment rate as the case of prompt CDR (i.e. from 2020, dark blue curve). The effect that delaying CDR intervention has on the temperature anomaly is showed in subfigure (b).

Referring to Figure 14, it becomes evident that delaying carbon dioxide removal (CDR) compensation by 10 years (blue curve) and by 20 years (light blue curve) has a significant impact on the temperature anomaly. This delay results in an increase in the final asymptotic steady-state temperature. The reason for this is that the three CDR compensation strategies proposed in Figure 14a lead to different radiative forcing profiles, thereby implying distinct temperature anomalies and steady states.

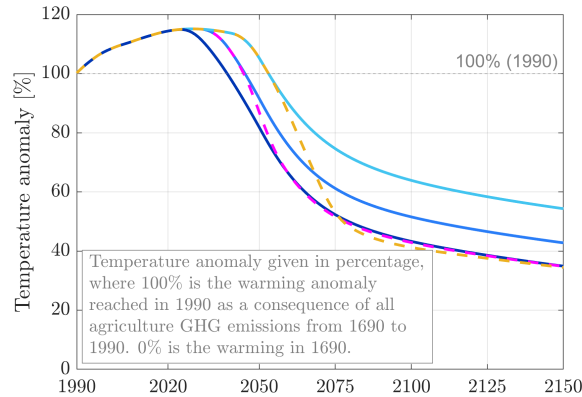
Furthermore, delaying CDR compensation also causes a slight postponement in the timing of the peak

temperature anomaly. This is observable when comparing the light blue curve (CDR starting in 2040) to the dark blue curve (CDR starting in 2020).

In Figure 15, we explore cases where negative emissions are delayed by 10 years (dashed pink line) and by 20 years (dashed yellow line), with same cumulative CDR deployment being achieved later. Figure 15b makes it clear that deploying the full extent of cumulative CDR, even if done at a later time, allows the final asymptotic temperature anomaly to decrease, approaching the dark blue curve representing prompt CDR deployment. However, the timing of peak warming remains slightly postponed, akin to what was observed in Figure 14.



(a) Delaying of CDR deployment, while regaining the total cumulative deployment of carbon dioxide removal



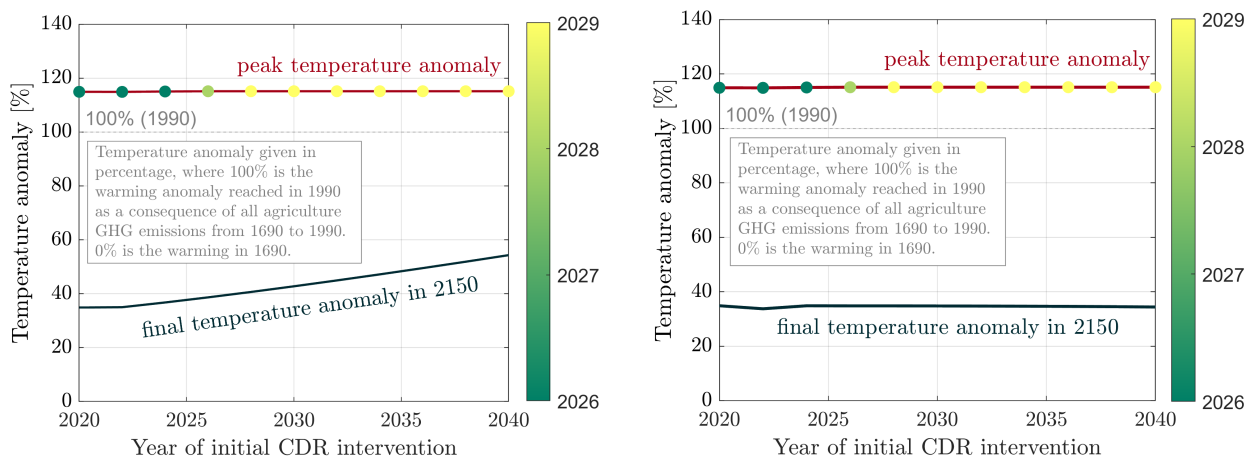
(b) Effect on the temperature anomaly

Figure 15. Delaying compensation by 10 years (i.e. until 2030, blue curve) and 20 years (i.e. until 2040, light blue curve), followed by CDR intervention with the same deployment rate as the case of prompt CDR (i.e. from 2020, dark blue curve) and regaining the total cumulative deployment of carbon dioxide removal. The effect that delaying CDR intervention, while regaining cumulative extent, has on the temperature anomaly is showed in subfigure (b).

The analysis of temperature anomalies was also conducted by continuously varying the onset time of

carbon dioxide removal (CDR) intervention in two-year increments from 2020 to 2040. The results are presented in Figure 16, clearly illustrating that regaining cumulative CDR deployment effectively limits the final level of warming by 2150. In cases of delayed CDR intervention, such as after 2035, the final asymptotic temperature begins to slightly decrease as cumulative equivalent CDR amounts are regained to offset emissions of short-lived climate forcers that have decayed in the meantime.

Additionally, it is worth noting that delaying CDR intervention slightly postpones the timing of peak warming by three years, shifting it from 2026 to 2029. However, the time of peak temperature anomaly is not pushed beyond 2029. This is because 2029 already marks the time of peak warming in the ZeroBasis scenario without CDR deployment (bottom-up curve), as clearly depicted in Figure 12. In cases where the temperature projection without CDR would continue to rise, as seen in the WWB projection (Figure 7), the time of peak warming would be further postponed with continuously delayed CDR intervention. This scenario is analyzed in Figure 17, Figure 18, and Figure 19.



(a) Delaying of CDR deployment without regaining the total cumulative deployment of carbon dioxide removal (b) Delaying of CDR deployment, regaining the total cumulative deployment of carbon dioxide removal

Figure 16. Continuous analysis of the impact on the temperature anomaly when CDR deployment is delayed in time, without (Figure 16a) or with (Figure 16b) regain of cumulative CDR extent.

When the bottom-up emissions profile consists of continuous, constant emissions of methane (CH₄) and nitrous oxide (N₂O), as is the case in the business-as-usual WWB projection, the corresponding temperature anomaly continues to rise. This rise is due to the ongoing increase in emissions that occurred from 1690 to 2020. This behavior is attributed to the longer timescale on which temperature stabilizes, and it can be clearly observed in Figure 7. In such cases, a specific peak warming point is not defined, and the temperature anomaly will simply continue to rise, eventually reaching the expected steady state asymptotically from below.

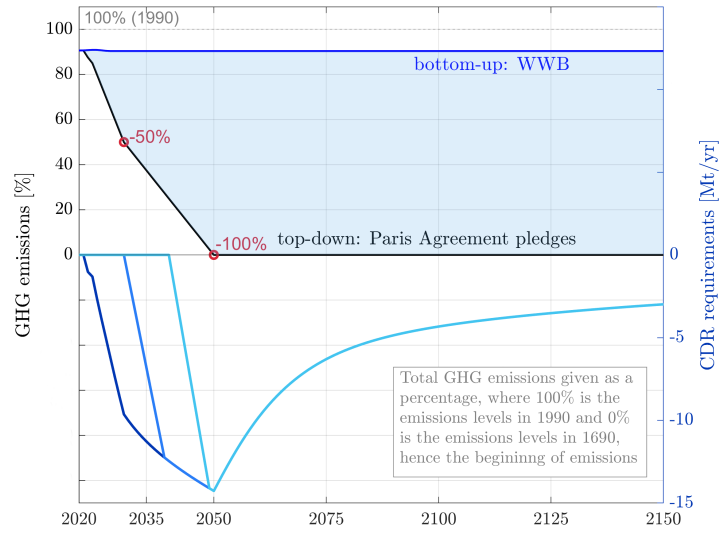
In contrast, a ZeroBasis emissions pathway defines a local peak temperature because of the decrease in methane emissions from 2020 to 2060. After reaching this local minimum, the temperature anomaly of the ZeroBasis scenario starts to increase again, as explained in Section Section 6.2 and demonstrated in Figure 7.

In the context of a business-as-usual emissions scenario, like WWB, where the peak of the temperature anomaly is not well-defined, delaying the deployment of carbon dioxide removal (CDR) has a significant impact on both the timing and magnitude of peak warming. As clearly illustrated in Figure 17 and Figure 18, postponing CDR intervention leads to a later occurrence of peak warming and an increase in the level of peak temperature.

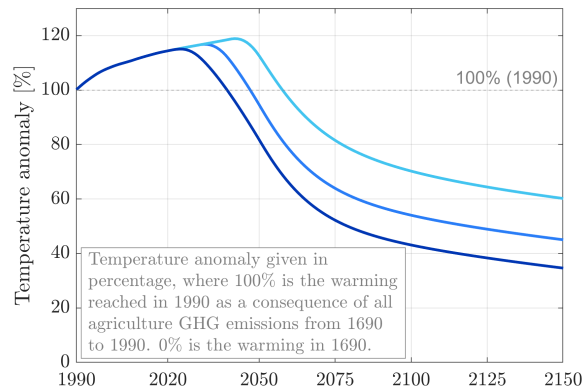
It is important to emphasize that, from a climate perspective, not only the final asymptotic temperature anomaly matters, but also the timing and magnitude of peak warming. Minimizing peak warming is crucial to prevent a momentary overshoot of maximum temperature targets, such as the 1.5°C target outlined in the Paris Agreement. Even a brief exceeding of such a temperature threshold, potentially caused by higher peak warming, can trigger irreversible planetary system feedbacks and exacerbate anthropogenic climate interference²²²³.

Figure 19, in line with Figure 17 and Figure 18, demonstrates that delaying CDR deployment for 20 years (from 2020 to 2040) results in a 4% increase in peak warming compared to 1990 levels, while also delaying it by 18 years (from 2026 to 2044). Regaining cumulative CDR deployment at a later point can constrain the final level of warming in 2150, similar to the ZeroBasis scenario shown in Figure 19.

For cases of prolonged delay in CDR intervention, such as after 2035, the final asymptotic temperature begins to slightly decrease as cumulative equivalent CDR amounts are regained for emissions of short-lived climate forcers that have decayed over time.

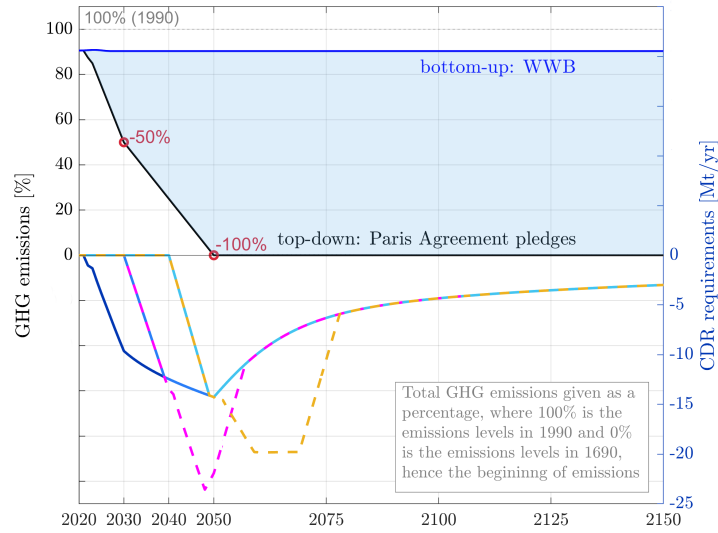


(a) Delaying of CDR deployment

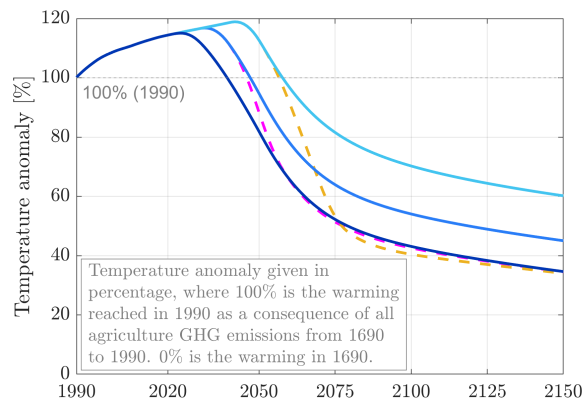


(b) Effect on the temperature anomaly

Figure 17. Delaying compensation by 10 years (i.e. until 2030, blue curve) and 20 years (i.e. until 2040, light blue curve), followed by CDR intervention with the same deployment rate as the case of prompt CDR (i.e. from 2020, dark blue curve). The effect that delaying CDR intervention has on the temperature anomaly is showed in subfigure (b).

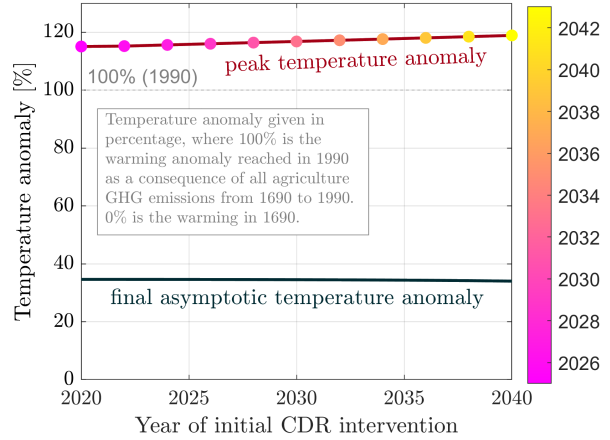
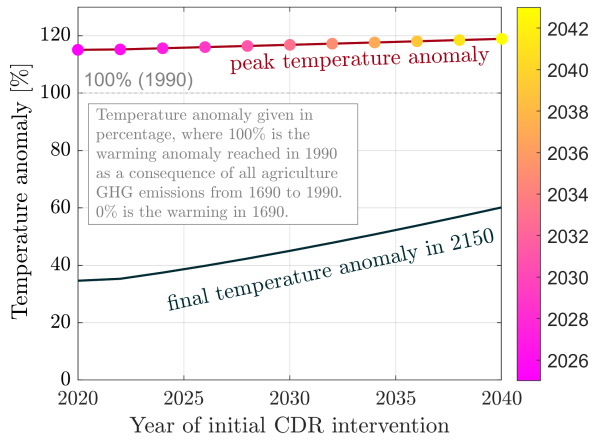


(a) Delaying of CDR deployment, while regaining the total cumulative deployment of carbon dioxide removal



(b) Effect on the temperature anomaly

Figure 18. Delaying compensation by 10 years (i.e. until 2030, blue curve) and 20 years (i.e. until 2040, light blue curve), followed by CDR intervention with the same deployment rate as the case of prompt CDR (i.e. from 2020, dark blue curve) and regaining the total cumulative deployment of carbon dioxide removal. The effect that delaying CDR intervention, while regaining cumulative extent, has on the temperature anomaly is showed in subfigure (b).



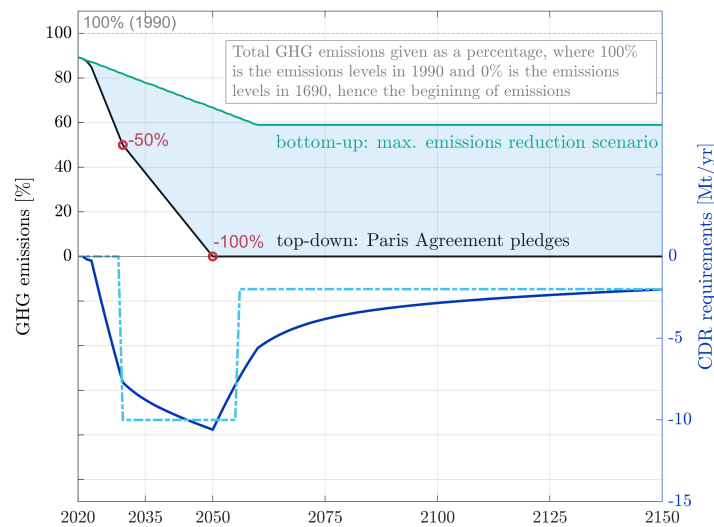
(a) Delaying of CDR deployment without regaining the total cumulative deployment of carbon dioxide removal (b) Delaying of CDR deployment, regaining the total cumulative deployment of carbon dioxide removal

Figure 19. Continuous analysis of the impact on the temperature anomaly when CDR deployment is delayed in time, without (Figure 19a) or with (Figure 19b) regain of cumulative CDR extent.

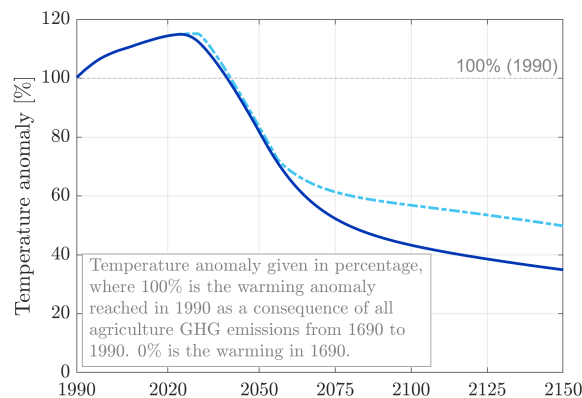
9.2 Piece-wise constant simplification of the CDR profile: the effect on the temperature anomaly

Similarly, the tools developed in this study can be employed to assess the climate impact of a target, simplified CDR deployment profile, in absolute terms or in comparison to the reference, LWE-calculated CDR curve. An example, is showed in Figure 20a where piece-wise constant simplification of the LWE-calculated CDR profile is assumed and showed in a light-blue dash-dotted line. The temperature anomalies of the correctly calculated LWE curve and the simplified CDR profiles are reported in Figure 20b.

Simplification was assumed here to allow for constant CDR deployment at 10 Mt/yr from 2030 to 2055, followed by constant CDR deployment at 2 Mt/yr. The resulting temperature anomaly from this simplified profile results in a good agreement with the reference dark blue-solid curve until 2055, and presents then a 15% final steady state temperature anomaly as less cumulative CDR is provided in the simplified case.



(a) Piece-wise simplification of the LWE-CDR deployment



(b) Effect on the temperature anomaly

Figure 20. In light blue, dash-dotted lines is the piece-wise simplification of the CDR profile and its effect on the temperature anomaly, compared to the reference LWE-calculated, exact CDR deployment curve (in dark blue, solid lines).

10 The impact of different equivalence metrics on CDR requirements: simulations for the Swiss aviation sector

Analogous to the analysis of the Swiss agriculture sector, we now turn our attention to the Swiss aviation sector.

Figure 47 (Milestone 2) presents the breakdown of greenhouse gas (GHG) emissions in Swiss aviation, with a primary contribution from CO₂, (NO_x), cirrus clouds, and some climate impact attributed to water vapor (H₂O). Other GHG emissions, such as BC and SO_x, have negligible climate impact and will not be considered further.

The green bottom-up curve (Figure 21) represents the projected reduction of aviation NO_x emissions, H₂O emissions and CO₂ emissions (which are expected to reach zero by 2050 due to the full adoption of Sustainable Aviation Fuels (SAFs) as discussed in Section 7.1) following the ZeroBasis EP2050+ scenario. Cirrus cloud formation is not included in the bottom-up curve. Instead, the top-down curve is again defined as a reduction, where emissions need to be decreased by 50% in 2030 compared to 1990 levels and reach a 100% reduction by 2050, in alignment with the Paris Agreement.

Similar to the agriculture sector, aviation is categorized as a "hard-to-transition" sector, necessitating the deployment of carbon dioxide removal (CDR) to offset all flight and non-flight emissions, including CO₂ and non-CO₂ emissions. To quantify the required CDR deployment needed to compensate for the residual NO_x, H₂O and CO₂ emissions (complying with the top-down black curve), we consider four equivalence approaches as discussed in previous sections: GWP₁₀₀, GWP₂₀, GWP*, and LWE. The corresponding CO₂ removal requirements, calculated using these approaches, are presented in Figure 21. These values are represented by different line styles: dashed-dotted for GWP₁₀₀, dashed for GWP₂₀, dotted for GWP*, and solid for LWE.

Additionally, the pink-solid line in Figure 21 represents the calculated CDR deployment needed to compensate for both the difference between the depicted bottom-up and top-down curves (which consider NO_x, H₂O, and CO₂ aviation emissions) and the climate impact of cirrus clouds. The climate impact of cirrus clouds is assessed by parameterizing their radiative forcing in terms of kilometers of air traffic volume, as discussed in Section 3.2.2. To calculate the CDR required to compensate for the climate impact of cirrus formation, we define a top-down curve of target reduction. This curve stipulates that kilometers of flight must be reduced by 50% in 2030 compared to 1990 levels and achieve a 100% reduction by 2050. It's important to note that this reduction in air traffic volume is merely a theoretical construct used to calculate the CDR necessary to offset all the climate impact generated by cirrus clouds.

In the following analysis, we will examine the differences in CDR requirements resulting from these different equivalence approaches, providing insights into their implications for CDR strategies in the context of aviation emissions reduction.

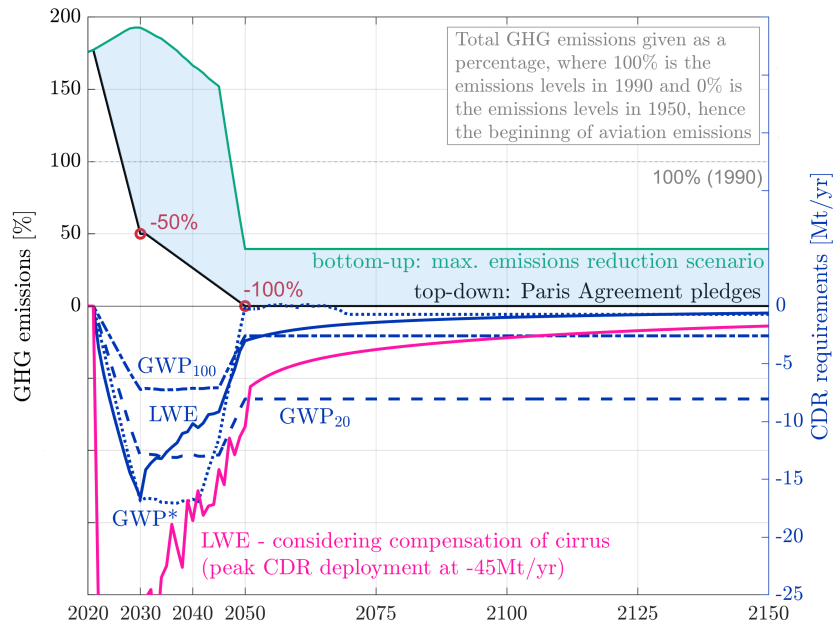


Figure 21. Determination of the CDR compensation strategy depending on the CO₂ equivalence metric employed in the calculations. Total GHG aviation emissions (i.e. CO₂, NO_x and H₂O emissions) to be compensated, hence the difference between the maximum reduction scenario (bottom-up curve) and climate targets in line with the reference objective scenario (top-down curve), are illustrated on the left vertical axis, as a percentage of the total emissions levels in 1990. The right vertical axis shows the yearly carbon dioxide removal, in negative values, required to compensate the blue area of residual emissions, as calculate by the different equivalence metrics to assess CO₂-equivalents for NO_x and H₂O. Required CDR compensation when considering also the climate impact of cirrus clouds is depicted in pink, as calculated by means of the LWE model. Only the deployment of CDR, as calculated by means of the LWE model, would ensure compensation of the climate impact (radiative forcing) of the light blue area, hence of the remaining agricultural emissions that need to be actively compensated in order to comply with the top-down emissions reduction targets. All other approaches (*GWP*₂₀, *GWP*₁₀₀ and *GWP*^{*}) under- and overestimate the required CO₂ removal at some point in time.

The analysis of the CDR requirements, as calculated using different equivalence approaches, reveals important insights into the strategies for addressing aviation emissions in the context of carbon dioxide removal. Here are the key observations:

- **LWE model:** When CDR is deployed according to the curve calculated with the LWE metric, it ensures compensation of the radiative forcing and, consequently, the climate impact generated by the light blue area. The LWE model provides an accurate representation of the temporal dynamics of emissions and their impact, making it a suitable choice for CDR planning.
- **GWP₁₀₀ metric:** The GWP₁₀₀ metric only matches the LWE-based CO₂ equivalence calculation at specific points in time when its curve intersects with the LWE profile. Before this intersection, it underestimates the CDR requirement compared to the LWE model. Afterward, it overestimates the CDR requirement. The GWP₁₀₀ metric does not provide an accurate representation of the evolving emissions and radiative forcing, making it less suitable for long-term CDR planning.
- **GWP₂₀ Metric:** The GWP₂₀ metric exhibits a similar behavior to GWP₁₀₀ but with a shorter time frame. It matches the correct CO₂ equivalence calculation at an earlier point in time when it intersects

with the LWE profile. However, it still underestimates the CDR requirement before this intersection and overestimates it afterward. Like GWP_{100} , GWP_{20} is not suitable for long-term CDR planning.

- **GWP* model:** The GWP* model approaches the LWE-CDR deployment but overreacts to discontinuous variations in the amount of residual emissions to compensate. GWP* may be a reasonable choice for CDR planning (upon correct calibration of this empirical metric, Appendix B.4) but may fall short in cases with significant emission fluctuations.

In summary, as previously also concluded for the agriculture sector, the choice of equivalence approach significantly impacts the calculation of CDR requirements to offset aviation emissions. The LWE model provides a useful reference representation of emissions and radiative forcing over time, making it a possible choice for CDR planning. GWP* generally provides an acceptable estimate, when correctly calibrated.

When taking into account the climate impact of cirrus clouds, represented by the pink curve in the graph, the LWE-CDR strategy follows a similar trend as the corresponding blue curve (which considers only NO_x , H_2O , and CO_2 compensation). However, as anticipated, the CDR deployment increases significantly, peaking at 45 Mt per year of CDR. This increase reflects the additional CDR required to offset the climate impact generated by cirrus cloud formation (which was defined as a main warmin inducer for the aviation sector in Milestone 2, Figure 47), making it a substantial component of the overall CDR strategy for the aviation sector.

As previously discussed for agriculture, and highlighted in Figure 21, not only does the extent of CDR deployment in a certain year change for different CDR strategies, but also the rate of CDR deployment strongly differs among equivalence metrics, with LWE and GWP* projecting a sharp increase early on (e.g. already from 2020 to 2030) compared to the other two metrics.

By means of the chain of causality and climate model introduced in Part I, the temperature anomaly curves corresponding to the different CDR strategies analyzed in Figure 21, are calculated and showed in Figure 22.

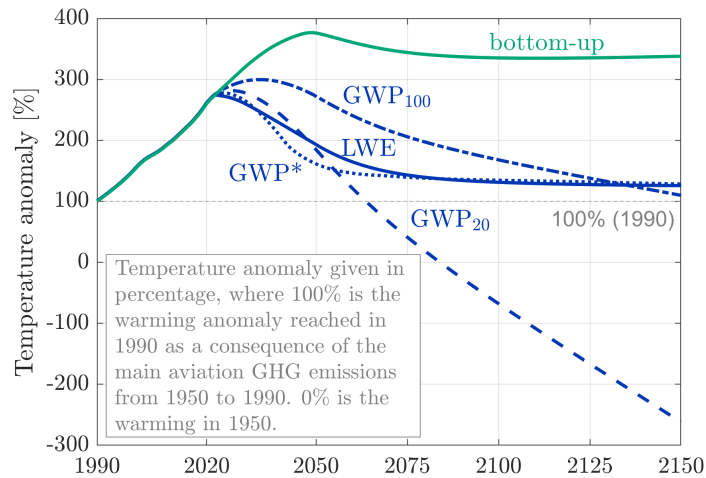


Figure 22. Temperature anomaly as a consequence of CO₂, NO_x and H₂O aviation emissions from 1950 onward, expressed in percentage of the warming in 1990 (where 100% corresponds to the warming in 1990 and 0% is the temperature anomaly in 1950, hence the beginning of significant aviation anthropogenic activity). Temperature anomaly curves are shown for five different scenarios. The green curve shows the warming resulting from the EP2050+ ZeroBasis emissions scenario, where no CDR compensation is undergone. The other four curves exhibit the development of the temperature anomaly, related to Swiss aviation emissions from 1950 onward, when the GWP₁₀₀- (dashed-dotted line), GWP₂₀- (dashed line), GWP*- (dotted line) and LWE-CDR strategies (solid line) are implemented from 2020 onward. The metric-specific CDR strategies are shown in Figure 21.

Firstly, it is possible to observe that only following the ZeroBasis projected emissions reduction and deploying no CDR strategy to compensate for the residual emissions of CO₂, NO_x and H₂O (green, bottom-up curve) increases warming to almost four times the levels in 1990. The emissions reduction projected in the ZeroBasis scenario results only in a momentary decrease in the temperature anomaly, which however slightly increases in the long run to reach the steady state, as previously discussed in Section 7.2. Instead, the climate impact of a Swiss CDR strategy, to align the aviation sector to the top-down target showed in Figure 21, highly differs depending on the equivalence metric implemented. Nevertheless, it is evident that all CDR strategies, regardless of the approach used to calculate the rate of CDR deployment, enable the anticipation and reduction of the peak temperature anomaly compared to the scenario without CDR.

Figure 22 clearly shows that an LWE-CDR strategy allows to perfectly stabilize the temperature anomaly to a constant value, ensuring exact compensation of the climate impact generated by the residual emissions (light blue area pictured in Figure 21). However, it is also important to note that a net-zero emissions objective for the aviation sector, as depicted by the top-down curve of Figure 21, stabilizes the temperature anomaly to levels greater than those induced by the aviation sector in 1990.

Instead, as mentioned before, GWP₁₀₀ strongly underestimates the required CO₂ negative emissions for a prolonged time, effectively increasing the temperature anomaly by approximately over 50% on average and also increasing peak warming and postponing its time, compared to LWE. The temperature anomaly of the LWE-CDR strategy and that of the GWP₁₀₀-CDR strategy only cross after 2125. Afterwards, the temperature associated to the GWP₁₀₀-CDR strategy continues to decrease linearly due to over-deployment of CO₂ removal. This is also clearly seen in the GWP₂₀-CDR strategy where the overcompensation with negative emissions starts sooner, as previously indicated in Figure 21. Here the temperature anomaly decreases rapidly, and somewhat uncontrollably, reaching the temperature values of 1950 (0%) around 2080 and plummeting below this level afterwards.

Overall, one might conclude that employing GWP₂₀ and GWP₁₀₀ metrics would undermine the effectiveness and stability of any CDR strategy, and hence climate policy.

Lastly, with a GWP*-CDR strategy the temperature anomaly can also be accurately stabilized to the asymptotic final value associated to the LWE-CDR strategy. It is important to highlight, however, that this is only the case for stable and continuous negative emissions requirements, as is the light blue area between 2050 and 2150 (Figure 21).

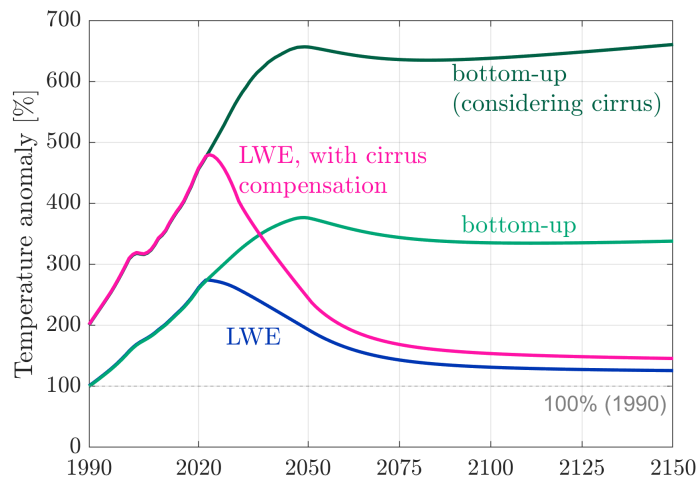


Figure 23. Here the same bottom-up (in light green) and LWE-CDR (in blue) temperature curves are reported as in Figure 22. In addition the temperature anomaly curves considering the climate impact of cirrus clouds without (in dark green, this curve corresponds to the bottom-up curve previously shown in ??) and with CDR compensation (in pink) are depicted. All temperature anomalies are given in percentages, where 100% is the warming reached in 1990 for the light, green bottom up curve, hence the curve only considering CO₂, NO_x and H₂O impacts.

In Figure 23 we also analyzed the projected temperature anomaly when considering the climate impact from cirrus clouds formation, as a result of aviation practices. In this figure, you can see several temperature anomaly curves for the Swiss aviation sector. The light green curve represents the bottom-up projection, considering only the climate impact of CO₂, NO_x, and H₂O emissions. The blue curve represents the LWE-CDR strategy, which includes carbon dioxide removal to compensate for these emissions. These curves correspond to the ones reported in Figure 22.

Additionally, two more temperature anomaly curves are depicted: the dark green curve represents the temperature anomaly when considering the climate impact of cirrus clouds (together with that of CO₂, NO_x and H₂O) without any carbon dioxide removal (CDR) compensation. The pink curve represents the temperature anomaly when a LWE-CDR is used to compensate for the climate impact of these aviation-induced pollutants.

All temperature anomalies are presented as percentages relative to the warming reached in 1990 for the light green bottom-up curve, which accounts for CO₂, NO_x, and H₂O impacts. This shows that the warming caused by cirrus clouds is equal, in absolute values, to the warming caused by CO₂, NO_x, and H₂O; considering cirrus clouds approximately doubles the overall climate impact of aviation, which is in line with finding from Milestone 2 (Figure 47).

Looking at the cumulative carbon removal requirements, as shown in Figure 24, paints a rather challenging

picture indicating an extremely large necessity of CDR deployment just to allow the Swiss aviation sector to comply with reduction targets in line with the reference objective scenario and reach net-zero emissions in 2050 (top-down curve in Figure 21). Until 2050, just under 200 Mt of CO₂ removal would have been cumulatively required by a GWP₁₀₀-CDR strategy, while a LWE-, a GWP*- and a GWP₂₀-CDR strategy would overlap at over 300 Mt cumulatively. When considering compensation for the climate impacts of cirrus clouds, the cumulative CDR requirements increase significantly, reaching over 700 Mt in 2050.

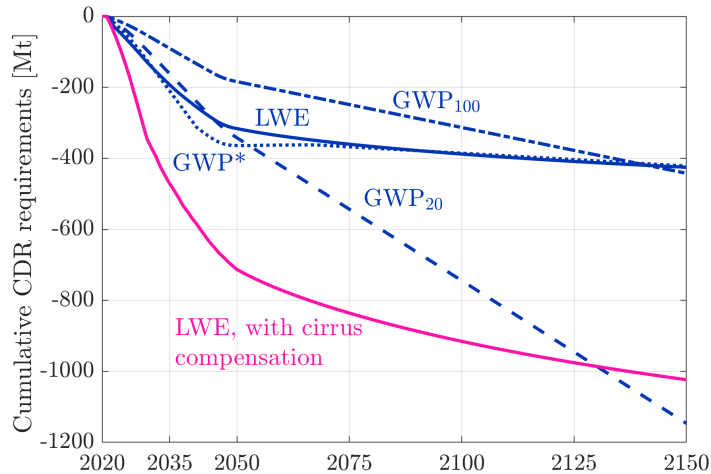


Figure 24. Cumulative CDR requirement, from 2020 to 2150, for the CDR strategies as following the four different equivalence metrics.

As previously mentioned and highlighted in Figure 21, the extent of carbon dioxide removal (CDR) deployment not only varies depending on the equivalence approach employed but also exhibits significant differences in the rate of CDR deployment until 2050. Specifically, the LWE and GWP* models project a more rapid deployment of carbon removal early on (e.g., from 2020 to 2030) compared to the commonly employed GWP₁₀₀ metric. This raises a critical question regarding the potential consequences for the temperature anomaly in the event that CDR cannot be deployed as rapidly as required by the CDR strategies outlined in Figure 21. This question is further explored in the following section.

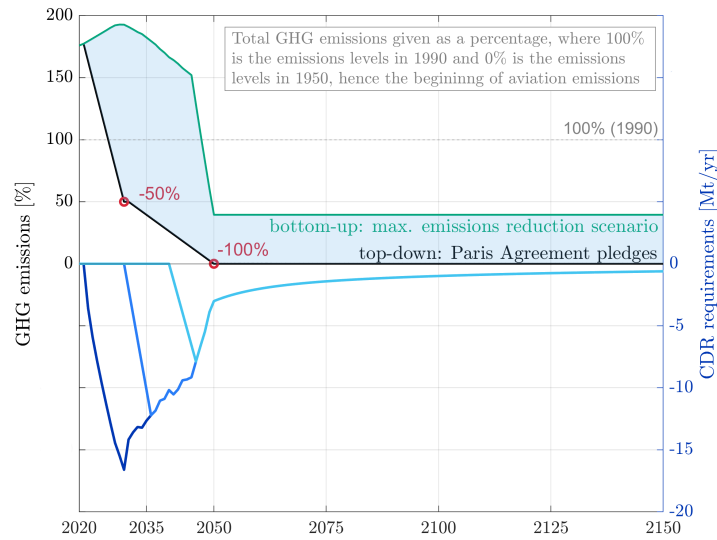
10.1 Delaying CDR intervention: the effect on the temperature anomaly

The same cases of delayed intervention are analyzed for the aviation sector as performed in Section 9.1:

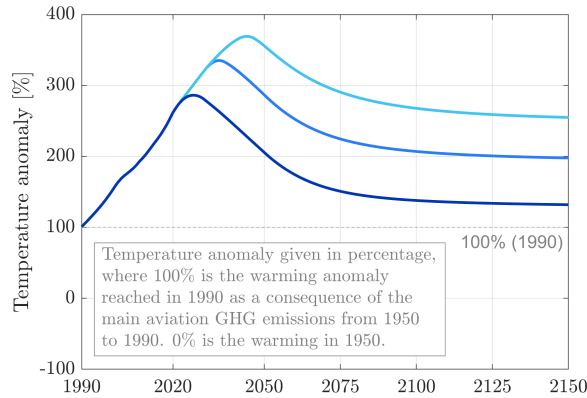
1. intervention is delayed until 2030, then regaining CDR deployment rate
2. intervention is delayed until 2040, then regaining CDR deployment rate
3. intervention is delayed until 2030, then regaining CDR deployment rate and cumulative CDR
4. intervention is delayed until 2040, then regaining CDR deployment rate and cumulative CDR

Analysis of delayed CDR deployment is performed only with the LWE model, for the sake of simplicity.

The first two cases of delayed compensation, and their respective temperature anomaly profiles, are showed in Figure 25 (in blue and light blue, respectively) together with the curve of prompt CDR deployment starting from 2020 (in dark blue).



(a) Delaying of CDR deployment



(b) Effect on the temperature anomaly

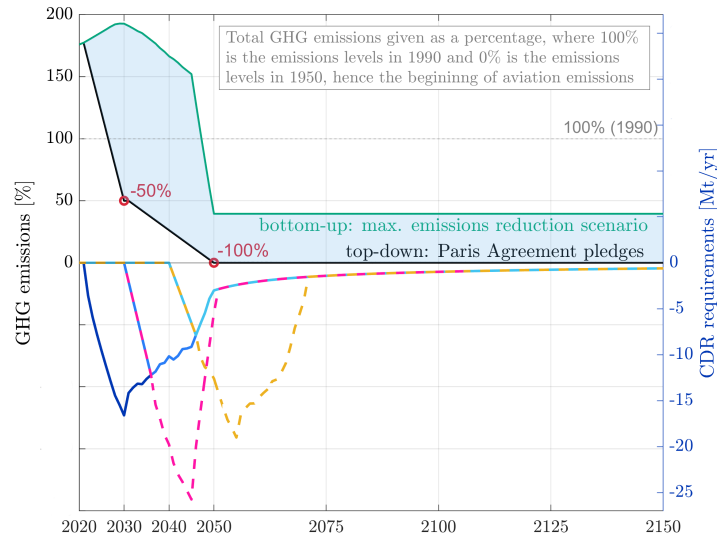
Figure 25. Delaying compensation by 10 years (i.e. until 2030, blue curve) and 20 years (i.e. until 2040, light blue curve), followed by CDR intervention with the same deployment rate as the case of prompt CDR (i.e. from 2020, dark blue curve). The effect that delaying CDR intervention has on the temperature anomaly is showed in subfigure (b).

Referring to Figure 25, it becomes evident that delaying carbon dioxide removal (CDR) compensation by 10 years (blue curve) and by 20 years (light blue curve) has a significant impact on the temperature anomaly. This delay results in an increase in the final asymptotic steady-state temperature. The reason for this is that the three CDR compensation strategies proposed in Figure 25a lead to different radiative forcing profiles, thereby implying distinct temperature anomalies and steady states.

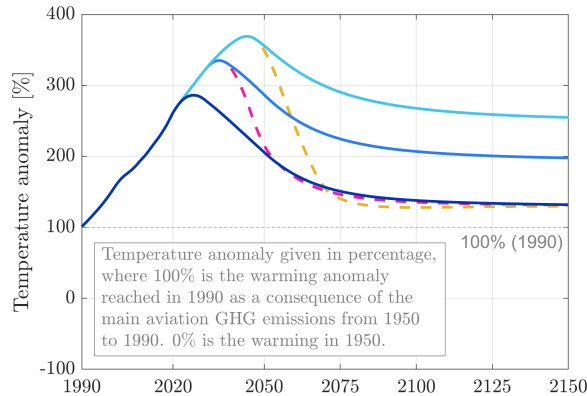
Furthermore, delaying CDR compensation also causes an increase in peak warming and a postponement in the timing of this peak temperature anomaly. This is observable when comparing the light blue curve (CDR starting in 2040) to the dark blue curve (CDR starting in 2020).

In Figure 26, we explore cases where negative emissions are delayed by 10 years (dashed pink line) and by 20 years (dashed yellow line), with same cumulative CDR deployment being achieved later. Figure 26b makes it clear that deploying the full extent of cumulative CDR, even if done at a later time, allows the final asymptotic

temperature anomaly to decrease, approaching the dark blue curve representing prompt CDR deployment. However, the timing of peak warming remains higher and postponed, akin to what was observed in Figure 25 and the results for the agriculture sector (Section 9.1).



(a) Delaying of CDR deployment, while regaining the total cumulative deployment of carbon dioxide removal

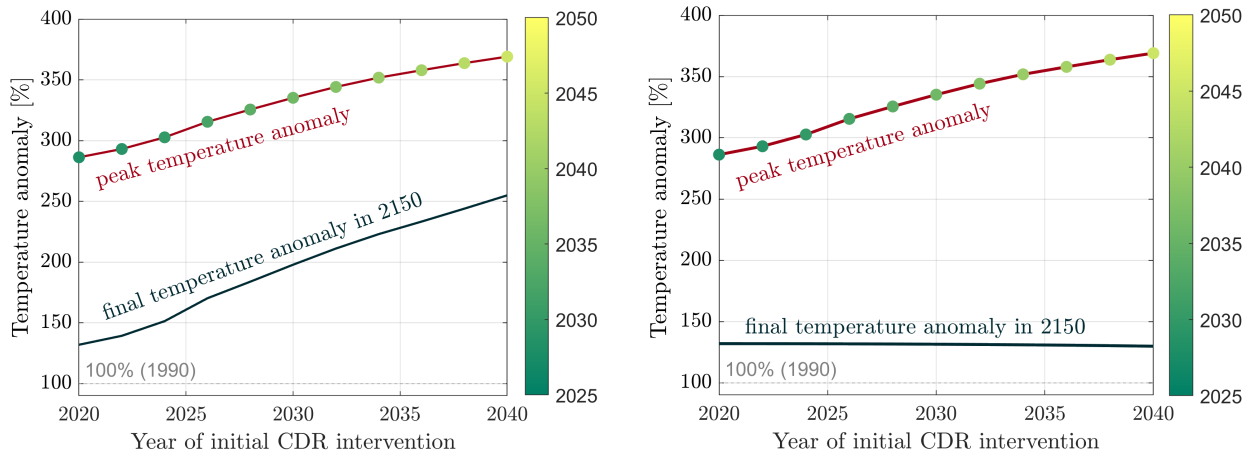


(b) Effect on the temperature anomaly

Figure 26. Delaying compensation by 10 years (i.e. until 2030, blue curve) and 20 years (i.e. until 2040, light blue curve), followed by CDR intervention with the same deployment rate as the case of prompt CDR (i.e. from 2020, dark blue curve) and regaining the total cumulative deployment of carbon dioxide removal. The effect that delaying CDR intervention, while regaining cumulative extent, has on the temperature anomaly is showed in subfigure (b).

The analysis of temperature anomalies was also conducted by continuously varying the onset time of carbon dioxide removal (CDR) intervention in two-year increments from 2020 to 2040. The results are presented in Figure 27, clearly illustrating that regaining cumulative CDR deployment effectively limits the final level of warming by 2150. In cases of delayed CDR intervention, such as after 2035, the final asymptotic temperature begins to slightly decrease as cumulative equivalent CDR amounts are regained to offset emissions of short-lived climate forcers that have decayed in the meantime.

Additionally, it is worth noting again that delaying CDR intervention postpones the time of peak warming from 2025 to 2045; and increases the level of the peak almost twice. Figure 19.



(a) Delaying of CDR deployment without regaining the total cumulative deployment of carbon dioxide removal (b) Delaying of CDR deployment, regaining the total cumulative deployment of carbon dioxide removal

Figure 27. Continuous analysis of the impact on the temperature anomaly when CDR deployment is delayed in time, without (Figure 27a) or with (Figure 27b) regain of cumulative CDR extent.

Part IV

Milestone 4 - Implications for the Swiss climate policy

11 Net-zero in the frame of the KIG law: the two interpretations of "Wirkung"

In Art. 3.3 the Klima- und Innovationsgesetz (KIG) states that total Swiss emissions need to be reduced, compared to the emissions levels of 1990, as to fulfill the following interim targets:

- between 2031 and 2040: -64% on average, at least;
- in 2040: -75%, at least;
- between 2041 and 2050: -89% on average, at least.

Therefore, each Swiss economic sector is to follow its maximum emissions reduction pathway from now until 2050, for example either by decarbonizing via electrification or by implementing point-source CO₂ capture with permanent storage (CCS). The difference between any remaining Swiss emissions and the interim targets set by Art 3.3 must be compensated through the purchase of international or national certificates, or possibly also by means of carbon dioxide removal from a certain time on.

After 2050 in fact, international avoidance certificates are expected to be no longer available, as all countries should have achieved net-zero emissions by then. As stipulated in Article 3.1b, any remaining residual reference objective scenario emissions must be addressed using negative emissions technologies to compensate for the climate "Wirkung," which translates into the effect or impact, of these residual greenhouse gas emissions, including aviation s indicated in Art 3.6.

This report identifies two possible interpretations of the term "Wirkung" in this context, namely:

- Target 1: Achieving net-zero residual emissions by 2050;
- Target 2: Achieving zero residual radiative forcing by 2050.

In this chapter, we analyze the climate impact and carbon dioxide removal (CDR) requirements if these targets were to be achieved by initiating CDR only from 2050. The reason for this approach is that Article 3.1b mandates the commencement of CDR from 2050 onward if necessary but does not require its deployment before then. Since in the long-term climate strategy, the deployment of CDR is also foreseen before 2050, we conduct a sensitivity analysis starting the year of CDR deployment.

However, in Milestone 3, we also analyzed the scenario where CDR deployment began in this decade (from 2020) to achieve a net-zero emissions objective by 2050 (Target 1). This can be compared to the results presented in Section 12.1, where the same target is achieved but CDR is initiated only from 2050. Similarly, in Section 12.2 of this milestone, we will demonstrate the impact of initiating CDR in this decade compared to a scenario where deployment begins only from 2050 onward when the objective is to reach net-zero residual radiative forcing (Target 2).

12 Results for the Swiss agriculture sector

12.1 Target 1: Net-zero residual emissions in 2050

Agriculture GHG emissions, which include methane, nitrous oxide, and carbon dioxide, and related climate impacts (over the time horizon from 1690 to 2300, and shown here only from 1990) are illustrated in Figure 28 for two of the projected future scenarios that we have already discussed: the business-as-usual WWB scenario

(in blue) and the EP2050+ ZeroBasis scenario (in green). The negative emissions required to achieve Target 1, which is net-zero emissions in 2050 with CDR starting from that year (this is the emissions profile shown as a black solid line in the first panel of Figure 28), are calculated using the LWE approach. This is applied to all the emissions of the two scenarios, because the goal is to reach zero emissions in 2050. The four panels show, from left to right: (i) the emissions in percentage (left vertical axis), where 100% corresponds to the level of emissions in 1990, while 0% represents their level at the start of detectable anthropogenic agriculture emissions, i.e., the year 1690; (ii) in the same first panel the CDR requirements in Mt/yr (right vertical axis), where rates of CDR are negative numbers, in contrast to emissions that are positive; (iii) the cumulative CDR requirements needed to achieve the net-zero emissions target when residual emissions follow either WWB or ZeroBasis (second panel); (iv) the associated radiative forcing for the WWB and ZeroBasis scenarios with and without CDR (third panel), where 100% is the corresponding level in 1990, and 0% that in 1690; (iv) the associated temperature anomaly for the WWB and ZeroBasis scenarios with and without CDR (fourth panel), where 100% is the corresponding level in 1990, and 0% that in 1690.

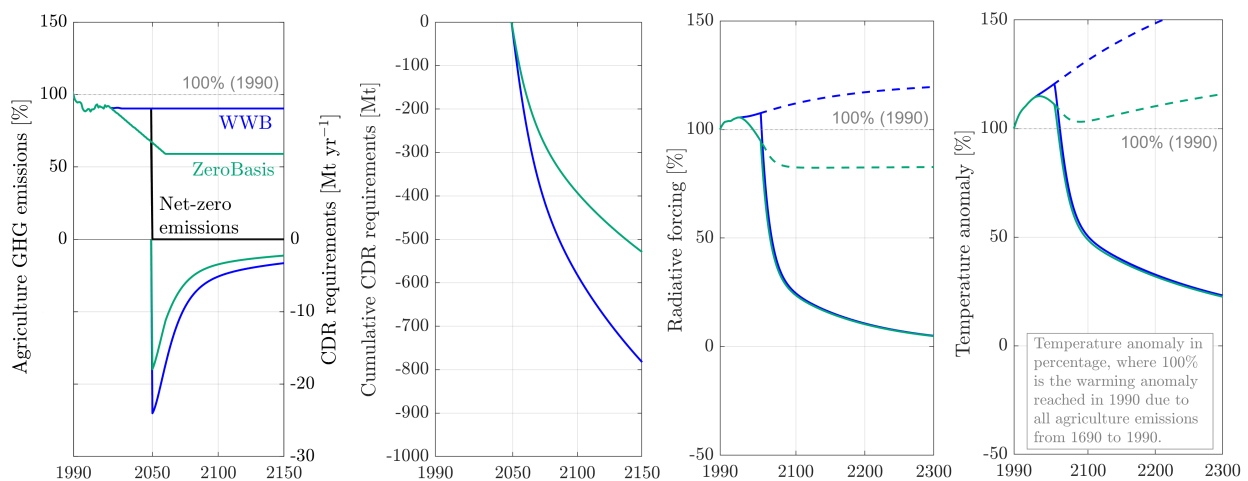


Figure 28. The first plot shows the CDR requirements to achieve net-zero emissions in 2050, starting negative emissions deployment from that same year. The analysis is performed for the business-as-usual WWB scenario (in blue) and for the ZeroBasis projection (in green). CDR requirements are calculated with the LWE equivalence metric. Achieving net-zero emissions, while only deploying CDR from that same target year, results in a peak of 25 and 18 Mt/yr for the WWB and ZeroBasis cases, respectively. This can be partially lowered through the earlier deployment of CDR, which is shown in Figure 11. The second plot exhibits cumulative CDR requirements for the two scenarios; the third and fourth plot show radiative forcing and temperature anomaly (normalized by the respective values in 1990) with CDR implementation (in solid lines) and without (in dashed lines) for the WWB and ZeroBasis scenarios. Target 1 of net-zero emissions allows for a sharp decrease in the climate impact, with warming approaching 0% (i.e., pre-industrial temperature level), as the remaining emissions of CH₄ and N₂O decay.

A few remarks about the results in Figure 28 are worth making:

- CDR requirements are much higher and must be fulfilled much faster if emissions from agriculture continue as in the WWB scenario than if they decrease following the ZeroBasis pathway.
- Implementing CDR measures allows reducing radiative forcing and temperature anomaly in both scenarios at the same level, thus avoiding the major increase of warming above 1990 levels in case CDR measures are not implemented.
- Although very similar, for instance in their long term behavior, the evolution of the temperature anomaly

differs in one critical feature. The peak temperature anomaly is more than 120% of that in 1990 in the WWB case, whereas it is 115% of that value in the ZeroBasis case. From a climate perspective this is a significant difference.

- It is worth noting that the peak rate of CDR generation occurs in both scenarios in 2050, when it attains very high values of ca. 25 and ca. 18 Mt CO₂ per year. This is a consequence of the assumption that no CDR measures are implemented before 2050.
- When this value is compared to the estimate made in the EP 2050+, ZeroBasis scenario, about the need for CDR for the whole Switzerland, i.e., ca. 7 Mt CO₂ per year in 2050, one sees clearly that the values obtained in this study are much larger, possibly unrealistically large. The discrepancy stems from the fact that EP 2050+ uses the GWP100 metric that leads to a short term underestimation of the need for CDR, as discussed in previous parts of this report.

There is one way to address this last issue, namely that of anticipating the deployment of CDR to before 2050. This is illustrated in Figure 29 and in Figure 30. In the former figure the same ZeroBasis profiles shown in Figure 28 are plotted together with those obtained when enforcing a linear reduction of emissions from the 2020 level to zero in 2050 (dotted lines in the four panels of Figure 29). It is apparent that the maximum rate of CDR deployment is reduced to ca. 10 Mt CO₂, and that the targeted reduction in radiative forcing and in temperature anomaly starts 10 to 20 years earlier.

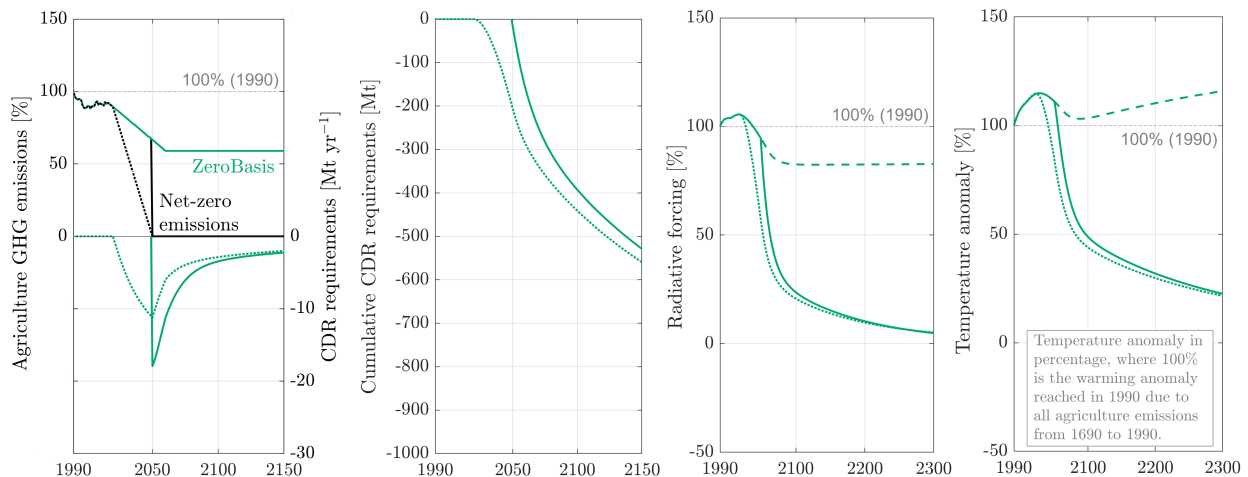


Figure 29. In the first panel, the required profile of CDR deployment is showed for a target 1 of net-zero emissions in 2050 when CDR is started early on (i.e., in 2020, showed in dotted lines) or only from 2050 (showed in solid lines), as two follow the two black target lines of net-zero emissions. Cumulative CDR requirements, the resulting radiative forcing perturbation and the temperature anomaly are showed for the two CDR profiles, starting from 2020 or from 2050, in the second, third and fourth panels, respectively. From this figure it is possible to see that early CDR deployment allows for a sooner decrease in the agriculture-induced climate impact, but more importantly it allows to almost halve peak CDR demand to a maximum of 10 Mt/yr.

In Figure 30 the observation above is further confirmed by the plots of cumulative CDR requirement, peak CDR generation rate and peak temperature anomaly as a function of the year when CDR measures have started to being deployed; these exhibit trends that are fully in line with the discussion above.

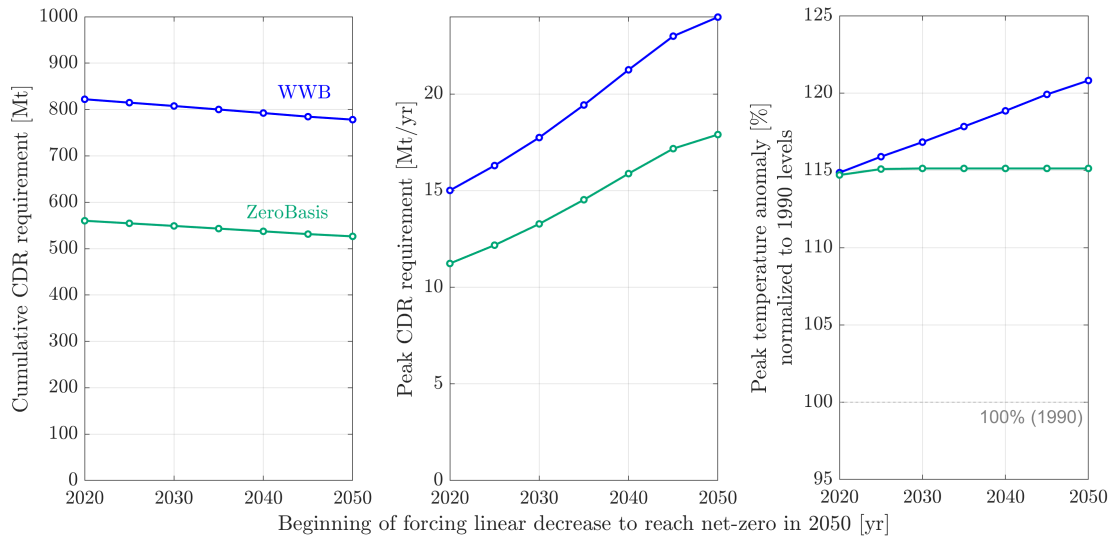


Figure 30. Cumulative CDR requirements (left panel), peak CDR requirements (middle panel) and peak warming (right panel) as a function of the beginning of CDR deployment when the policy objective is to achieve net-zero emissions by 2050. Delaying CDR deployment increases peak negative emissions requirements. Cumulative CDR, on the other hand, is slightly increased when early emissions reduction to net-zero is targeted.

12.2 Target 2: Zero residual forcing in 2050

The same diagrams as for target 1 are shown for target 2 in Figure 31. In this case the goal is to achieve zero radiative forcing from 2050 on, with CDR deployment starting in 2050; this is the radiative forcing profile shown as a red solid line in the third panel from the left in Figure 31. The negative emissions required to achieve Target 2 are calculated also in this case using the LWE approach. It is worth noting that the amount of CDR needed to achieve a target defined in terms of radiative forcing can only be done using the LWE approach; no other metric could be utilized in this case.

Also in this case a few remarks are worth making:

- CDR requirements are much higher and must be fulfilled much faster if emissions from agriculture continue as in the WWB scenario than if they decrease following the ZeroBasis pathway.
- Implementing CDR measures allows for reducing radiative forcing and temperature anomaly in both scenarios at the same level, thus avoiding the major increase of warming above 1990 levels in case CDR measures are not implemented.
- Although very similar, for instance in their long term behavior, the evolution of the temperature anomaly differs in one critical feature, i.e., a higher peak temperature anomaly in the WWB case.
- Also in this case, the rate of CDR generation peaks in both scenarios in 2050, when it attains extremely, unrealistically high values of more than 350 Mt CO₂ per year. This is a consequence of the assumption that no CDR measures are implemented before 2050.
- Although also in this case the peak rate of CDR deployment can be reduced by starting CDR implementation before 2050 (see Figure 32), its value if deployment started in 2020 would still be very high, namely ca. 25 Mt CO₂.

Thus summarizing, when comparing the results obtained for target 1 and for target 2, it appears that targeting net-zero radiative forcing by 2050 does indeed accelerate the reduction in thermal anomaly, but only a little bit (compare the rightmost panels of Figure 28 and of Figure 31). Whereas the increase of the peak rate of CDR deployment, of the order of ten times, is unrealistic; such requirement makes target 2 also unrealistic.

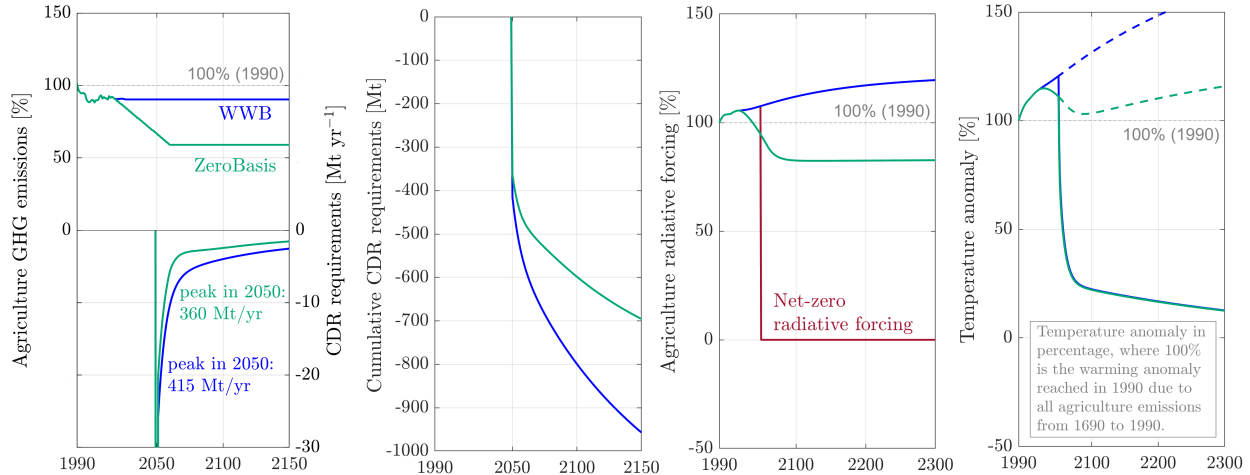


Figure 31. The first plot shows the CDR requirements to achieve zero forcing in 2050, starting negative emissions deployment from that same year. The analysis is performed for the business-as-usual WWB scenario (in blue) and for the ZeroBasis projection (in green). CDR requirements to allow a specific forcing evolution can only be calculated by means of the LWE equivalence metric. Achieving net-zero forcing, while only deploying CDR from that same target year, results in an unfeasible peak CDR demand. This can be lowered by an order of magnitude through the earlier deployment of CDR, which is shown in Figure 32, resulting therefore in a peak CDR requirement more comparable to that of a net-zero emissions objective (Target 1). The second plot exhibits cumulative CDR requirements for the two scenarios, while the third plot shows temperature anomaly (normalized by the respective values in 1990) with CDR implementation (in solid lines) and without (in dashed lines) for the WWB and ZeroBasis scenarios. This last figure shows that achieving net-zero forcing allows for a sharp decrease in the temperature anomaly, and long-term stabilization to 0%, hence the warming at the beginning of Swiss agriculture anthropogenic emissions (i.e., 1690).

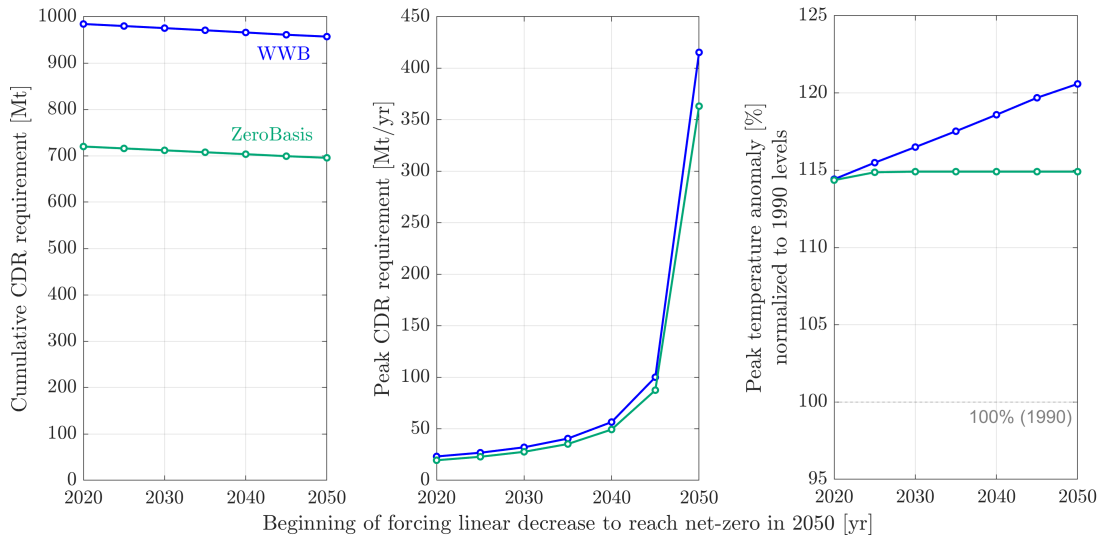


Figure 32. Cumulative CDR requirements (left panel), peak CDR requirements (middle panel) and peak warming (right panel) as a function of the beginning of CDR deployment when the policy objective is to achieve net-zero forcing by 2050. Delaying CDR deployment increases peak negative emissions requirements and peak warming, depending on the GHG emissions’ projected evolution until 2050. Cumulative CDR, on the other hand, is only slightly increased when early forcing reduction to net-zero is targeted.

13 Results for the Swiss aviation sector

In the context of the aviation sector, similar to the agriculture sector, two possible interpretations of the term ”net-zero Wirkung” (net-zero effect) in the KIG law are discussed.

Currently, as explained in Art. 3 of the ”*Bundesgesetz über die Ziele im Klimaschutz, die Innovation und die Stärkung der Energiesicherheit*”, only carbon dioxide emissions are considered within the aviation net-zero targets, while other atmospheric effects are excluded. However, the Swiss long-term climate strategy states that ”um bis im Jahr 2050 netto möglichst keine klimawirksamen Emissionen mehr zu verursachen, müssten auch Nicht-CO₂-Effekte berücksichtigt werden, was beispielsweise durch Entnehmen und Speichern von zusätzlichem CO₂ möglich ist”, requiring the need to consider aviation non-CO₂ effects in order to reduce the remaining climate-harmful emissions in 2050. These non-CO₂ effects could be addressed through flight-management practices or by removing and storing additional CO₂.

Therefore, this analysis examines the two policy targets separately for aviation-induced CO₂ emissions alone and for both CO₂ and non-CO₂ effects to provide a comprehensive understanding of the potential climate impacts and carbon dioxide removal (CDR) requirements in the aviation sector.

13.1 Aviation sector: CO₂ emissions

13.1.1 Target 1: Net-zero residual emissions in 2050

Aviation CO₂ emissions (over the time horizon from 1950 to 2150) and related climate impacts (over the time horizon from 1950 to 2300) are illustrated in Figure 33 for two of the projected future scenarios that we have already discussed: the business-as-usual WWB scenario (in blue) and the EP2050+ ZeroBasis scenario (in green). The four panels show, from left to right: (i) the emissions in percentage (left vertical axis), where 100% corresponds to the level of aviation-induced CO₂ emissions in 1990, while 0% represents their level at

the start of detectable anthropogenic aviation emissions, i.e., the year 1950; (ii) in the same first panel the CDR requirements in Mt/yr (right vertical axis) required to achieve Target 1, which is net-zero CO₂ emissions in 2050 with CDR starting from that year. Rates of CDR are negative numbers, in contrast to emissions that are positive; (iii) the cumulative CDR requirements needed to achieve the net-zero CO₂ emissions target when residual emissions follow either WWB or ZeroBasis (second panel); (iv) the associated radiative forcing for the WWB and ZeroBasis scenarios with and without CDR (third panel), where 100% is the corresponding level in 1990, and 0% that in 1950; (iv) the associated temperature anomaly for the WWB and ZeroBasis scenarios with and without CDR (fourth panel), where 100% is the corresponding level in 1990, and 0% that in 1950.

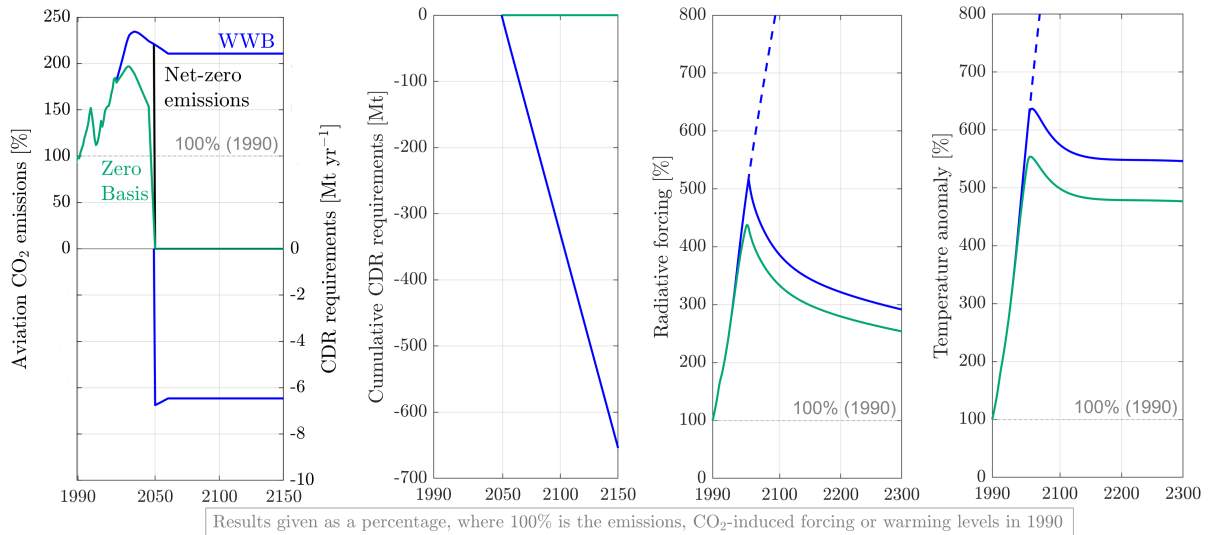


Figure 33. CDR requirements to achieve net-zero aviation-induced CO₂ emissions in 2050, starting negative emissions deployment from that same year, are calculated for the business-as-usual WWB scenario (in blue) and for the ZeroBasis projection (in green). In this latter scenario, carbon dioxide emissions are projected to phase out before 2050 from the 100% implementation of SAFs and bio-fuels, requiring therefore no CDR deployment. The second plot exhibits cumulative CDR requirements for the two scenarios; the third and fourth plot show radiative forcing and temperature anomaly (normalized by the respective CO₂-induced values in 1990) with CDR implementation (in solid lines) and without (in dashed lines) for the WWB and ZeroBasis scenarios.

A few remarks about the results in Figure 33 are worth making:

- In the EP2050+ ZeroBasis scenario CDR requirements remain zero, as this scenario assumes a complete transition to synthetic aviation fuels (SAFs) and biogenic fuels, effectively phasing out CO₂ emissions before 2050.
- In the WWB scenario, where fossil fuel consumption is only partially reduced, carbon dioxide removal at a rate of over 6 Mt/yr is required to achieve the goal of net-zero aviation CO₂ emissions by 2050, when CDR deployment is started from that same year.
- Evolution of CO₂ emissions to follow the ZeroBasis scenario can be regarded as unrealistic, as it is improbable for SAFs to cover 100% of the fuel requirements.²⁴
- Following the rapid halt in CO₂ emissions, the radiative forcing stabilizes from above. This is because, at that point, the only factor affecting the development of the CO₂ forcing is the exchange of a small portion of cumulative CO₂ from the atmosphere to other terrestrial compartments. This exchange

reduces the atmospheric concentration of carbon dioxide and, consequently, the radiative forcing and temperature anomaly. This phenomenon was previously reported in the literature¹⁰.

- Implementing CDR measures allows reducing radiative forcing and temperature anomaly in both scenarios compared to the case where CDR measures are not implemented. The difference between WWB and ZeroBasis forcing and temperature anomaly after CDR implementation, is given by the additional CO₂ emitted until 2050 in the WWB scenario.
- Nonetheless, with the implementation of a Target 1 policy to address CO₂ emissions forcing and temperature anomaly remain well above current warming levels, with the blue line (associated to WWB) causing approximately 70% more warming than ZeroBasis.

However, it is essential to note that in reality, long-term warming would continue to increase due to other non-CO₂ effects that are not currently explicitly considered in the KIG. This is shown in Figure 34, where the temperature anomaly is presented for the ZeroBasis and WWB projections with a Target 1 climate policy on CO₂ emissions when only carbon dioxide warming is considered (solid lines, as presented in the last plot of Figure 33) and when also the warming due to other non-CO₂ effects is taken into account (dashed lines). All temperature anomaly curves are normalized to aviation CO₂-induced warming in 1990 (100%).

As expected, when the warming from non-CO₂ effects, primarily from NO_x emissions and cirrus cloud formation, is taken into account, the temperature anomaly curve shifts to higher absolute values. Additionally, long-term temperature stabilization is eliminated because the non-CO₂ pollutants continue to induce warming, as they are not targeted by the climate policy. This highlights the importance of addressing these non-CO₂ effects to achieve effective climate mitigation in the aviation sector.

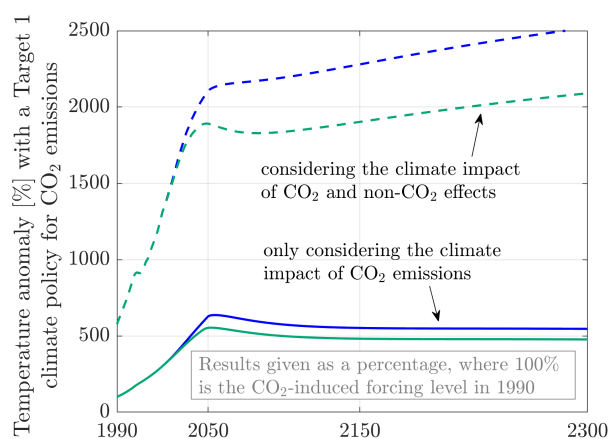


Figure 34. Temperature anomaly evolution for a CO₂-focused Target 1 policy when only carbon dioxide warming is considered (solid lines, as presented in the last plot of Figure 33) and when also the warming due to other non-CO₂ effects is taken into account (dashed lines). The dashed, green temperature anomaly curve is consistent to that of Figure 9 in Milestone 2. Here, all temperature anomaly curves are normalized to aviation CO₂-induced warming in 1990.

13.1.2 Target 2: Zero residual radiative forcing in 2050

The same diagrams as for target 1 are shown for target 2 in Figure 35. In this case the goal is to achieve zero residual radiative forcing from 2050 on, with CDR deployment starting in 2050; this is the radiative forcing profile shown as a red solid line in the third panel from the left in Figure 35. The negative emissions required to achieve Target 2 are depicted in negative values in the first panel of Figure 35 (right vertical axis).

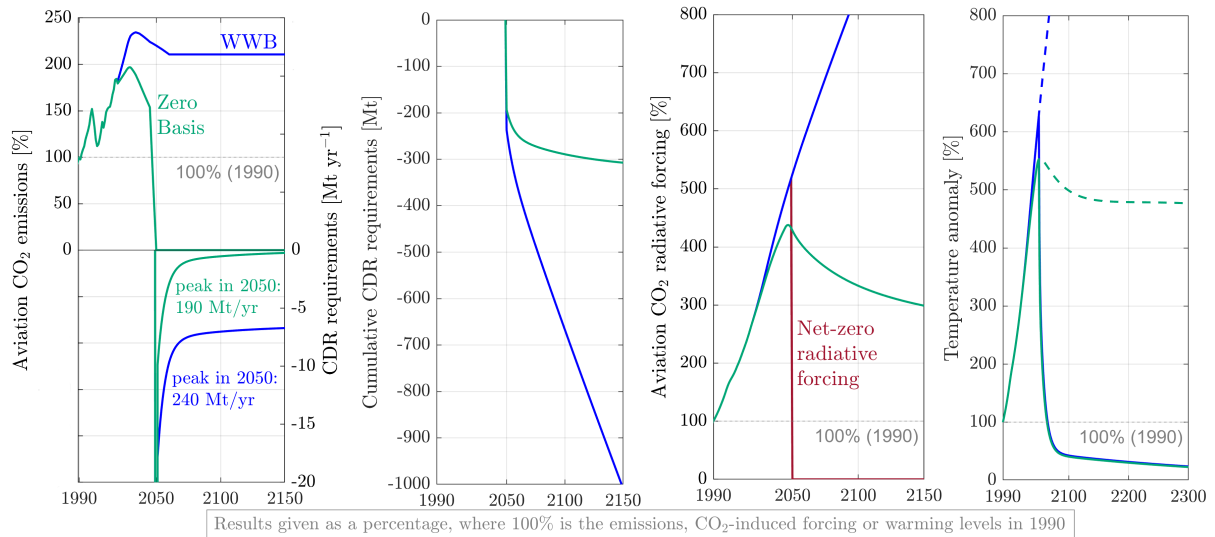


Figure 35. The first plot shows the CDR requirements to achieve net-zero forcing in 2050 (red line, third panel), starting negative emissions deployment from that same year. The analysis is performed for the business-as-usual WWB scenario (in blue) and for the ZeroBasis projection (in green). Achieving net-zero forcing, while only deploying CDR from that same target year, results in an unfeasible peak CDR demand. This can be lowered by an order of magnitude through the earlier deployment of CDR, which is shown in Figure 36, resulting therefore in a peak CDR requirement more comparable to that of a net-zero emissions objective (Target 1). The second plot exhibits cumulative CDR requirements for the two scenarios, while the third plot shows temperature anomaly (normalized by the respective CO₂-induced values in 1990) with CDR implementation (in solid lines) and without (in dashed lines) for the WWB and ZeroBasis scenarios. This last figure shows that achieving net-zero forcing allows for a sharp decrease in the temperature anomaly, and long-term stabilization to 0%, hence the warming at the beginning of significant aviation CO₂ emissions (i.e., 1950).

Also in this case a few remarks are worth making:

- Evolution of CO₂ emissions to follow the ZeroBasis scenario can be regarded as unrealistic, as it is improbable for SAFs to cover 100% of the fuel requirements.²⁴
- Here the rate of CDR requirements peaks in both scenarios in 2050, when it attains extremely, unrealistically high values of more than 190 Mt CO₂ per year. This is a consequence of the assumption that no CDR measures are implemented before 2050
- Implementing CDR measures to follow target 2 allows reducing radiative forcing and temperature anomaly in both scenarios at the same level, thus avoiding the major increase of warming above 1990 levels in case CDR measures are not implemented.
- Although very similar, for instance in their long term behavior, the evolution of the temperature anomaly differs in one critical feature. The peak temperature anomaly is almost 650% of that in 1990 in the WWB case, whereas it is 550% of that value in the ZeroBasis case. From a climate perspective this is a very large difference.
- Higher peak warming in the WWB scenario occurs because CO₂ emissions keep increasing at a fast rate until 2035, and only later they start to decrease. This higher peak warming can be mitigated either through accelerated emissions reduction, making the scenario more akin to the ZeroBasis projection, or else through earlier CDR implementation.

The issue of unfeasible high CDR peaks can be addressed by anticipating the deployment of CDR to before 2050, enforcing a linear reduction of forcing from the 2020 level to zero in 2050. This is illustrated in Figure 36, where it is apparent that the maximum rate of CDR deployment can be reduced by one order of magnitude to ca. 10 Mt CO₂ per year. Moreover, it can be seen that for both WWB and ZeroBasis, delaying CDR deployment considerably increases peak warming.

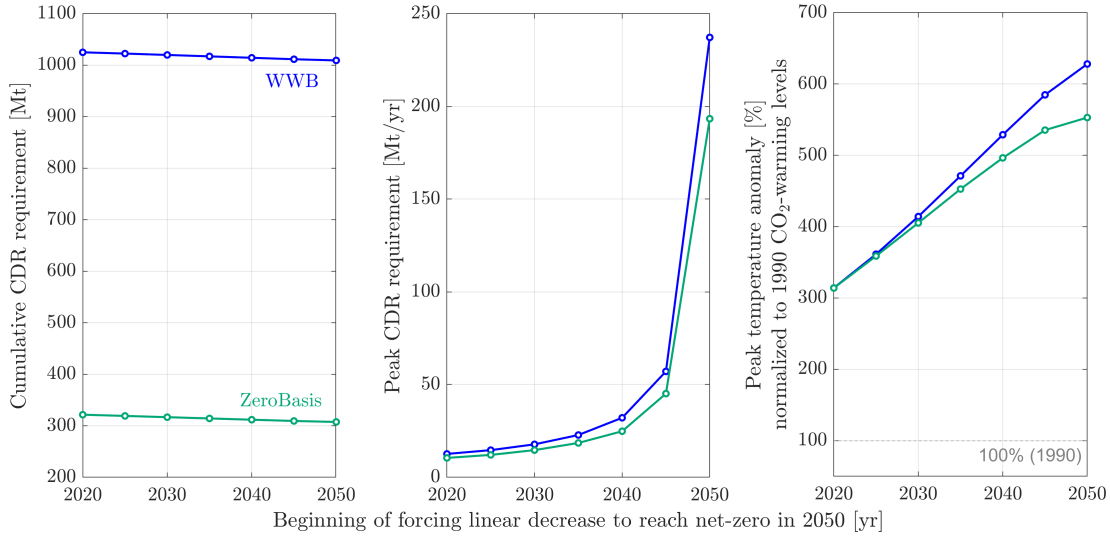


Figure 36. Cumulative CDR requirements (left panel), peak CDR requirements (middle panel) and peak warming (right panel) for the WWB and ZeroBasis projections under a target 2 policy that addresses only aviation induced CO₂ emissions, as a function of beginning CDR deployment year.

Finally, similarly to Target 1, when the warming from non-CO₂ effects is considered, the temperature anomaly curve shifts to higher absolute values. Additionally, long-term temperature stabilization is eliminated because the non-CO₂ pollutants continue to induce warming, as they are not targeted by the climate policy (which addresses only CO₂ emissions). This highlights the importance of addressing these non-CO₂ effects to achieve effective climate mitigation in the aviation sector.

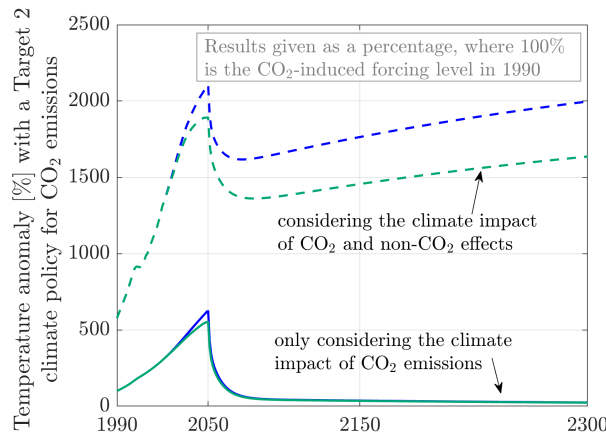


Figure 37. Temperature anomaly evolution for a CO₂-focused Target 2 policy when only carbon dioxide warming is considered (solid lines, as presented in the last plot of Figure 35) and when also the warming due to other non-CO₂ effects is taken into account (dashed lines). All temperature anomaly curves are normalized to aviation CO₂-induced warming in 1990.

13.2 Aviation sector: CO₂ emissions and non-CO₂ effects

As discussed in the previous section, addressing aviation-induced non-CO₂ effects within the target of a climate policy is instrumental to achieve true and effective climate mitigation in the aviation sector. Therefore, we analyze here again target 1, targeting net-zero emissions, and target 2, targeting net-zero forcing, from 2050 on (with CDR starting from that same year) in the scope of a climate policy that addresses not only CO₂ emissions but also other aviation-induced non-CO₂ effects. Of these, the largest climate impact comes from NO_x emissions and cirrus clouds formation.

Figure 38 illustrates, summarizes and compares the two possible interpretations of a net-zero "Wirkung" climate policy for the Swiss aviation sector, when both CO₂ emissions and non-CO₂ climate impacts are addressed. The top row shows the results of the WWB scenario, while the bottom row those of ZeroBasis. The four panels in each row show, from left to right: (i) the CDR requirements in Mt/yr (where rates of CDR are negative numbers); (ii) the cumulative CDR requirements needed to achieve the net-zero emissions and net-zero forcing targets; (iii) the associated radiative forcing for the WWB and ZeroBasis scenarios where CDR measures are deployed to achieve net-zero emissions (dashed, light-blue curve) and net-zero forcing (solid, dark blue line). Here 100% is the corresponding level of forcing in 1990, as a result of CO₂ and non-CO₂ impacts, and 0% that in 1950; (iv) the associated temperature anomaly for the two targets, where 100% is the corresponding CO₂ and non-CO₂ induced warming level in 1990, and 0% that in 1950. Curves associated with a Target 1 of net-zero emissions and with a Target 2 of zero radiative forcing are plotted in dash-dotted lines and in solid lines, respectively. WWB and ZeroBasis scenarios are visualized in blue and green colors, respectively.

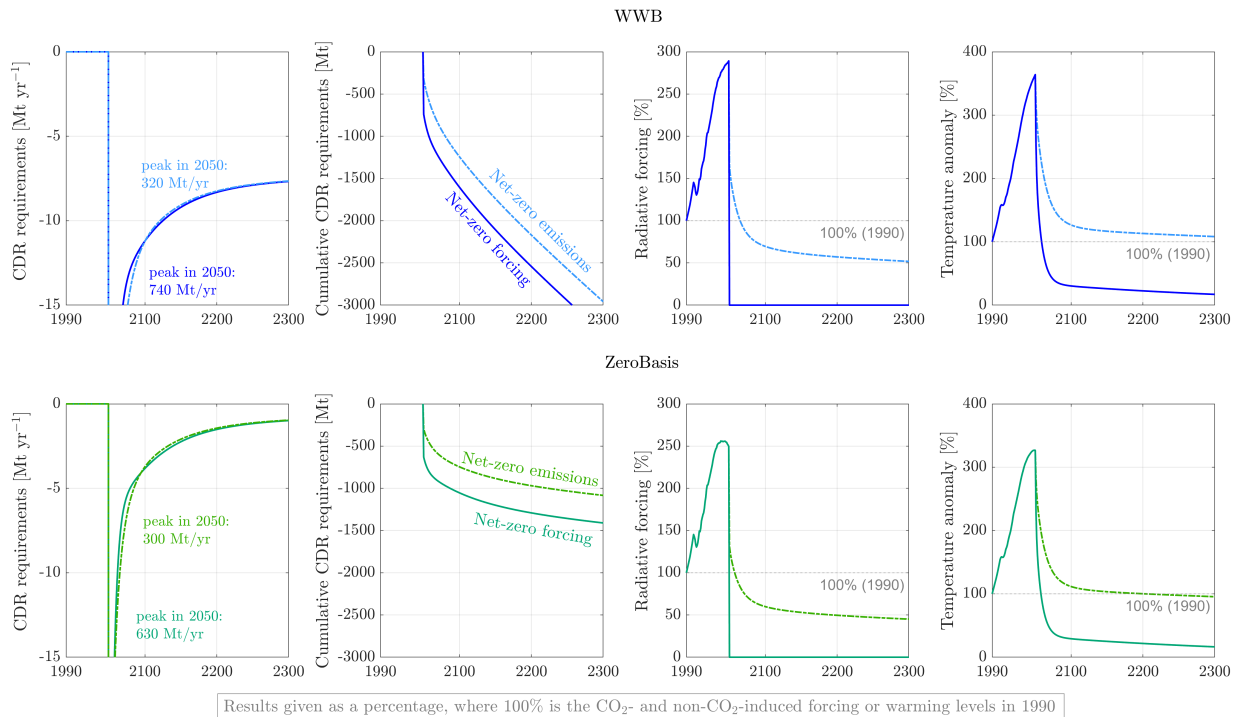


Figure 38. Comparative visualization of the two possible interpretations of a net-zero “Wirkung” climate policy for the Swiss aviation-induced CO₂ emissions, with CDR implementation only from 2050, and their corresponding impact on the CDR requirements, and the forcing and warming impact. Curves associated with a Target 1 of net-zero emissions are shown in dash-dotted lines and Target 2 of net-zero forcing in solid lines. WWB and ZeroBasis scenarios are identified in blue and green, respectively.

Target 1 and 3 do not halt warming in both scenario. Target 2 allows for a steeper decrease in temperature anomaly at the expense of a much higher and unfeasible CDR demand. Target 2 necessitates early deployment of CDR (i.e. already in the next 10 years) to decrease peak CDR requirements and increase feasibility. Cumulative CDR remains nonetheless higher for Target 2, than for Target 1.

A few remarks are worth making:

- The rate of CDR requirements peaks in both scenarios (i.e., ZeroBasis and WWB) and for both targets (i.e., 1 and 2) in 2050, when it attains extremely, unrealistically high values of more than 300 Mt CO₂ per year. This is a consequence of the assumption that no CDR measures are implemented before 2050.
- A target 1 of net-zero CO₂-emissions and non-CO₂ impacts, with CDR starting from 2050, allows for the temperature anomaly to be reduced to levels comparable to 1990. This reduction is attributed to the cooling effect from a net-zero target when applied to short-lived pollutants such as NO_x and cirrus clouds. In fact, as argued in the IPCC AR6²⁵, applying a target of net-zero emissions to short-lived greenhouse gas emissions reduces warming with respect to the peak temperature anomaly before the emissions decrease started. This effectively reduces the ongoing warming induced by CO₂ emissions that was illustrated in Figure 33, allowing for the temperature anomaly to be reduced to 1990 levels.
- Net-zero forcing allows instead for a steeper reduction in the temperature anomaly as well as a lower final temperature anomaly.
- It holds true that adhering to a ZeroBasis scenario, where emissions increase less from 2020 onward with respect to WWB, allows for a lower peak warming, namely approximately 50% lower.

The first issue can be again addressed by anticipating the deployment of CDR to before 2050, enforcing a linear reduction of forcing from the 2020 level to zero in 2050. This is illustrated in Figure 39 for target 1; target 2 is not further analyzed in this context as it requires unachievable high levels of CDR deployment. This is illustrated in Figure 39, where it is apparent that the maximum rate of CDR deployment can be reduced by one order of magnitude, i.e., to ca. 25-30 Mt CO₂ per year; this remains a considerably high CDR peak deployment though. Moreover, it can be seen that for both WWB and ZeroBasis, delaying CDR deployment greatly increases peak warming.

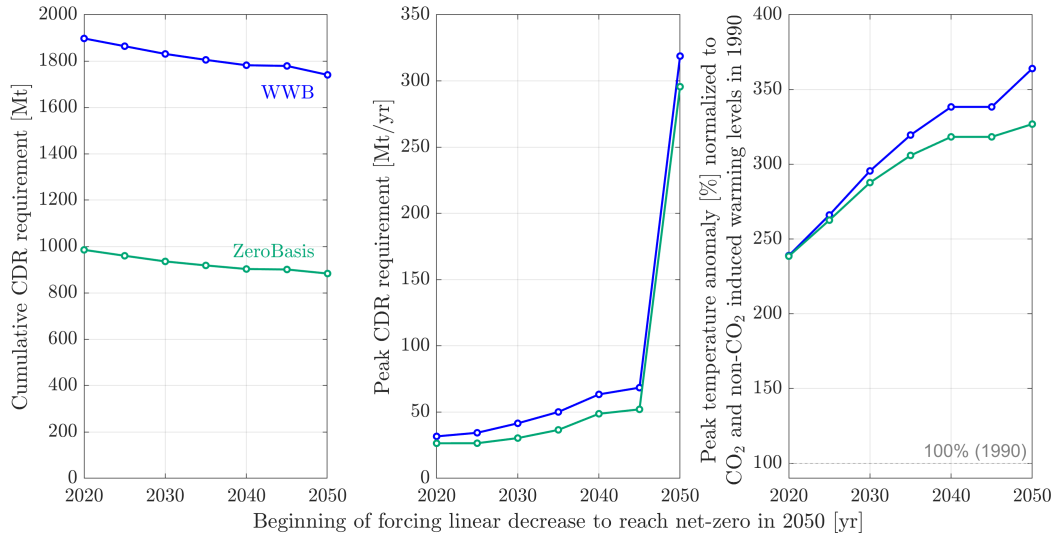


Figure 39. Cumulative CDR requirements (left panel), peak CDR requirements (middle panel) and peak warming (right panel) for the WWB and ZeroBasis projections under a target 1 policy that addresses both aviation induced CO₂ and non-CO₂ effects, as a function of beginning CDR deployment year.

Appendices

A Appendix Milestone 1

A.1 Global warming potential (GWP)

Based on Myhre et al.¹⁴ (IPCC 2013), the global warming potential (GWP) for gas i is calculated as

$$GWP_i(H) = \frac{AGWP_i(H)}{AGWP_{CO_2}(H)} = \frac{\int_0^H F_i(t) dt}{\int_0^H F_{CO_2}(t) dt}, \quad (34)$$

where the absolute global warming potential (AGWP) is the time-integrated radiative forcing due to 1 kg pulse emission of gas i (usually in $W m^{-2} yr kg^{-1}$), H is the time horizon in years, and F_i is the radiative forcing due to a pulse emission of a gas i , given by

$$F_i(t) = A_i R_i(t). \quad (35)$$

A_i [$W m^{-2} kg^{-1}$] is defined in the paper as "the F_i per unit mass increase in atmospheric abundance of species i ", or alternatively, as radiative efficiency (RE_i). Regarding the assumption of A_i being time-independent, it is important to acknowledge that its validity may vary depending on specific circumstances. According to Joos *et al.*²⁶, "for sufficiently small emissions and approximately constant background," the assumption of time invariance for A_i can be a reasonable approximation. In practical terms, this means that under certain conditions, it is acceptable to treat A_i as a constant value over time, especially when emissions are relatively small and the background conditions remain relatively stable. However, in cases of significant emissions or when background conditions are rapidly changing, the time-invariance assumption may no longer hold, and a more dynamic representation of A_i may be necessary.

Instead, $R_i[-]$ represents the fraction of species i that remains in the atmosphere following a pulse emission event. In essence, it serves as a proxy for the evolution of the concentration of species i , taking into account various processes such as chemical reactions or absorption that affect the persistence of the species in the atmosphere. R_i can also be referred to as the impulse response function (*IRF*). Since its reference value is 1 at the beginning, it can indeed be interpreted as a fraction representing the fraction of species i remaining in the atmosphere following an emission event. For most species R_i is based on a simple exponential decay:

$$R_i(t) = \exp\left(-\frac{t}{\tau_i}\right) \quad (36)$$

where τ_i is the perturbation lifetime of CF_i . Thus, for non- CO_2 species:

$$AGWP_i(H) = \int_0^H F_i(t) dt = A_i \tau_i \left(1 - \exp\left(-\frac{H}{\tau_i}\right)\right) \quad (37)$$

For CO_2 , R_{CO_2} is calculated using a more complex expression as this pollutant is partitioned between terrestrial compartments and does not decay:

$$R_{CO_2}(t) = a_0 + \sum_{j=1}^{N(=3)} a_j \exp\left(-\frac{t}{\tau_{CO_2,j}}\right) \quad (38)$$

It follows the $AGWP_{CO_2}$ mathematical expression:

$$AGWP_{CO_2}(H) = A_{CO_2} \left(a_0 H + \sum_{j=1}^{N(=3)} a_j \tau_{CO_2,j} \left(1 - \exp\left(-\frac{H}{\tau_{CO_2,j}}\right)\right) \right) \quad (39)$$

The two equations above are reported by Myhre et al.¹⁴ with imprecision, and are originally taken from Joos et al.²⁶. Table 2 reports the values of a_j and $\tau_{CO_2,j}$ for CO₂ from the same references. As per our knowledge, the values documented in Table Table 2 represent the most up-to-date and accurate information available regarding these coefficients.

Table 2. CO₂ characteristic times, $\tau_{CO_2,j}$, and parameters, a_j , for Equation (6)^{14,26}

	$j = 0$	$j = 1$	$j = 2$	$j = 3$
a_j [-]	0.2173	0.2240	0.2824	0.2763
$\tau_{CO_2,j}$ [yr]	–	394.4	36.54	4.304

The absolute global temperature change potential for a pulse emission of 1 kg of a substance i ($AGTP$, $K\ kg^{-1}$) is defined as

$$AGTP_i(H) = \int_0^H F_i(t) R_T(H-t) dt \quad (40)$$

where R_T is the "climate response to a unit forcing" (as defined in the IPCC) or the "impulse response function for a global-mean surface temperature" (as defined in Shine et al.¹⁶). R_T is represented by a sum of exponentials, highlighting the two timescale of temperature anomaly evolution (s_1 and s_2).

$$R_T(t) = \sum_{k=1}^2 \frac{q_k}{s_k} \exp\left(-\frac{t}{s_k}\right) \quad (41)$$

R_T [$K\ W^{-1}\ m^2\ yr^{-1}$] characterizes the effect of radiative forcing on the Earth's climate system, independently of the type of pollutant. This parameter quantifies the temperature response of the planet to changes in radiative forcing, making it a fundamental measure of how the climate reacts to external influences, regardless of the specific factors driving those changes. The values of the s_k and q_k coefficients are discussed in Section 3.5.

The $AGTP$ for a species i other than CO₂ then becomes

$$AGTP_i(H) = A_i \tau_i \sum_{k=1}^2 \frac{q_k}{\tau_i - s_k} \left(\exp\left(-\frac{H}{\tau_i}\right) - \exp\left(-\frac{H}{s_k}\right) \right). \quad (42)$$

This equation is mathematically invalid if $\tau_i = s_k$; for this specific case an expression is given by Shine et al.²⁷. It is also important to reiterate that when a pollutant other than CO₂ is emitted in a pulse, it results in an exponentially decreasing radiative forcing over time, rather than a pulse forcing. Consequently, the $AGTP$ is not a strictly monotonic function of time (H) due to the convolution integral. The maximum $AGTP$ occurs some years after the emission event, reflecting the time-delayed impact of the pollutant on global temperatures. This temporal delay is a significant factor to consider when assessing the full climate impact of emissions of certain substances.

For CO₂, instead, the $AGTP$ is defined as follows:

$$AGTP_{CO_2}(H) = A_{CO_2} \left[a_0 \sum_{k=1}^2 q_k \left(1 - \exp\left(-\frac{H}{s_k}\right) \right) + \sum_{k=1}^2 q_k \sum_{j=1}^3 \frac{a_j \tau_{CO_2,j}}{\tau_{CO_2,j} - s_k} \left(\exp\left(-\frac{H}{\tau_{CO_2,j}}\right) - \exp\left(-\frac{H}{s_k}\right) \right) \right] \quad (43)$$

A (the radiative efficiency, RE) may be given with units of [$W\ m^{-2}\ ppbv^{-1}$] or [$W\ m^{-2}\ kg^{-1}$]. To convert values given per ppbv to per kg, they must be multiplied by $\left(\frac{M_{air}}{M_i}\right)\left(\frac{10^9}{m_a}\right)$, where M_i is the molar mass of the compound i , $M_{air} = 28.97\ kg\ kmol^{-1}$ that of air, and $m_a = 5.1352 \times 10^{18}\ kg$ is the mass of the atmosphere.

Table 3. Radiative properties of carbon dioxide, methane and nitrous oxide.

Source	Radiative efficiency A [$\text{W m}^{-2} \text{kg}^{-1}$]		
	CO_2	CH_4	N_2O
Ramaswamy et al. ²⁸ (2001) ^a	–	1.3×10^{-13}	4.0×10^{-13}
Myhre et al. ²⁹ (2013) ^b	1.76×10^{-15}	1.28×10^{-13}	3.85×10^{-13}
Forster et al. ¹⁹ (2021) ^c	$1.70 \pm 0.21 \times 10^{-15}$	$2.0 \pm 0.5 \times 10^{-13}$	$3.6 \pm 1.4 \times 10^{-13}$

^a The value reported for CO_2 is 3 orders of magnitude larger, indicating a different definition of Equation (38).

^b The uncertainty is defined as 10%.

^c The values of A include chemical adjustments.

Table 4. Perturbation Lifetimes

Source	Perturbation lifetime τ [yr]	
	CH_4	N_2O
Ramaswamy et al. ²⁸ (2001)	12.0	114
Myhre et al. ²⁹ (2013)	12.4	121
Forster et al. ¹⁹ (2021)	11.8 ± 1.8	109 ± 10

Table 3 and Table 4 report values of A and τ , respectively, that can be found in the IPCC reports with their corresponding literature sources. In this study, the most-up-to-date values of radiative efficiency (A) and characteristic times (τ) are employed, namely the values reported by Forster et al. ¹⁹, with the exception of $\tau_{\text{N}_2\text{O}}$ which is set to 121yr in accordance to FAIR v1.3.³

The latest values of Global Warming Potential (GWP) and Absolute Global Warming Potential ($AGWP$) from the 2021 IPCC report^{3,19} are provided in Table Table 5. However, it's important to acknowledge that different values for radiative efficiency are reported throughout the IPCC 2021 report, which can lead to some confusion regarding which values to use.

For instance, in Table 7.15, a radiative efficiency of $5.7 \pm 1.4 \times 10^{-4} \text{ W m}^{-2} \text{ ppbv}^{-1}$ is reported for both fossil and non-fossil methane, yet different GWP values are presented (29.8 ± 11 and 27.0 ± 11 , respectively, at 100 years). In Section 7.6.1, a value of $3.89 \times 10^{-4} \text{ W m}^{-2} \text{ ppbv}^{-1}$ is reported, which corresponds to a GWP_{100} of 27.9 according to Table 7.SM.7. It is also relevant to note that in Table 7.SM.8, Smith et al. ³⁰ report a total uncertainty for the GWP_{20} and GWP_{100} of CH_4 of 32 and 40%, respectively. For N_2O , the uncertainties are 43 and 47%, respectively.

Table 5. GWP [–] and $AGWP$ [$\text{pW m}^{-2} \text{ yr kg}^{-1}$] reported in Table 7.SM.7 by Smith et al. ³⁰

Gas	GWP_{20}	GWP_{100}	$AGWP_{20}$	$AGWP_{100}$
CO_2	1	1	0.0243	0.0895
CH_4	81.2	27.9	1.98	2.49
N_2O	273	273	6.65	24.5

The values of perturbation lifetimes and radiative properties associated with aviation-induced emissions, including substances like NO_x (nitrogen oxides) and SO_x (sulfur oxides), have been sourced from⁶. These values are reported in Table 6.

Table 6. Perturbation lifetimes and radiative properties for aviation emissions by Sacchi et al.⁶

Species	Lifetime [years]	Molecular mass [g/mol]	Radiative efficiency A [W/(m ² kg) or W/(m ² km) for cirrus]
NO _x	11.8	46.01	1.67×10^{-12}
SO _x	0.011	64.07	-1.10×10^{-10}
BC	0.02	12.01	5.54×10^{-10}
H ₂ O	0.8	18.02	2.86×10^{-14}
cirrus	0.00057		9.36×10^{-13}

A.2 GWP*

Conventionally, CO₂-equivalent (CO₂-eq.) emissions for a non-CO₂ pollutant are defined as follows:

$$E_{\text{CO}_2\text{e}}(t) = E_{\text{SLCP}}(t)GWP_{H,\text{SLCP}} \quad (44)$$

where E denotes the emissions (in this case of a short-lived climate pollutant, SLCP) and GWP_H the equivalence factor (i.e., usually GWP_{100} or GWP_{20}).

As first proposed by Allen et al.³¹, equivalent CO₂ emissions can be calculated by means of the revised GWP* equivalence metric as follows:

$$E_{\text{CO}_2\text{e}^*} = \frac{\Delta E_{\text{SLCP}}}{\Delta t} GWP_{H,\text{SLCP}} H \quad (45)$$

where typically $\Delta t = 20$ yr and $H = 100$ yr. The rate-based equivalence for short-lived climate pollutants (SLCPs), as expressed in Equation (45), addresses the issues associated with traditional Global Warming Potential (GWP) metrics, which do not adequately distinguish the largely non-cumulative behavior of SLCPs. However, as witnessed in the simulations and also pointed out by¹⁰, even though a sustained rate of SLCP emissions will result in a stable atmospheric concentration and maintain a constant level of radiative forcing, there will still be some additional long-term warming occurring while the climate system is in the process of equilibrating to past increases in SLCP emissions.

It is important to emphasize that this additional warming is not a cumulative impact of emissions akin to that of carbon dioxide (CO₂). Instead, it represents a delayed response associated with the system's equilibration to a past increase in radiative forcing (as identifiable from the long characteristic timescale of climate response, s_1). To account for this delayed response, the authors¹⁰ propose a modified equation for calculating CO₂-equivalent emissions. This modification aims to provide a more accurate representation of the climate impact of SLCP emissions while considering the time-delayed nature of any pollutant's effects.

$$E_{\text{CO}_2\text{we}} = GWP_{H,\text{SLCP}} \left(r \frac{\Delta E_{\text{SLCP}}}{\Delta t} H + s E_{\text{SLCP}} \right) \quad (46)$$

where CO₂we stands for CO₂-warming-equivalent, ΔE_{SLCP} the change in SLCP emission rate over the preceding Δt years, E_{SLCP} the SLCP emissions for that year, and r and s the weights assigned to the rate and stock contributions, respectively. By setting $r = 1$ and $s = 0$, Equation (46) reduces to Equation (45). The second term, arising when s is nonzero, represents the long-term equilibration to past increases in forcing.

GWP*, as described in Cain et al.¹⁰, is a lumped expression trying to describe: (i) the dissimilar ways in which emissions and radiative forcing from SLCPs (e.g., methane) and persistent pollutants (e.g., carbon dioxide) behave due to their varying lifetimes; ii) the processes and mechanisms governing the evolution of surface temperature anomalies.

GWP* is an empirical model characterized by an expression that relies on parameters (i.g., r , s , H) calibrated for specific scenarios. It is important to note that GWP* is not universally applicable to all cases and cannot be extrapolated to scenarios that greatly differ from the one for which it has been calibrated. For example, both values of r and s are compound- and scenario-dependent. For methane, $r = 0.75$ and $s = 0.25$ ($r + s = 1$, further explanation is provided in literature¹⁰). For nitrous oxide, these values of r and s parameters are not valid and the GWP* empirical definition cannot be employed as it is (re-calibration of GWP* to better describe the climate impact of N₂O is discussed in Appendix B.4).

An updated definition of GWP* was later proposed³², introducing a $g(s)$ factor. The latest formulation of GWP* is the following:

$$E_{CO_2we} = gGWP_{H,SLCP} \left((1-s) \frac{\Delta E_{SLCP}}{\Delta t} H + sE_{SLCP} \right) \quad (47)$$

For methane, Equation (47) can be rewritten as Equation (48)^{12,32} for $GWP_{100} = 28.3$ ²⁶.

$$E_{CO_2we}(t) = 128E_{CH_4}(t) - 120E_{CH_4}(t-20) \quad (48)$$

Instead, for an arbitrary SLCP, Equation (47) can be rewritten as follows:

$$E_{CO_2we}(t) = GWP_{100,SLCP} (4.53E_{SLCP}(t) - 4.25E_{SLCP}(t-20)) \quad (49)$$

To calculate the equivalent emissions of a SLCP for an emission profile of CO₂ under GWP*, the equation is inverted, leading to

$$E_{SLCP}(t) = \frac{E_{CO_2we}(t)}{4.53GWP_{100,SLCP}} + \frac{4.25}{4.53} E_{SLCP}(t-20) \quad (50)$$

A.3 Global mean surface temperature (GMST) change

The temperature anomaly resulting from a perturbation in atmospheric forcing caused by a pollutant's emissions can be computed with the global mean surface temperature (GMST) change per unit emission or offset emission, as described in²⁹. The following definition of ΔT_{GMST} is consistent with, and can be derived from, the physical equations presented in Section 3.5.

$$\Delta T_{GMST}(t) = \sum_i \int_0^t E_i(s) AGTP_i(t-s) ds \quad (51)$$

In discrete form, the above equation can be rewritten as follows³³:

$$\Delta T_{GMST}(t) = \sum_{t_e=0}^t \left[\sum_i E_i(t_e) AGTP_i(t-t_e) \right] \quad (52)$$

Mathematically, the computation can be simplified by realizing that

$$\Delta \mathbf{T}_{GMST} = \mathbf{P}_i \mathbf{E}_i \quad (53)$$

where \mathbf{P} is the lower triangular Toeplitz matrix whose first column is $(\mathbf{P}_i)_i = AGTP_i$. Toeplitz matrices have the same values along each descending diagonal from left to right. Thus, to fully define \mathbf{P}_i it is sufficient to define its first column.

A.4 Linear warming equivalence (LWE)

The concept of linear warming equivalent emissions has been presented by Allen et al.¹² to ensure that offsetting emissions of a given gas with another one does not result in a different global warming effect.

Let us assume that emissions of gas A are offset by emissions of gas B. Then, the same warming effect happens if the forcing profile is the same for the emissions of both gases:

$$\int_0^t A_A R_A(t-t') E_A(t') dt' = \int_0^t A_B R_B(t-t') E_B(t') dt' \quad (54)$$

The problem can be solved by noting that the forcing timeseries resulting from an emission timeseries of gas A can be expressed as

$$\mathbf{f} = \mathbf{F}_A \mathbf{E}_A \quad (55)$$

where \mathbf{f} is the row vector containing the forcing over the years, \mathbf{E}_A is the column vector containing the emissions of gas A over the years, and \mathbf{F}_A is a lower-diagonal Toeplitz matrix. Toeplitz matrices have the same values along each descending diagonal from left to right. Thus, to fully define \mathbf{F}_A it is sufficient to define its first column. The first column contains the first derivative of the *AGWP* of gas A, which is known as the *Absolute Global Forcing Potential (AGFP)*. Taking an interval of 1 yr to compute the discrete derivative, $(\mathbf{F}_A)_{i,1} = AGWP_i - AGWP_{i-1} = AGFP_i$ according to Allen et al.¹². For computational purposes, however, it seems more appropriate to extend by one year the time horizon and use the following: $(\mathbf{F}_A)_{i,1} = AGWP_{i+1} - AGWP_i = AGFP_i$. \mathbf{F}_A is generally invertible. Finally, the emissions of gas B can be computed as

$$\mathbf{E}_B = \mathbf{F}_B^{-1} \mathbf{F}_A \mathbf{E}_A \quad (56)$$

A.5 Implementation

All sets of equations reported above have been implemented in Matlab in an object-oriented fashion, thus allowing to perform simulations with simplicity. The correctness of the implementation has been tested by reproducing the calculations by Allen et al.¹², leading to the plots in Figure 40.

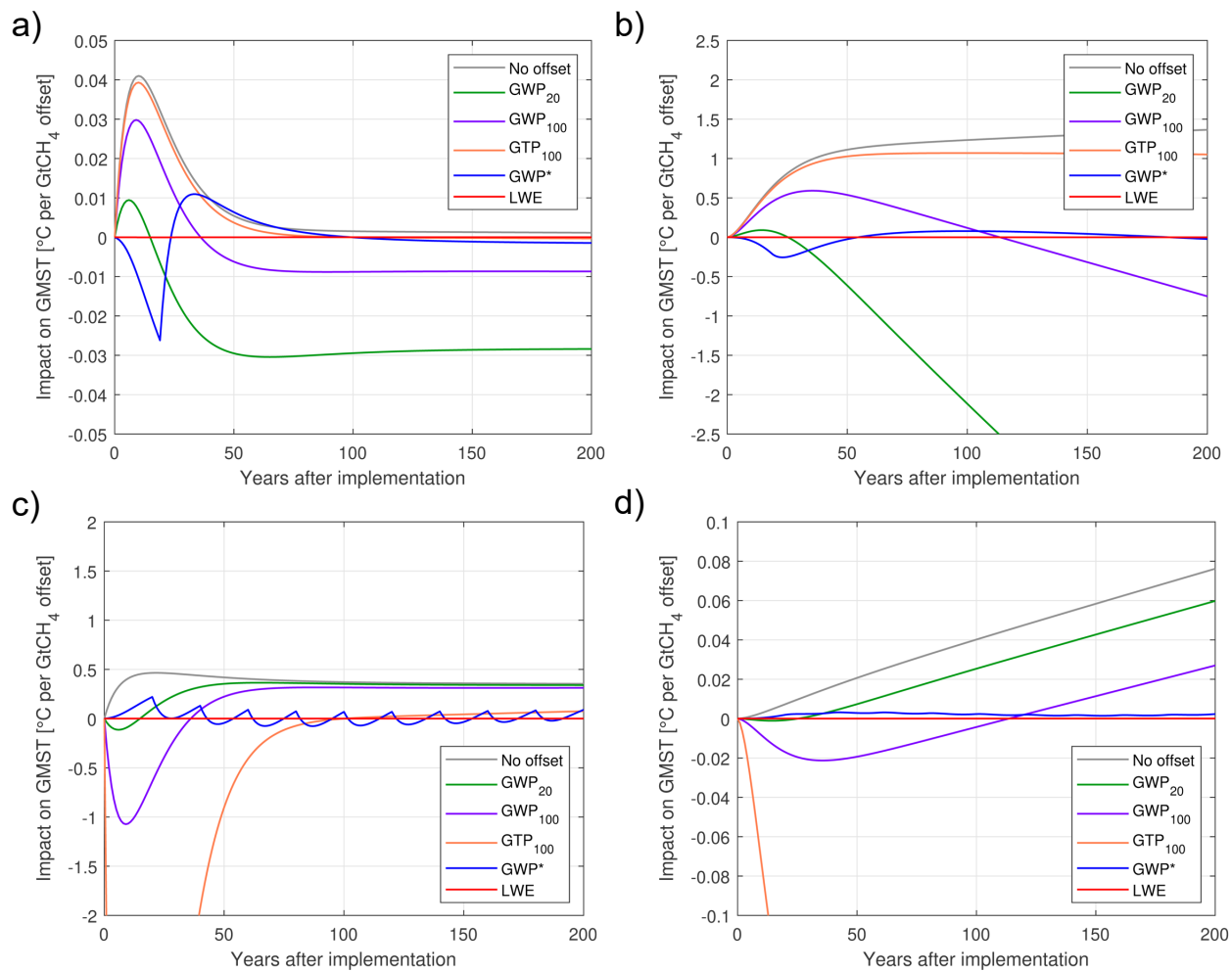


Figure 40. Reproduced results originally published by Allen et al.¹². Panels (a) and (b) correspond to Figure 1 of the referenced work. Panels (c) and (d) correspond to Figure 2 of the referenced work.

B Appendix Milestone 2

B.1 Agriculture sector

B.1.1 GHGs contributions of the total agriculture climate impact

Figure 41 analyzes the total mass of GHGs emitted, as well as the total generated forcing and temperature perturbations from Swiss agriculture activity since 1690, and it illustrates the contribution of each greenhouse gas, namely CH₄, N₂O, and CO₂, to the overall total.

It can be observed that of the total mass of GHG emissions, CO₂ accounts for approximately one-fourth (in all scenarios). However, when looking at the total radiative forcing, CO₂ plays a negligible role, while CH₄ and N₂O have a more significant impact on the climate. In the WWB projection, where emissions of all pollutants are kept constant from 2020 onward, CH₄ is the largest climate contributor throughout the entire timeline. However, it's worth noting that the contribution of N₂O increases over time because the radiative forcing of this longer-lived climate forcer takes longer to reach stability than that of the short-lived methane. As a result, it continues to increase for a while after emissions have plateaued (see Figure 5 for reference). Furthermore, for decreasing emissions scenarios like ZeroBasis and Scenario D, the contribution of N₂O to the total radiative forcing becomes more important relative to CH₄. This is because, for the same rate of

emissions reduction, the forcing of fast-reacting methane decreases more rapidly than that of N₂O, as can be observed in Figure 5.

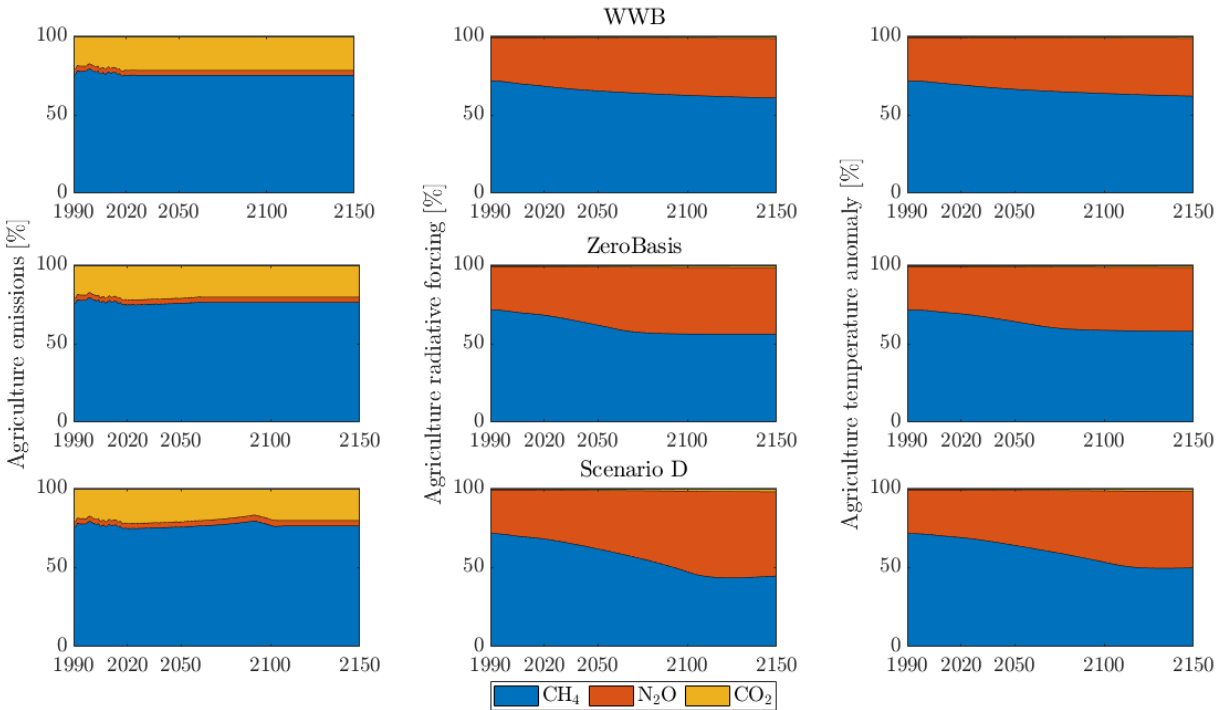


Figure 41. Percentage contribution of each greenhouse gas, namely CH₄, N₂O and CO₂, to the total mass of GHGs emitted, and the total generated forcing and temperature perturbations from the Swiss agriculture activity since 1690. CO₂, while being emitted in large quantities, plays a very negligible role in the total climate impact of the Swiss agriculture while CH₄ and N₂O are found as the largest contributors. The climate importance of N₂O increases with time, especially in scenarios where emissions are reduced. This temporal factor is directly attributable to the longer life time of this GHG, which results in a longer time scale required for the radiative forcing, and hence temperature anomaly, to reach stability.

B.1.2 CO₂-equivalence metrics for non-CO₂ climate forcers: the effect on the radiative forcing and temperature anomaly

Simulations of equivalent CO₂ emissions for the methane and nitrous oxide agriculture emissions of the ZeroBasis scenario are shown in Figure 42, alongside simulations of the radiative forcing and temperature anomaly curves for the equivalent CO₂ amounts as calculated with the different metrics. The results for the WWB and Scenario D projections follow in Figure 43 and Figure 44.

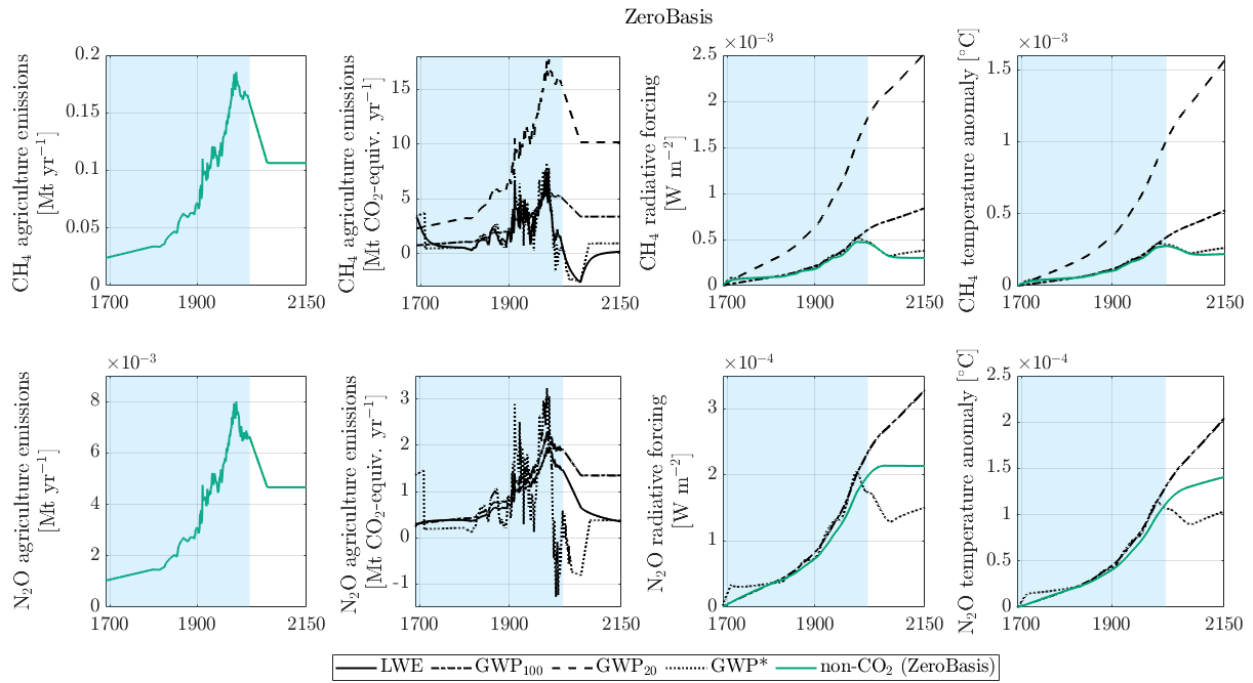


Figure 42. CO₂-equivalents, as calculated by means of the GWP₁₀₀, GWP₂₀, GWP* and LWE metrics, of methane (top row) and nitrous oxide (bottom row) emissions for the ZeroBasis scenario. The radiative forcing and temperature anomaly curves are calculated for the non-CO₂ emissions (green curves) and for the CO₂-equivalents as calculated with the different metrics. The climate impact calculated from LWE-CO₂-equivalents provides an exact fit to the impact of a non-CO₂ forcer, both short-live and long-lived. The GWP₁₀₀ and GWP₂₀ provide a correct equivalence at a specific point in time (i.e., around 20 and 100y years, respectively, from beginning of the time series analyzed). However they underestimate the required CO₂-equivalents before then, and greatly overestimate them thereafter (for both LLCFs and SLCFs), as they do not account for the decay of non-CO₂ GHGs. Lastly, the GWP* equivalence metric performs well for CH₄, as it was calibrated for this GHG, but badly for the longer-lived N₂O.

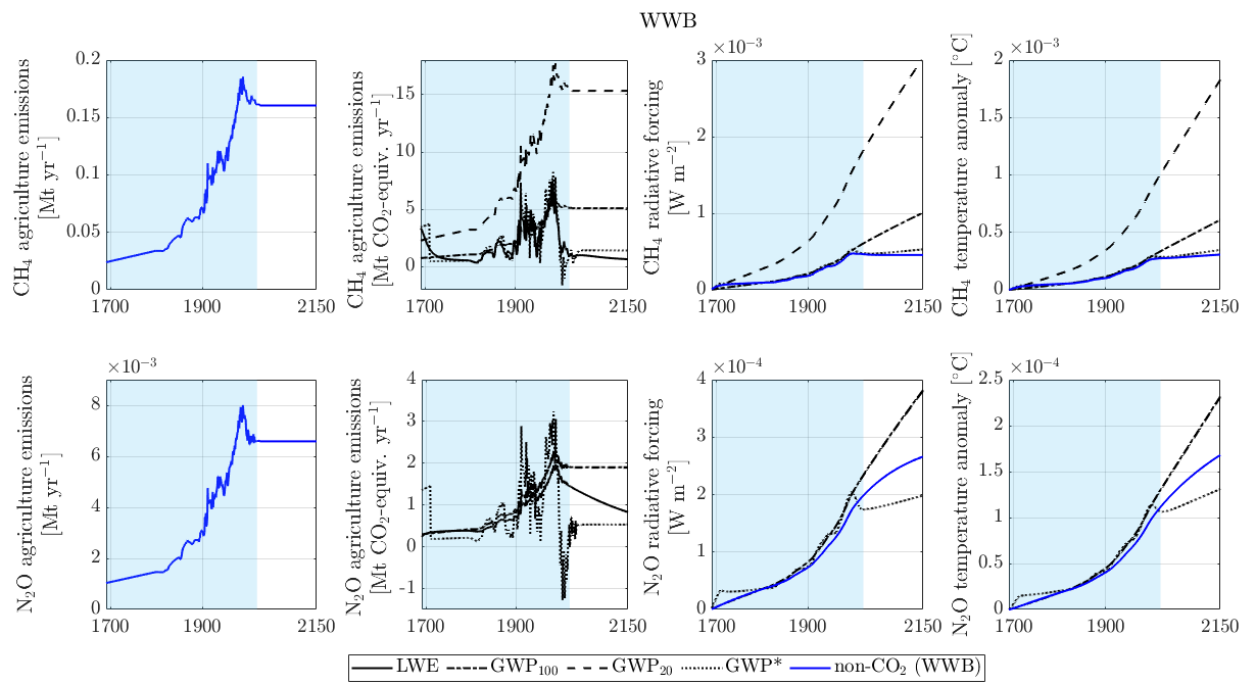


Figure 43. CO₂-equivalents, as calculated by means of the GWP₁₀₀, GWP₂₀, GWP* and LWE metrics, of methane (top row) and nitrous oxide (bottom row) emissions for the WWB scenario. The radiative forcing and temperature anomaly curves are calculated for the non-CO₂ emissions (blue curves) and for the CO₂-equivalents as calculated with the different metrics. The climate impact calculated from LWE-CO₂-equivalents provides an exact fit to the impact of a non-CO₂ forcer, both short-live and long-lived. The GWP₁₀₀ and GWP₂₀ provide a correct equivalence at a specific point in time (i.e., around 20 and 100y years, respectively, from beginning of the time series analyzed). However they underestimate the required CO₂-equivalents before then, and greatly overestimate them thereafter (for both LLCFs and SLCFs), as they do not account for the decay of non-CO₂ GHGs. Lastly, the GWP* equivalence metric performs well for CH₄, as it was calibrated for this GHG, but badly for the longer-lived N₂O.

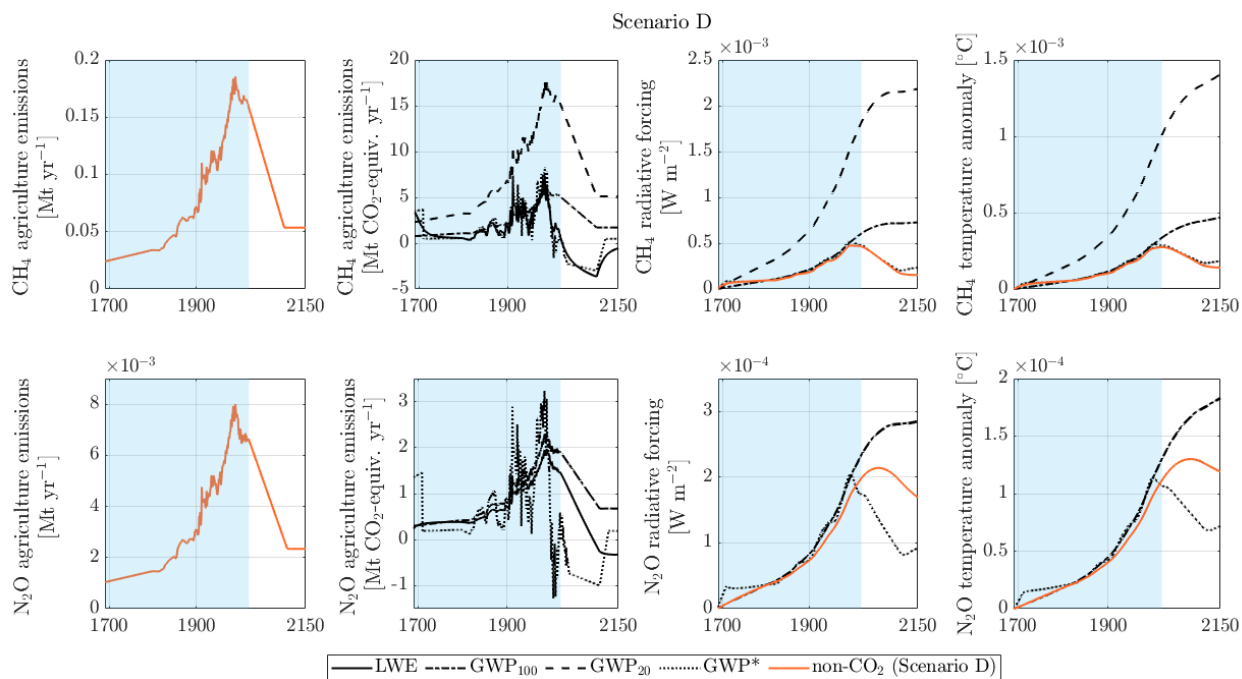


Figure 44. CO₂-equivalents, as calculated by means of the GWP₁₀₀, GWP₂₀, GWP* and LWE metrics, of methane (top row) and nitrous oxide (bottom row) emissions for the Scenario D. The radiative forcing and temperature anomaly curves are calculated for the non-CO₂ emissions (orange curves) and for the CO₂-equivalents as calculated with the different metrics. The climate impact calculated from LWE-CO₂-equivalents provides an exact fit to the impact of a non-CO₂ forcer, both short-live and long-lived. The GWP₁₀₀ and GWP₂₀ provide a correct equivalence at a specific point in time (i.e., around 20 and 100y years, respectively, from beginning of the time series analyzed). However they underestimate the required CO₂-equivalents before then, and greatly overestimate them thereafter (for both LLCFs and SLCFs), as they do not account for the decay of non-CO₂ GHGs. Lastly, the GWP* equivalence metric performs well for CH₄, as it was calibrated for this GHG, but badly for the longer-lived N₂O.

Emissions of methane and nitrous oxide for the ZeroBasis scenario are reported in the first column of Figure 42, and their corresponding radiative forcing and temperature anomaly are shown in green in the third and fourth columns of Figure 42, respectively. The second column reports emissions in CO₂-equivalents as calculated by means of the four equivalence metrics, namely the GWP₁₀₀, GWP₂₀, GWP*, and LWE.

GWP₁₀₀ and GWP₂₀ are metrics that establish CO₂-equivalence for non-CO₂ climate forcers in a proportional manner. Therefore, to find equivalent CO₂ emissions, the emissions of methane and nitrous oxide are simply multiplied by their respective values of the chosen metric. Values of GWP₁₀₀ and GWP₂₀ for CH₄ and N₂O are found in Table 5 of the Appendix.

However, it's important to note that these metrics have recently been recognized as questionable because they are non-physical. They do not accurately express the fundamental difference between the physical behavior of non-CO₂ and CO₂ climate forcers, namely that non-CO₂ forcers decay over time while CO₂ does not. The factors associated with these metrics (Table 5) express correct CO₂-equivalence at a specific point in time, but they perform poorly when handling a time series of emissions. As a result, they do not ensure a correct equivalence in terms of climate impact, which could compromise the achievement of long-term climate goals.

The shortcomings of these metrics become evident when examining the radiative forcing and temperature anomaly curves derived from the calculated CO₂-equivalent emissions. For methane, both the GWP₁₀₀-

CO₂-equivalents and GWP₂₀-CO₂-equivalents initially (within the first approximately 100 and 20 years, respectively) underestimate the actual climate impact, as seen in the green radiative forcing curve calculated directly from CH₄ emissions. However, after this initial period, both metrics progressively overestimate the radiative forcing of methane emissions from agriculture because they do not account for the decay of this greenhouse gas. The overestimation by GWP₂₀ is more pronounced due to the larger factor associated with methane compared to GWP₁₀₀ (refer to Table 5 for details). A very similar pattern emerges when these metrics are applied to calculate the CO₂-equivalence of N₂O emissions, with the only difference being that both GWP₁₀₀ and GWP₂₀ exhibit comparable overestimations in the long term since their factors for N₂O are nearly identical.

Newer metrics have therefore been recently proposed, such as the Linear Warming Equivalent (LWE) metric. This metric acts on the radiative forcing level of the chain of causality, advocating for an equivalence based on radiative forcing. As a result, in the scope of linear approximation, the radiative forcing from LWE-CO₂-equivalents provides an exact fit to the radiative forcing of a non-CO₂ forcer. The LWE-CO₂-equivalent radiative forcing and temperature curves cannot be seen in Figure 42 as they are exactly overlapped by the true curves calculated from the non-CO₂ emissions (green curves).

The GWP* metric, proposed before the LWE, offers an empirical approach to consider the decay of non-CO₂ GHGs by incorporating a stock and flow term in its equation:

$$E_{co_2-equiv.}^{GWP*} = \alpha E_{GHG} + \frac{\beta \Delta E_{GHG}}{\Delta t} \quad (57)$$

As shown in Figure 42, the radiative forcing curve calculated from GWP*-CO₂-equivalents of CH₄ closely follows the real radiative forcing curve (green curve), although it exhibits slight overreactions to discontinuous variations in methane emissions. However, the GWP* metric does not perform as well when creating CO₂-equivalences for N₂O emissions. This discrepancy is due to the parameters in Equation (57) being calibrated for methane. To better describe the behavior of nitrous oxide emissions, recalibration of these parameters will be performed at the end of this chapter.

B.1.3 GHGs contributions of the total agriculture climate impact: the impact of different equivalence metrics

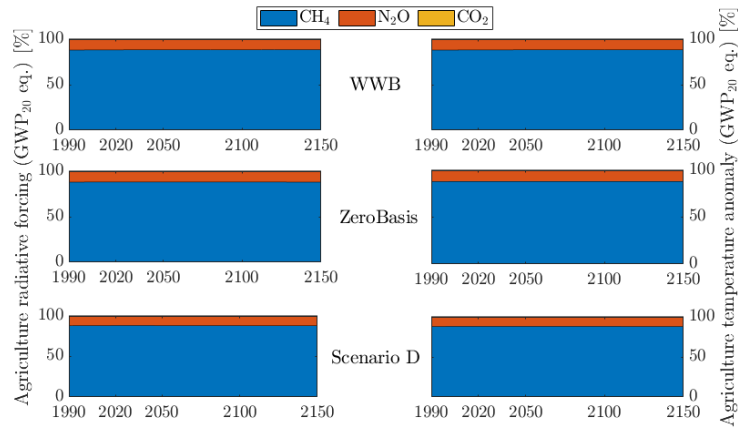
Figure 45 analyzes, of the total generated forcing and temperature perturbations from the Swiss agriculture activity since 1690, how much each greenhouse gas, namely CH₄, N₂O and CO₂, is responsible for of the total when different metrics are employed to calculate the CO₂-equivalent amounts for the non-CO₂ emissions. Results are shown for the GWP₂₀-, GWP₁₀₀- and GWP*-CO₂-equivalents. For the LWE-CO₂-equivalents results are not reported as they exactly correspond to the results of Figure 41, as the climate impact from LWE- CO₂-equivalents provides an exact fit to that of a non-CO₂ forcer.

Starting from the results of the GWP₂₀-CO₂-equivalents, Figure 45a, it can be observed that the contribution of methane to the total agriculture climate impact is greatly overestimated, as can be also seen from Figure 42, leading to an underestimation of the relative impact of N₂O. The overestimation of the impact of methane over that of nitrous oxide is reduced with the employment of GWP₁₀₀ and GWP* as equivalence metrics.

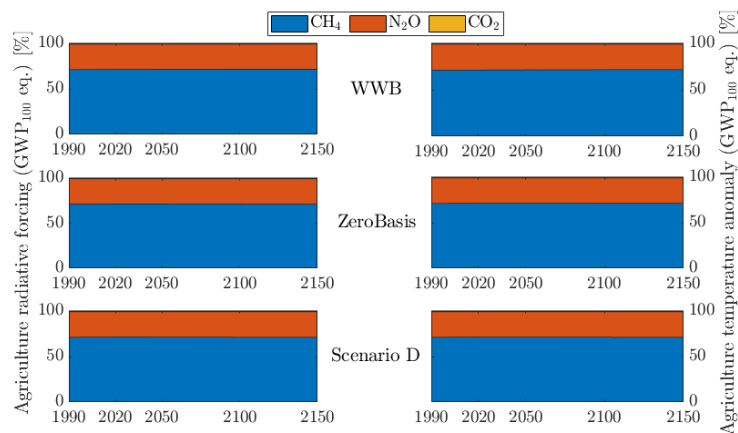
Nonetheless, when comparing Figure 45 with Figure 41, it can be clearly seen that all three metrics, namely GWP₂₀, GWP₁₀₀ and GWP*, fail to capture the temporal factor of N₂O, hence that its relative contribution to the total climate impact becomes larger with time as this long-lived climate forcer requires a longer time scale to reach stability as previously explained in Section 6.2.

CO₂-equivalents as calculated by means of GWP* are able to slightly express the temporal factor of N₂O,

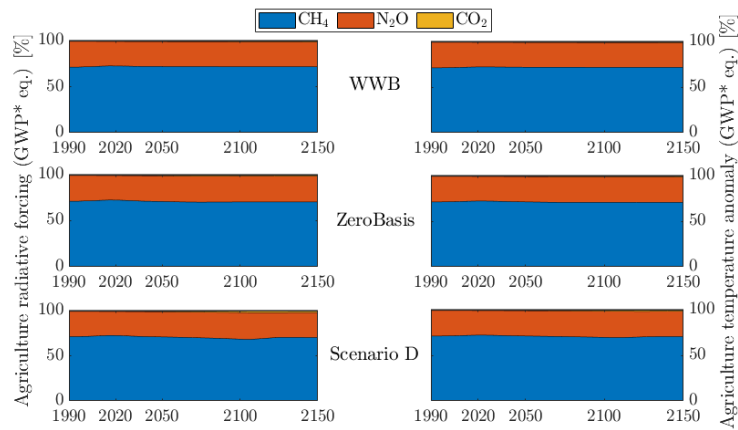
even though much more diminished compared to the real impact as calculated for the non-CO₂ emissions (Figure 41). The under-performance of GWP* when operating on emissions of N₂O, compared to when employed on emissions of CH₄, was already discussed in Section 6.2 and can be directly attributed to the fact that the parameters of the GWP* definition (Equation (57)) were calibrated on CH₄ and not on a longer-lived gas. Recalibration of the GWP* parameters to improve the metric performance when handling time series of N₂O will be discussed at the end of this chapter.



(a) GWP₂₀-CO₂-equivalents



(b) GWP₁₀₀-CO₂-equivalents



(c) GWP*-CO₂-equivalents

Figure 45. Percentage contribution of each greenhouse gas, namely CH₄, N₂O and CO₂, to the total generated forcing and temperature perturbations from the Swiss agriculture activity since 1690, as calculated in GWP₂₀-, GWP₁₀₀- and GWP*-CO₂-equivalents. The results for LW- and LW*-CO₂-equivalents are not reported as they exactly correspond to the results of Figure 41.

B.2 Aviation sector

B.2.1 From specific polluters to radiative forcing and temperature anomaly

Simulations of the radiative forcing and temperature anomaly resulting from CO₂, NO_x, SO_x, BC, and H₂O emissions originating from the Swiss aviation sector, as well as the climate impact of cirrus clouds, are presented in Figure 46.

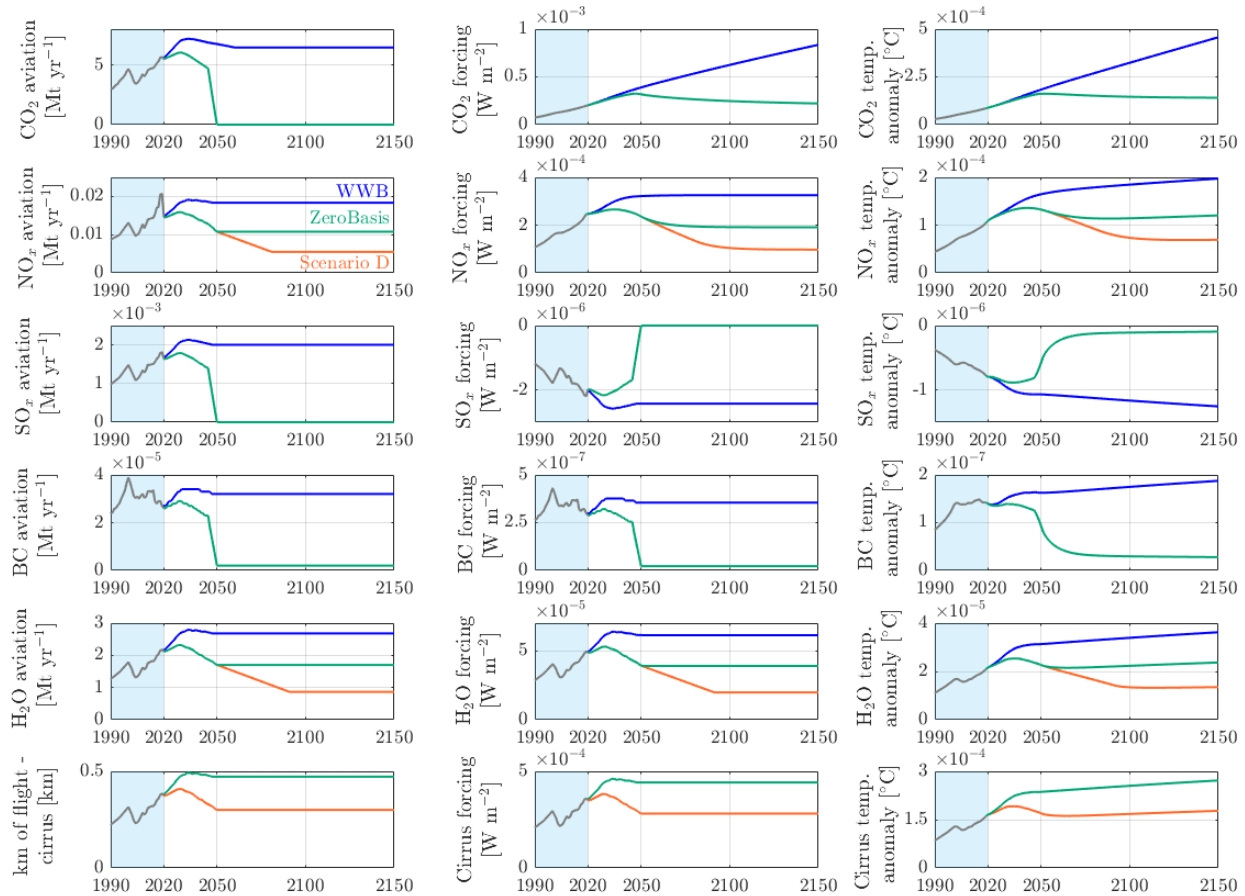


Figure 46. Emissions of CO₂, NO_x, SO_x, BC and H₂O, and kilometers of flight are shown in the first column from top to bottom, respectively. Their resulting radiative forcing is plotted in the second column, followed by the caused temperature anomaly in the third column. The three considered future scenarios, namely WWB, ZeroBasis and Scenario D, are shown in their respective colors, blue, green and orange. The curves are shown from 1990 to 2150.

Except for CO₂, all other pollutants emitted by aviation practices can be considered short-lived forcers. This can be clearly observed in Figure 46, where the radiative forcing and temperature anomaly of CO₂ continue to increase even as emissions decrease, whereas those of non-CO₂ pollutants follow the trends in emissions. Notably, in cases of a rapid reduction in CO₂ emissions, such as in the ZeroBasis scenario where emissions drop from 5 Mt/yr to 0 within 5 years (representing a 100% uptake of synthetic aviation fuels), the radiative forcing of carbon dioxide stabilizes from above. This is because, at that point, the only factor affecting the development of the CO₂ forcing is the exchange of a small portion of cumulative CO₂ from the atmosphere to other compartments. This exchange slightly reduces the atmospheric concentration of carbon dioxide and, consequently, the radiative forcing. This phenomenon, where thermal adjustment occurs when CO₂ emissions reach zero, balanced by ocean uptake of carbon dioxide, has been previously reported in the literature¹⁰.

As mentioned earlier, all other pollutants except CO₂ are short- to very short-lived, and their radiative forcing responds rapidly to changes in emissions, closely following their emission trends. SO_x, BC, H₂O, and cirrus clouds all have lifetimes of less than one day, which explains the almost instantaneous adaptation of radiative forcing to changes in their emissions. NO_x, with a lifetime similar to that of methane, experiences a slightly delayed adjustment in forcing perturbation.

Notably, emissions of SO_x have a cooling effect on the climate, leading to a negative radiative forcing. Consequently, in the ZeroBasis scenario where SO_x emissions are projected to decrease to zero due to the 100% uptake of synthetic aviation fuels (SAFs), the radiative forcing also approaches zero.

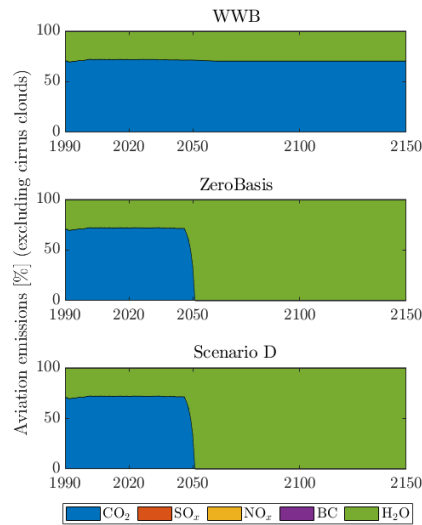
Turning to the temperature anomaly curves, it is evident that they take longer to stabilize compared to the corresponding radiative forcing perturbation curves. This slower stabilization of temperature can also be explained mathematically using Equation (32). The equation reveals that the radiative forcing's impact on surface temperature anomalies occurs on three different timescales: two relatively short timescales and a much longer timescale. The short timescales reflect the almost immediate impact of radiative forcing perturbations on the upper thermal layers' energy balance. In contrast, the longer timescale arises from the much slower transfer of excess heat to the deep ocean, which keeps the Earth's climate system out of equilibrium for an extended period after anthropogenic GHG emissions have altered radiative forcing.

Indeed, constant emissions of short-lived climate pollutants lead to an almost immediate generation of constant radiative forcing, as evident in the WWB (blue) case. However, the temperature anomaly takes longer to stabilize due to what can be described as an "inertia" of the lower thermal layer. This means that the temperature still needs to reach the steady state value corresponding to the final constant pollutants forcing level, which is a consequence of the evolution of the emissions, and therefore radiative forcing, that has been caused in the past (the mathematical expression of the steady state temperature anomaly is given by Equation (26)). Similarly, this pattern is observed in the ZeroBasis projections, with the exception of CO₂, BC, and SO_x, where the ZeroBasis projection resembles more of a scenario D projection. In these cases, the temperature initially decreases in response to the reduction in radiative forcing, but once this stabilizes, the temperature anomaly gradually starts to increase again, approaching the steady-state temperature corresponding to all past emissions. In the case of ZeroBasis, the plateau temperature is lower than that of the WWB projections due to the further reduction in emissions between 2020 and 2060. A similar behavior is witnessed for the orange Scenario D.

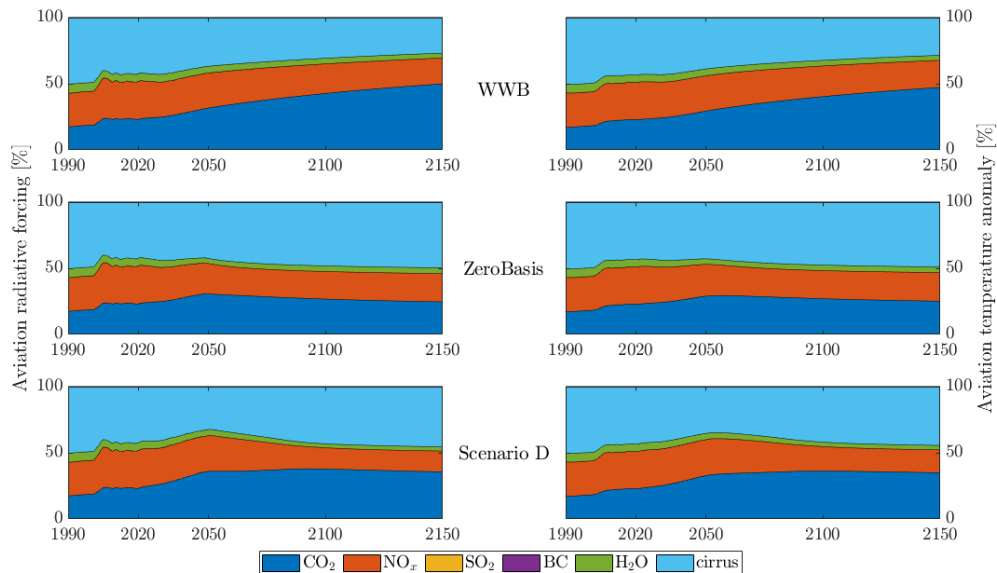
B.2.2 GHGs contributions of the total aviation climate impact

Figure 47 analyzes the total mass of GHGs emitted (excluding cirrus clouds), and of the total generated forcing and temperature perturbations (including the impact of cirrus clouds) from the Swiss aviation activity since 1950, and how much each polluter, namely CO₂, NO_x, SO_x, BC, H₂O and cirrus clouds, is responsible for of the total.

The analysis of the contribution of different pollutants to the climate impact of the Swiss aviation sector reveals that, in terms of the mass of total emissions, CO₂ and H₂O are the primary contributors. These pollutants are emitted in substantial quantities by aviation practices. However, when considering radiative forcing, which directly affects the climate impact, the primary contributors are CO₂, NO_x, and cirrus clouds. These pollutants have a significant impact on warming. The impact of H₂O and especially of SO_x and BC can be neglected.



(a) Contribution to the total mass of emissions (excluding cirrus clouds)



(b) Contribution to the total radiative forcing perturbation and temperature anomaly

Figure 47. Percentage contribution of each pollutant, namely CO₂, NO_x, SO_x, BC and H₂O, to the total mass of GHGs emitted, and the total generated forcing and temperature perturbations (including the impact from cirrus clouds formation) from the Swiss aviation activity since 1950. CO₂ is emitted in large quantities through the entire WWB scenario time line, while in the ZeroBasis case (equally as in Scenario D) CO₂ emissions are reduced to zero between 2045 and 2050 due to the projected 100% uptake of SAFs. In mass, water vapor is the only other significant pollutant. When looking at the total climate impact, CO₂ continuously increases in importance in the WWB case, due to the persisting emissions. Cirrus clouds and NO_x are the other two major pollutants impacting the climate. Their contribution goes from more than 75% in 1990 to approximately 50% in 2150 as CO₂ accumulates. In the ZeroBasis and Scenario D projections, the percentage contribution of CO₂ plateaus at less than 50% as emissions go to zero (the percentage contribution of CO₂ towards the total climate impact is higher in Scenario D because here, most other other non-CO₂ emissions are further reduced). In these scenarios of full SAFs uptake (within the 5 years before 2050), non-CO₂ pollutants consistently contribute most to the climate impact of the Swiss aviation sector between 1990 and 2150.

B.2.3 CO₂-equivalence metrics for non-CO₂ climate forcers: the effect on the radiative forcing and temperature anomaly

The non-CO₂ emissions of the Swiss aviation sector, and their corresponding climate impact, can also be calculated in terms of carbon dioxide, by means of equivalence metrics, namely the GWP₁₀₀, GWP₂₀, GWP* and LWE metrics.

Simulations of equivalent CO₂ emissions for NO_x, SO_x, black carbon and H₂O aviation emissions of the ZeroBasis scenario are shown in Figure 48, alongside simulations of the radiative forcing and temperature anomaly curves for the equivalent CO₂ amounts as calculated with the different metrics. The results for the WWB and Scenario D projections follow in Figure 49 and Figure 50.

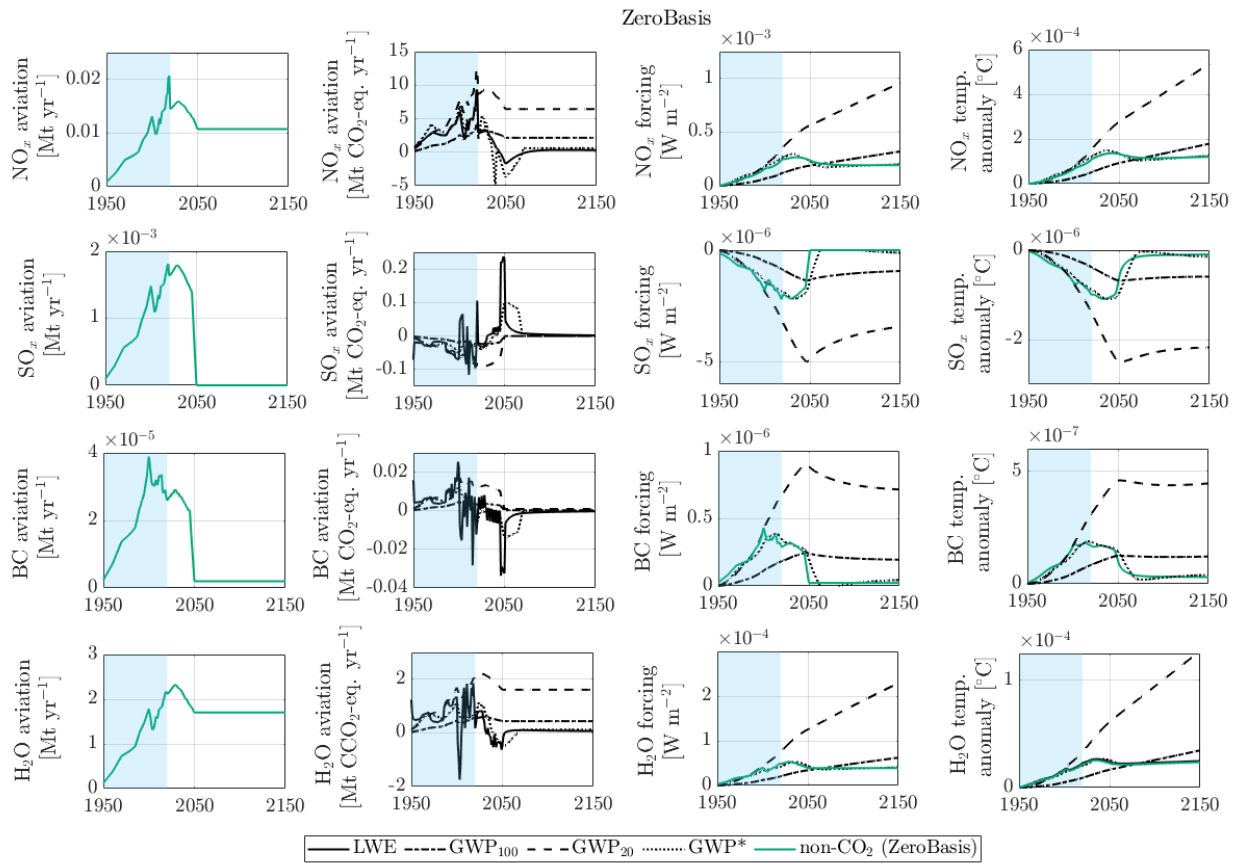


Figure 48. CO₂-equivalents, as calculated by means of the GWP₁₀₀, GWP₂₀, GWP* and LWE metrics, of NO_x (top row), SO_x, black carbon and H₂O (bottom row) emissions for the ZeroBasis scenario. The radiative forcing and temperature anomaly curves are calculated for the non-CO₂ emissions (green curves) and for the CO₂-equivalents as calculated with the different metrics. The climate impact calculated from LWE-CO₂-equivalents provides an exact fit to the impact of a non-CO₂ forcer. The GWP₁₀₀ and GWP₂₀ provide a correct equivalence at a specific point in time (i.e., around 20 and 100y years, respectively, from beginning of the time series analyzed). However they underestimate the required CO₂-equivalents before then, and greatly overestimate them thereafter, as they do not account for the decay of non-CO₂ GHGs. Lastly, the GWP* equivalence metric performs generally well as all investigated pollutants are short-lived.

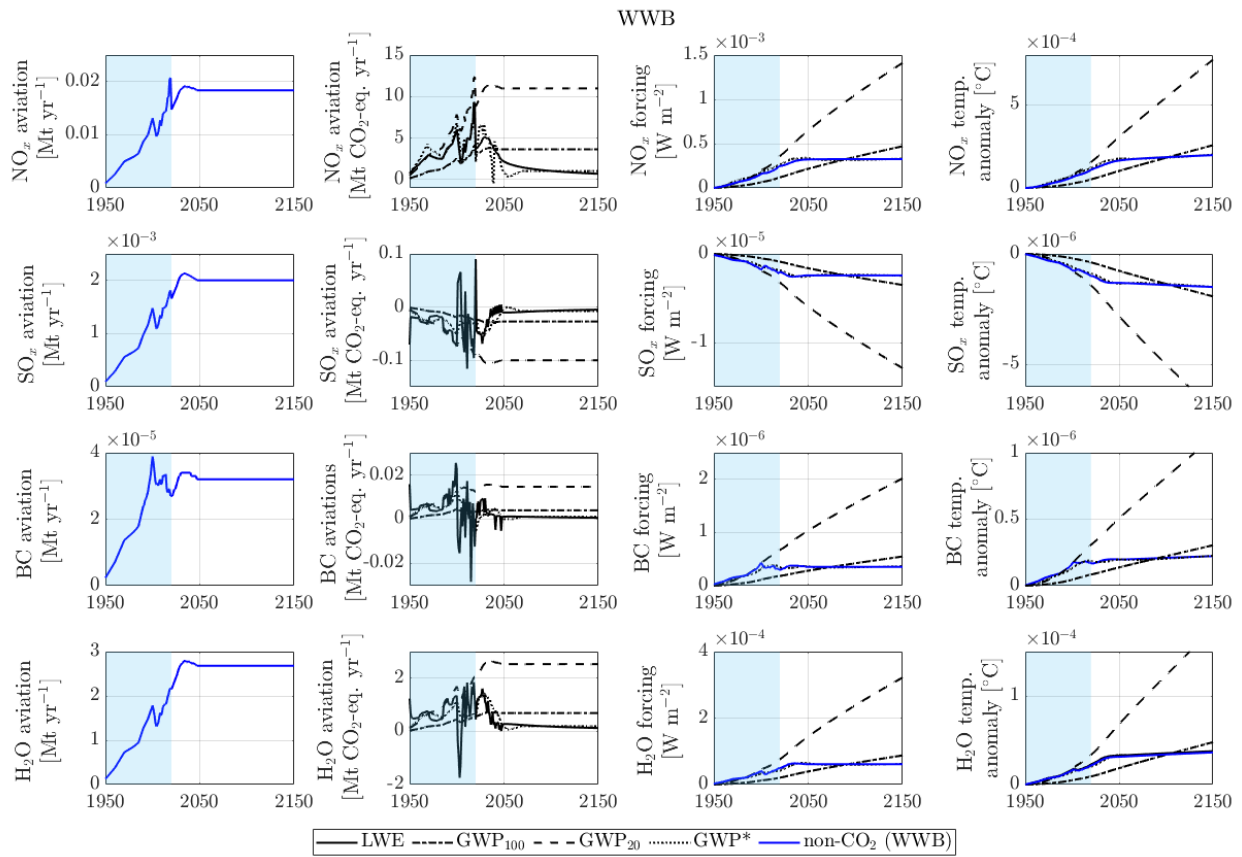


Figure 49. CO₂-equivalents, as calculated by means of the GWP₁₀₀, GWP₂₀, GWP* and LWE metrics, of NO_x (top row), SO_x, black carbon and H₂O (bottom row) emissions for the WWB scenario. The radiative forcing and temperature anomaly curves are calculated for the non-CO₂ emissions (blue curves) and for the CO₂-equivalents as calculated with the different metrics. The climate impact calculated from LWE-CO₂-equivalents provides an exact fit to the impact of a non-CO₂ forcer. The GWP₁₀₀ and GWP₂₀ provide a correct equivalence at a specific point in time (i.e., around 20 and 100y years, respectively, from beginning of the time series analyzed). However they underestimate the required CO₂-equivalents before then, and greatly overestimate them thereafter, as they do not account for the decay of non-CO₂ GHGs. Lastly, the GWP* equivalence metric performs generally well as all investigated pollutants are short-lived.

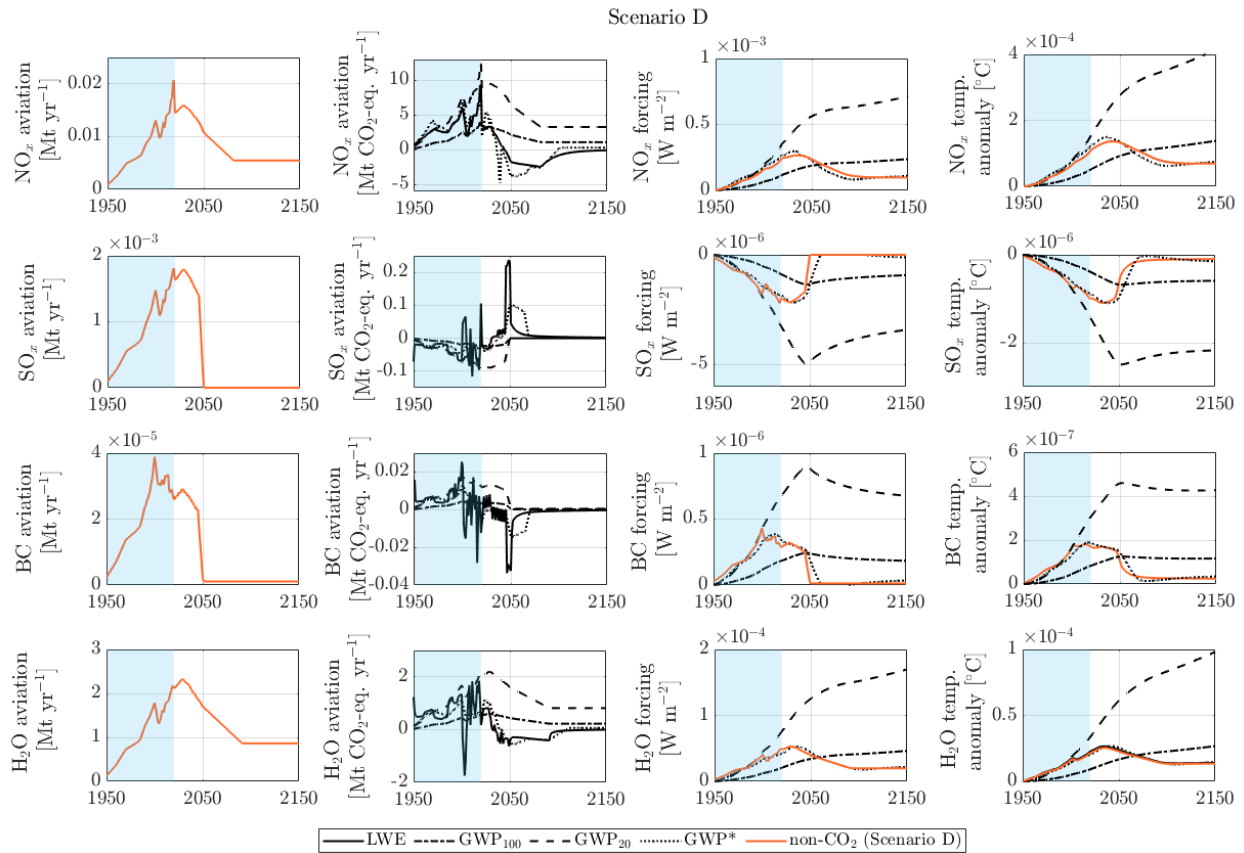


Figure 50. CO₂-equivalents, as calculated by means of the GWP₁₀₀, GWP₂₀, GWP* and LWE metrics, of NO_x (top row), SO_x, black carbon and H₂O (bottom row) emissions for Scenario D. The radiative forcing and temperature anomaly curves are calculated for the non-CO₂ emissions (orange curves) and for the CO₂-equivalents as calculated with the different metrics. The climate impact calculated from LWE-CO₂-equivalents provides an exact fit to the impact of a non-CO₂ forcer. The GWP₁₀₀ and GWP₂₀ provide a correct equivalence at a specific point in time (i.e., around 20 and 100y years, respectively, from beginning of the time series analyzed). However they underestimate the required CO₂-equivalents before then, and greatly overestimate them thereafter, as they do not account for the decay of non-CO₂ GHGs. Lastly, the GWP* equivalence metric performs generally well as all investigated pollutants are short-lived.

Emissions of NO_x, SO_x, black carbon, and H₂O for the ZeroBasis scenario are presented in the first column of Figure 48, and their corresponding radiative forcing and temperature anomaly are illustrated in green in the third and fourth column of the same figure, respectively. The second column provides emissions data in CO₂-equivalents, calculated using four equivalence metrics: GWP₁₀₀, GWP₂₀, GWP*, and LWE.

GWP₁₀₀ and GWP₂₀ are metrics that establish CO₂-equivalence for non-CO₂ climate forcers in a proportional manner. To determine equivalent CO₂ emissions, non-CO₂ climate forcer emissions are multiplied by their respective values of the chosen metric. The GWP₁₀₀ and GWP₂₀ values for NO_x, SO_x, black carbon, and H₂O were calculated using the equations provided in Appendix A, along with specific lifetime and radiative efficiency values for non-CO₂ flight emissions, as detailed in Table 6.

However, it's important to note that these metrics have recently been subject to criticism due to their non-physical nature. They fail to accurately capture the fundamental difference between the physical behavior of non-CO₂ and CO₂ climate forcers, namely that non-CO₂ forcers decay over time while CO₂ does not. While these metrics provide correct CO₂-equivalence at a specific point in time, they perform poorly when

applied to time series of emissions. Consequently, they do not ensure a proper equivalence in terms of climate impact, which could jeopardize the achievement of long-term climate goals.

The shortcomings of traditional metrics become evident when examining the radiative forcing and temperature anomaly curves derived from the calculated CO₂-equivalent emissions. In the case of all non-CO₂ climate forcers, both GWP₁₀₀-CO₂-equivalents and GWP₂₀-CO₂-equivalents initially (within the first approximately 100 and 20 years, respectively) underestimate the actual climate impact, as indicated by the green radiative forcing curve calculated from the non-CO₂ emissions. However, beyond this initial period, both metrics gradually begin to overestimate the radiative forcing generated by aviation emissions since they fail to account for the decay of these greenhouse gases. Notably, the overestimation is more pronounced with GWP₂₀ for short-lived GHGs like those from aviation compared to GWP₁₀₀. For emissions of black carbon (BC) and sulfur compounds (SO_x), the radiative forcing curves resulting from GWP₂₀-CO₂-equivalents exhibit a peak around 2050, followed by a decline as non-CO₂ emissions, and consequently CO₂-equivalent emissions, drop to zero in that year.

Recognizing the limitations of traditional metrics, newer approaches such as the Linear Warming Equivalent (LWE) metric have been proposed. LWE operates at the radiative forcing level of the causality chain, advocating for an equivalence based on radiative forcing. In a linear approximation, LWE-CO₂-equivalents provide an exact match to the radiative forcing of a non-CO₂ forcer. Notably, the LWE-CO₂-equivalent radiative forcing and temperature curves are indistinguishable from the true curves calculated from non-CO₂ emissions, as seen in Figure 48.

Another new metric is GWP*, which is an empirical equivalence metric that was proposed prior to the Linear Warming Equivalent (LWE) and aims to account for the decay of non-CO₂ GHGs through a stock and flow term, as depicted in Equation (57). As demonstrated in Figure 48, the radiative forcing curves of all non-CO₂ emissions, as calculated using GWP*-CO₂-equivalents, closely overlap with the actual radiative forcing curves (green curves). However, there is a slight tendency to overreact to abrupt variations in emissions. GWP* generally performs well with all non-CO₂ flight emissions because they are short-lived, aligning with the lifetime on which this equivalence metric was calibrated.

Furthermore, as discussed in Section 3.2.2, the radiative forcing of cirrus clouds is determined by parametrizing their radiative forcing in terms of kilometers of air traffic volume. Using the radiative forcing simulation, the LWE metric can be used inversely to calculate the amount of CO₂-equivalent emissions corresponding to the radiative forcing generated by cirrus clouds. The LWE-CO₂-equivalents of cirrus clouds resulting from Swiss aviation activities between 1950 and 2150 are depicted in Figure 51.

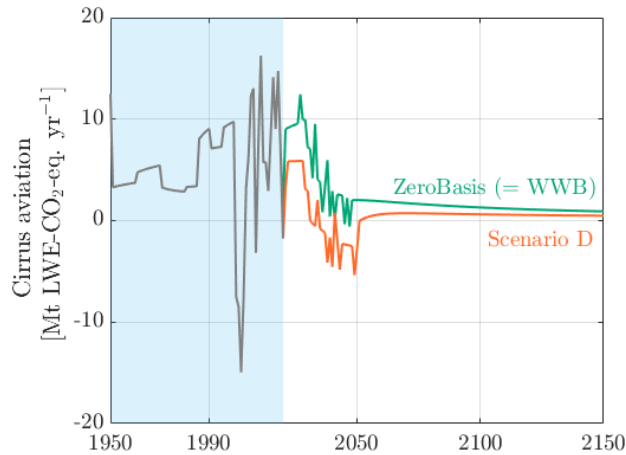


Figure 51. LWE-CO₂-equivalents of cirrus clouds induced forcing, as a result of Swiss aviation activity between 1950 and 2150.

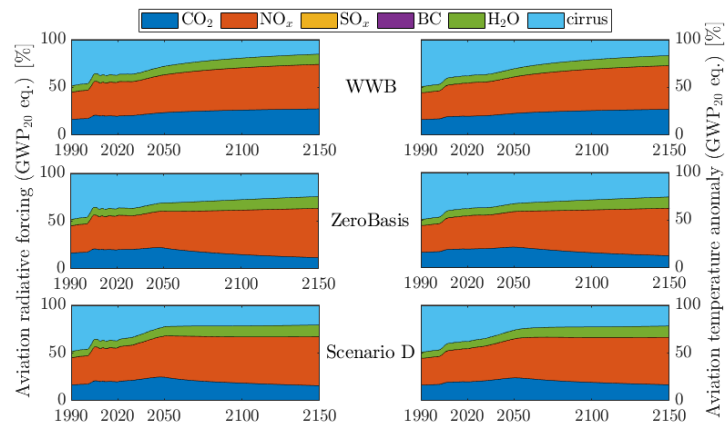
B.2.4 GHGs contributions of the total aviation climate impact: the impact of different equivalence metrics

Figure 52 provides an analysis of the total radiative forcing and temperature perturbations generated by Swiss aviation activity since 1950, showing the contributions of different climate forcers, including NO_x, SO_x, black carbon, H₂O, and cirrus clouds, when various metrics are used to calculate the CO₂-equivalent amounts for non-CO₂ emissions. The metrics considered are GWP₂₀, GWP₁₀₀, and GWP*. Results of the LWE-CO₂-equivalents are not reported as they exactly correspond to the results of Figure 47, as the climate impact from LWE-CO₂-equivalents provides an exact fit to that of a non-CO₂ forcer. Lastly, the forcing and temperature perturbation from the formation of cirrus clouds is not calculated with different metrics, as this is not possible, and is therefore equal in absolute values for all subplots of Figure 52.

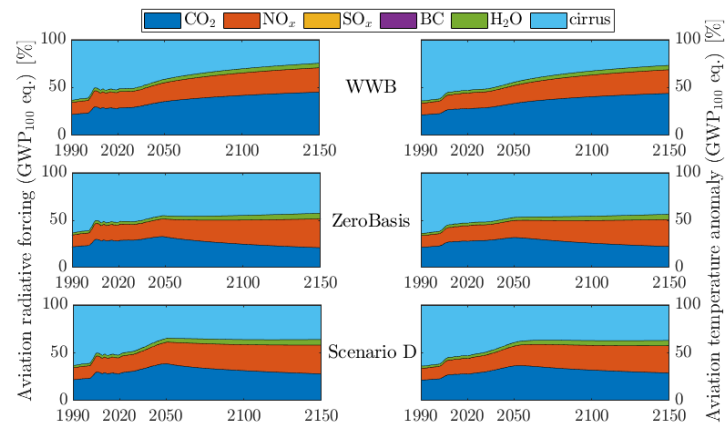
Starting with the GWP₂₀-CO₂-equivalents in Figure 52a, it is evident that the contributions of short-lived GHGs, such as NO_x and H₂O, are significantly overestimated throughout the entire timeline when compared to their real impact (as shown in Figure 47). This leads to a relative underestimation of the impact of CO₂ and cirrus clouds, particularly in the long term.

The results for GWP₁₀₀-CO₂-equivalents in Figure 52b exhibit behavior closer to the real climate impact (Figure 47). However, there is an initial underestimation of converted forcers like NO_x and H₂O until approximately 2050, followed by an increasing overestimation of their CO₂ equivalent thereafter. This overestimation, while present, is smaller than that observed with GWP₂₀-calculated CO₂-equivalents.

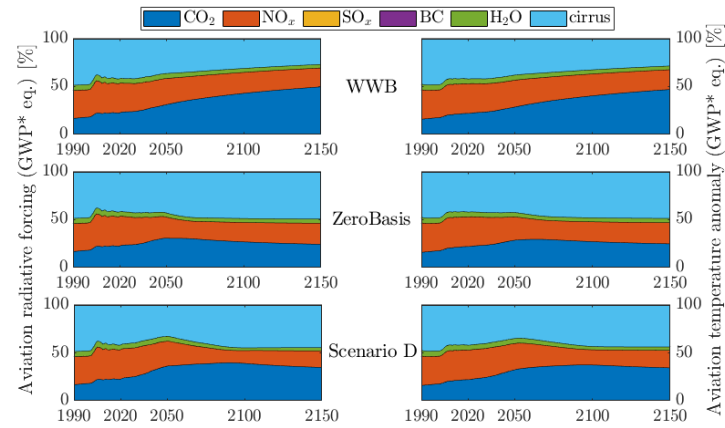
Lastly, Figure 52c shows the results for GWP*-CO₂-equivalents, which closely match the actual non-CO₂ results in Figure 47. GWP* appears to be a suitable metric for assessing the climate impact of aviation emissions in this context, as it provides a correct representation of the short-lived GHGs in accordance with the definition and calibration of the GWP* metric for such GHGs.



(a) GWP₂₀-CO₂-equivalents



(b) GWP₁₀₀-CO₂-equivalents



(c) GWP*-CO₂-equivalents

Figure 52. Percentage contribution of each climate forcer, namely NO_x, SO_x, black carbon, H₂O and cirrus clouds, to the total generated forcing and temperature perturbations from the Swiss aviation activity since 1950, as calculated in GWP₂₀-, GWP₁₀₀- and GWP*-CO₂-equivalents. The results for LWE-CO₂-equivalents are not reported as they exactly correspond to the results of Figure 47. Forcing and temperature perturbation from the formation of cirrus clouds is not calculated with different metrics, as this is not possible, and is therefore equal in absolute values for all plots.

B.3 Consideration of the climate impact from a time point t^*

To enable a clearer and more transparent understanding, simple profiles of steadily increasing, decreasing and constant GHG emissions are analyzed first. From these simplified outlines we can derive some key observations, as discussed in this section.

In all cases, the concentration is calculated through a convolution integral of the emissions, and then the radiative forcing is calculated as linearized approximation of $F_i = f_i(c_i)$.

The total radiative forcing differential of the specific agent, and hence its overall climate impact, is that generated by all emissions since the first time point of anthropogenic climate-negative activities, set as $t = 0$.

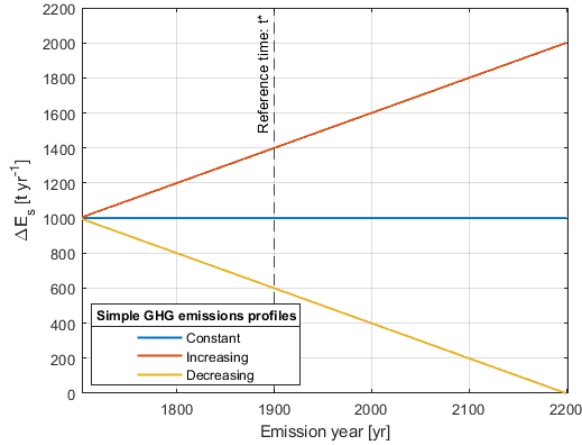


Figure 53. Three linear emissions profiles (increasing, decreasing and constant) of a generic GHG.

Figure 53 exhibits the emissions of a specific agent, considered as a relatively small perturbation of the background, $E_s(t)$, for a generic greenhouse gas, over a time span from 1700 to 2200.

The total radiative forcing differential for the three cases above could be calculated by means of Equation (14), accounting for all emissions over the time span 1700-2200, where 1700 is considered as the starting point of emissions.

B.3.1 Approaches (CASES)

As previously introduced by Equation (13), the evolution of a climate forcer concentration can be expressed as follows:

$$\begin{aligned}
 c_i(t) &= c_{i,0} \exp\left(-\frac{t}{\tau_i}\right) + \int_0^t (E_{i,g}(t') + E_{i,s}(t')) \exp\left(\frac{t' - t}{\tau_i}\right) dt' = \\
 &= c_{i,0} \exp\left(-\frac{t}{\tau_i}\right) + \int_0^t E_{i,g}(t') \exp\left(\frac{t' - t}{\tau_i}\right) dt' + \int_0^t E_{i,s}(t') \exp\left(\frac{t' - t}{\tau_i}\right) dt' = \\
 &= c_{i,g}(t) + \Delta c_{i,s}(t) \qquad t \geq 0 \qquad (58)
 \end{aligned}$$

where $\Delta c_{i,s}$ is the differential perturbation of the atmospheric climate forcer's concentration due to specific emissions.

In the scope of climate policy, however, it might be of interest to consider the climate impact of a specific emitter only from a reference time point t^* , where $t \geq t^* \geq 0$. The consideration of only a time subset in the evaluation of the forcing of a specific agent can be achieved by means of three different approaches, as discussed below and illustrated in Figure 54.

CASE 1

The differential concentration is calculated as a difference between the concentration at t and that at a reference time t^* . This is obtained by subtracting such reference value to Equation (13), thus obtaining:

$$\Delta c_{i,s}^*(t) = \Delta c_{i,s}(t) - \Delta c_{i,s}(t^*) \quad (59)$$

Effectively, the atmospheric differential concentration perturbation curve from $0 \leq t \leq t^*$ is now part of the background. Equation (59) applies to the case of a general non-CO₂ CFI, while a similar expression can be derived for carbon dioxide.

CASE 2

The differential concentration is calculated based on all specific emissions from $t = t^*$, i.e., from a reference time, chosen based either on considerations about climate change (i.e., climate change was either not yet an issue or not yet perceived as a problem) or on climate policy decisions (e.g., because international covenants set that as the point in time where climate policies are initiated), thus obtaining:

$$\Delta c_{i,s}^*(t) = \exp\left(\frac{-t}{\tau_i}\right) \int_{t^*}^t \Delta E_{i,s}(t') \exp\left(\frac{t'}{\tau_i}\right) dt' \quad (60)$$

Effectively, emissions from $0 \leq t \leq t^*$ are considered as part of the background and the specific agent is assumed to start emitting from $t = t^*$.

CASE 3

The differential concentration is calculated based on all specific emissions from $t = t^*$, reduced by a reference value, which is typically set equal to the value of the specific emissions at $t = t^*$, i.e., $E_{i,s,\text{ref}} = E_{i,s}(t^*)$, thus obtaining:

$$\Delta c_{i,s}^*(t) = \exp\left(\frac{-t}{\tau_i}\right) \int_{t^*}^t [\Delta E_{i,s}(t') - \Delta E_{i,s,\text{ref}}] \exp\left(\frac{t'}{\tau_i}\right) dt' \quad (61)$$

Effectively, this means that we consider the emissions level at the time t^* as the "business-as-usual" scenario to which we relate the emissions after that time point.

It is worth noting that in the constant emissions case, from the last equation, if $E_{i,s,\text{ref}} = E_{i,s}(t^*)$, then the differential concentration is zero, which represents obviously the limit value for $t \rightarrow \infty$.

Figure 54 summarizes the three different cases of how to evaluate the climate impact of a specific sector or agent from a time point t^* .

In the first row, plots showing the emissions perturbation curves, as taken into consideration for the calculations of the radiative forcing differentials from a time t^* , are presented. It is worth noticing that for CASE 1 we only consider the variation in atmospheric differential concentration perturbation of the pollutant from a time t^* . The three rows below exhibit the radiative forcing from $t = 0$ (dashed line) and from $t = t^*$ (solid line) for the three different emission profiles (increasing, decreasing and constant), and for three different CFs, respectively: the short-lived CH₄, the long-lived N₂O and the accumulating CO₂.

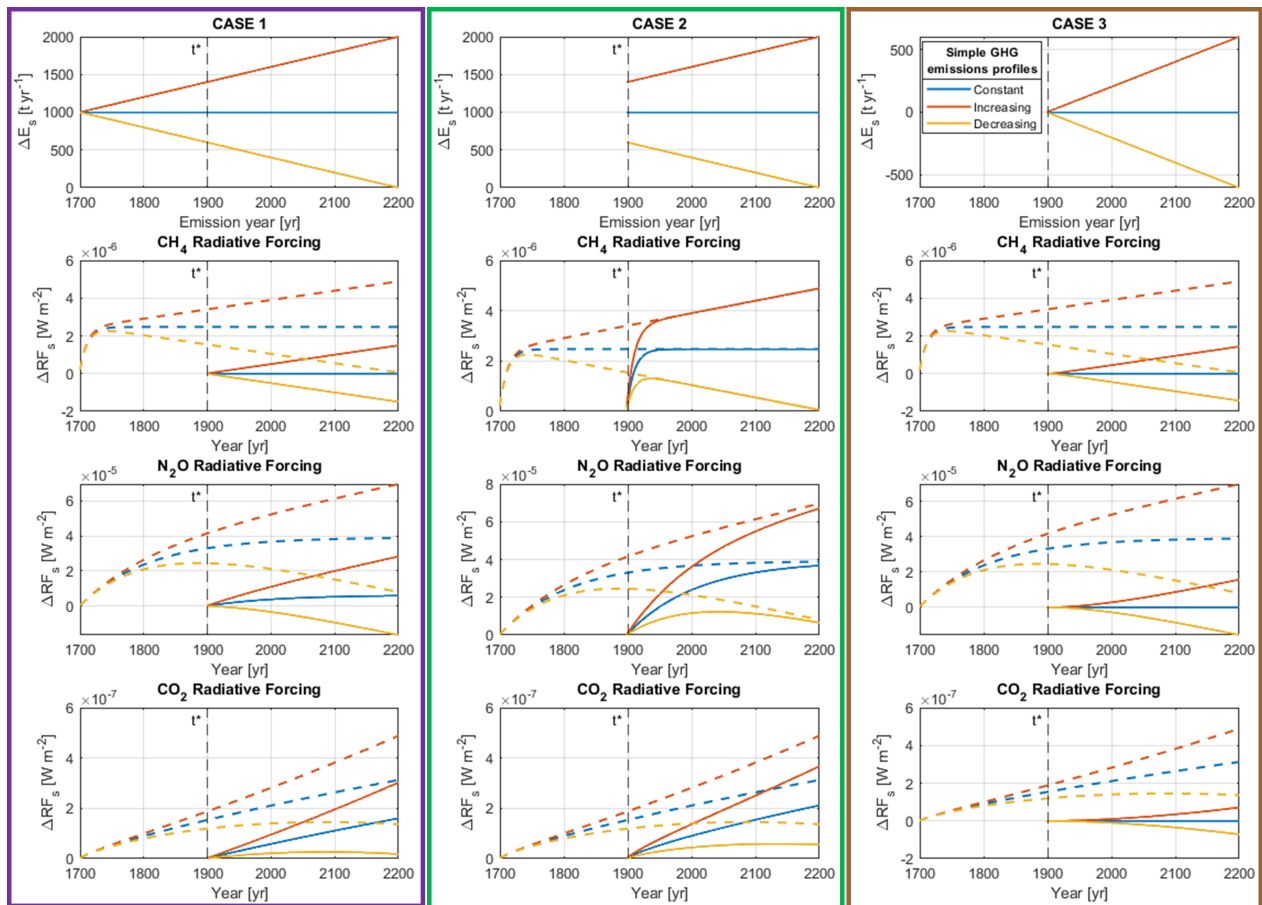


Figure 54. Three approaches for the evaluation of a specific agent’s climate impact from a reference time point t^* : CASE 1, highlighted in purple, CASE 2, in green, and CASE 3, contoured in brown. The total radiative forcing differential curves, exhibiting the climate impact of a specific agent as a result of all the emissions from $t = 0$, are shown with dashed lines. The solid lines exhibit the partial radiative forcing differential, or climate impact, of a specific emitter when considering their ”activity” only from a time t^* , as calculated with the different approaches (CASE 1, 2 and 3). The colors indicate the emissions profile, as specified in Figure 53.

From a climate perspective the most accurate mitigation effect would come from considering all emissions since $t = 0$, hence from the beginning of the anthropogenic climate-negative activity of the specific agent (correspondent to the dashed lines of Figure 54). These curves show increasing climate impact for all climate forcers (i.e., CH_4 , N_2O and CO_2) in the case of an increasing emission profile. For constant emissions of CH_4 and N_2O , the generated radiative forcing differential stabilizes to a constant value on a shorter and longer timescale, respectively, as a result of their different life times. For constant CO_2 emissions, the resulting radiative forcing, and hence climate impact, continuously increases due to the cumulative nature of this pollutant. Lastly, for decreasing emissions of CH_4 and N_2O , the resulting RF curves decrease after having peaked. The time of this peak depends on the life time of the pollutant. Instead, decreasing emissions of CO_2 are responsible for a continuously increasing radiative forcing differential. Once the emissions become zero and maintain that level for a sustained time, the radiative forcing curve reaches a steady state corresponding to the level of carbon dioxide concentration accumulated in the atmosphere.

As previously mentioned, the goal of a climate policy, might be however to only mitigate the emissions from a certain time point, either in the past or in the future. Evaluating the climate impact of a specific agent from a time point t^* leads, however, to different results depending on the mathematical approach (CASE) followed.

When employing CASE 1, the climate impacts of a specific emitter are considered as starting from t^* . From that point onward, the specific radiative forcing differential due to non-CO₂ GHG emissions increases and decreases for rising and lowering emissions profiles, respectively. For constant emissions, the radiative forcing profile from a time t^* depends on the type of non-CO₂ GHG. If $t^* \gg \tau_i$, such as for the case of CH₄ in Figure 54, the radiative forcing differential from t^* remains stable and equal to 0, as the total concentration differential had already reached a steady state before t^* . If $t^* \ll \tau_i$, as exhibited in the case of the longer-lived N₂O climate forcer, ΔRF_s from t^* slightly increases reaching a steady state over a longer time horizon. As previously mentioned, the radiative forcing differential keeps increasing for constant CO₂ emissions, while decreasing emissions approaching zero result in a positive and constant ΔRF_s on a long time scale. These behaviors remain true when only looking at the climate impact from a time t^* . Worth highlighting is that the radiative forcing differential curves from a time t^* , as calculated by the mathematical approach of CASE 1, still consider, to an extent dependent on the lifetime of the evaluated GHG, some of the climate effect due to emissions that occurred prior to t^* .

In CASE 3, instead, only the additional emissions from a time t^* and relatively to that level, which becomes a sort of "business-as-usual" reference, are considered. For increasing, decreasing and constant emissions, all forcings exhibit a similar radiative forcing behavior, independently of their life time. For increasing and decreasing emissions, relative to the value at t^* , the radiative forcing differential increases and decreases, respectively. For constant emissions, the additional radiative forcing since t^* remains steady at 0 as we are neither emitting more nor less relatively to our "business-as-usual". Important to highlight, is that utilizing the mathematical approach presented in CASE 3 results in a strongly different climate impact for CO₂ compared to CASE 1 (and CASE 2, as we will see next). In fact, considering the effect of CO₂ from a time t^* with the approach of CASE 3 leads to the conclusion that constant and decreasing emissions of CO₂ have a neutral and even positive climate impact, respectively. These interpretations are nonetheless incongruous with the known physical cumulative nature of carbon dioxide in the atmosphere.

Lastly, following the approach of CASE 2 we consider the emissions of a specific agent as only starting from time t^* . For short-lived CFs such as CH₄, all three profiles of emissions exhibit a specific climate impact from t^* that overlaps with the total radiative efficiency differential within a relatively short time frame. The same behavior is observed for N₂O but the overlap is reached over a longer time scale. For a CO₂ emissions profile, the curve depicting the total climate impact and that of the radiative forcing from a time t^* achieve a steady state over time, but remain distant by a constant amount which corresponds to the atmosphere-accumulated fraction of CO₂ emissions from the initial time to t^* .

Worth noting is that even if, for the case of the short-lived CH₄ where the radiative forcings calculated starting from t^* with CASE 2 quickly overlaps with the total radiative forcing curves, the mathematical artifact of the quickly raising concentration, and hence forcing, after t^* has an effect on the behavior of the corresponding temperature curves for a long time after t^* , again as a result of the longer time scale required by the surface temperature anomaly to stabilize after a perturbation in the radiative forcing.

Lastly, it is again important to highlight that the most accurate evaluation of the radiative forcing and temperature anomaly curves is achieved when considering all emissions since $t = 0$, hence from the beginning of the anthropogenic climate-negative activity of a specific agent (e.g. around the beginning of 1700 for the Swiss agriculture sector).

In Figure 55 the different CO₂-equivalence metrics are evaluated for the simple profiles of increasing, decreasing and constant emissions as presented in Figure 53. Similar conclusions on the performance of the different equivalence metrics are drawn as in Appendix B.1.2.

The first row of Figure 55 exhibits the CO₂-equivalent profiles as given by the LWE and GWP* metrics, for methane in black and nitrous oxide in red (for easiness of graph reading the GWP₁₀₀- and GWP₁₀₀-CO₂-

equivalent profiles are not given as they simply proportional to those of the non-CO₂ emissions). The second and third rows show instead the equivalent radiative forcing as calculated with the GWP₂₀, GWP₁₀₀, GWP* and LWE metrics, for CH₄ and N₂O, respectively.

From the second and third rows of Figure 55 it is possible to see that the GWP₂₀ and GWP₁₀₀ metrics result in a quite incongruous equivalent radiative forcing, compared to the real curve (solid line), for both CH₄ and N₂O. In fact, these two metrics calculate equivalent emissions as a proportionality of the real non-CO₂ emission profiles presented in blue in the first row of Figure 55, which results in a long-term overestimation of the CO₂-equivalent radiative forcing calculations. More importantly, it is worth noticing that, for SLCFs, the GWP₁₀₀ metric results in an underestimation of the climate impact, and hence required Carbon Dioxide Removal (CDR), on a short-term. Given that the time of peak warming is unknown, any metric that results in higher global temperatures on any timescale risks compromising the achievement of the long-term temperature goal.

Equivalent radiative forcing as calculated by the GWP* metric exhibits a good approximation to the true climate impact of SLCFs, while it underestimates overtime the warming generated by LLCFs. This behaviour is a direct consequence of the mathematical definition of GWP*, as it was trained and calibrated to describe the behavior of methane.

Lastly, Linear Warming Equivalence results in an exact representation of the true radiative forcing of a non-CO₂ CF.

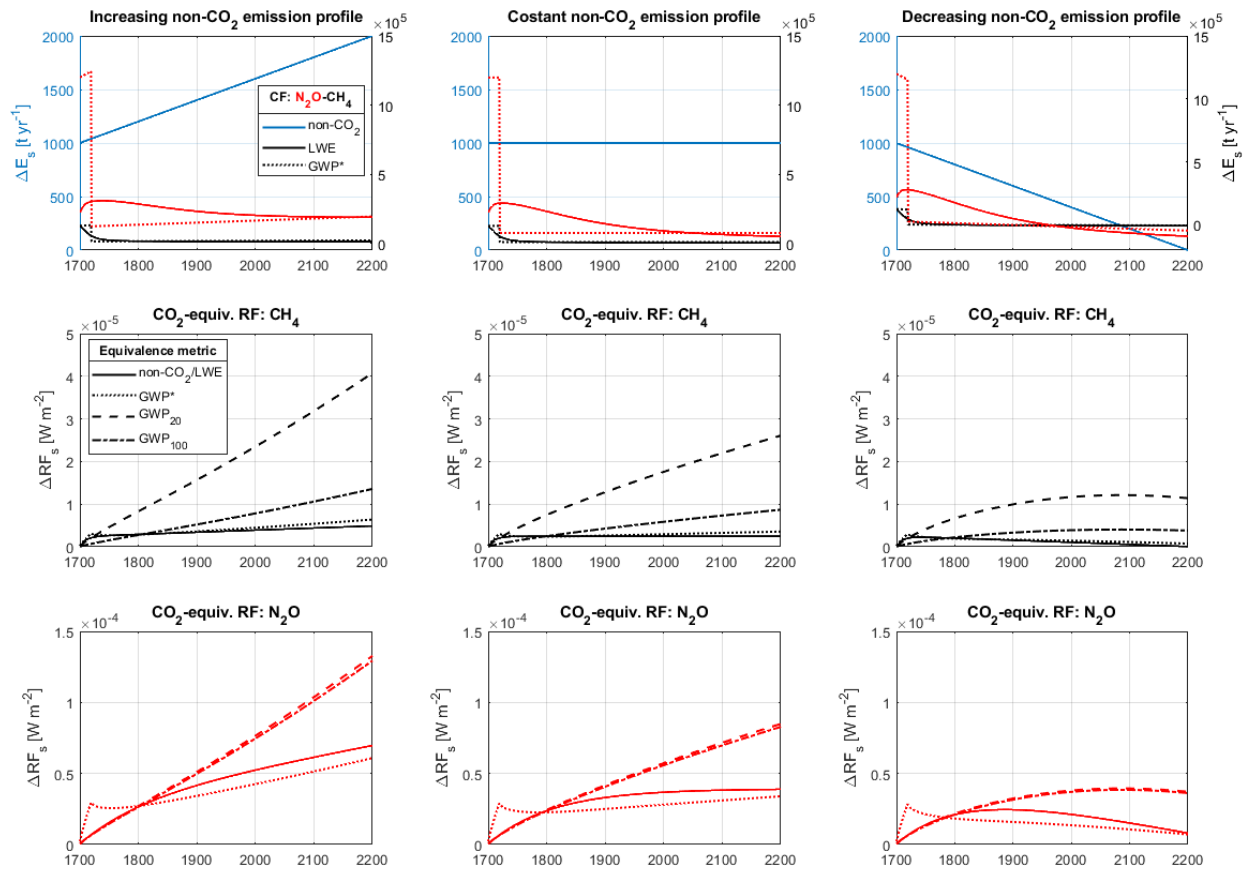


Figure 55. Evaluation of different CO₂-equivalence metrics for the simple profiles of increasing, decreasing and constant emissions as presented in Figure 53. The first row exhibits the equivalent profiles as given by the LWL and GWP* metrics, for methane in black and nitrous oxide in red. The second and third rows show the equivalent radiative forcing as calculated with the GWP₂₀, GWP₁₀₀, GWP* and LWL, for CH₄ and N₂O, respectively.

B.3.2 Simulation of the Swiss agriculture climate impact from a time t^*

In this section we analyze the example of the Swiss agriculture sector and how its climate impact varies when considering only emissions from a time t^* , by means of the 3 CASES introduced in the above section.

Two different reference time points, t^* , were investigated besides 1690 ($t=0$, considered as the beginning of Swiss agriculture emissions, hence the pre-industrial level or beginning of the anthropogenic climate-negative activity from the Swiss agricultural sector) namely 1950, a time point in the middle of the increase in emissions, and 1990, the peaking point of Swiss agriculture emissions and corresponding also to the time of increasing societal concerns about global warming (e.g., establishment of the Intergovernmental Panel on Climate Change, IPCC).

Emissions profiles for CH₄, N₂O and CO₂ from the agriculture sector are reported in the rows of Figure 56 from 1690 to 2100 (in black). Emissions considered only from later reference time points, namely 1950 (in red) and 1990 (in blue), are exhibited for CASE 2 (green box) and CASE 3 (brown box) as calculated by following their respective mathematical approaches. CASE 1 (purple box) considers instead the additional atmospheric concentration relative to either 1950 or 1990, rather than "acting" on the emissions themselves. For this reason, the first column of Figure 56 does not exhibit red or blue emission profiles. Lastly, future projections on the evolution of GHGs emissions are highlighted by a white figure background and differentiated

with different line styles, namely dash-dotted for the WWB scenario, solid for the ZeroBasis and dashed for the Scenario D projection.

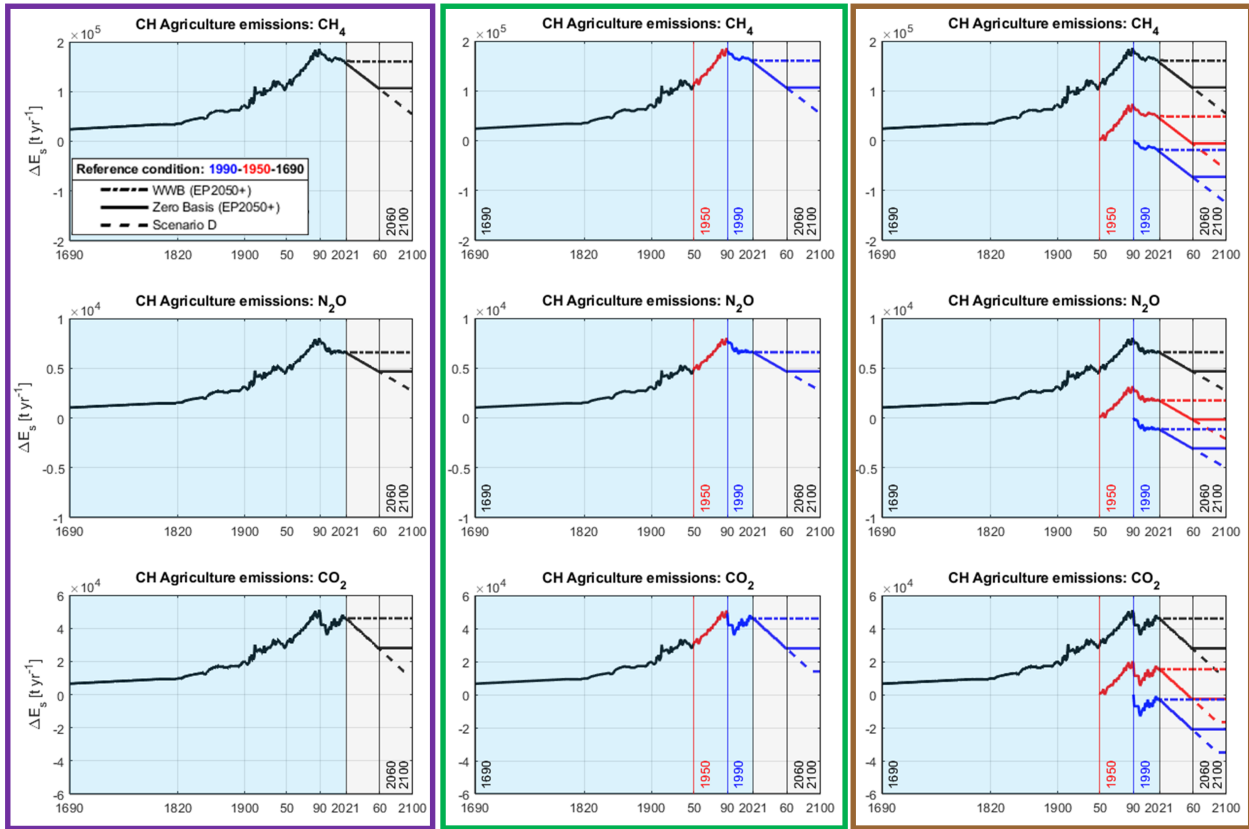


Figure 56. Swiss agriculture CH₄ (first row), N₂O (second row) and CO₂ (last row) emission profiles from 1690 to 2100 (in black). For CASE 2 (green box) and 3 (brown box), emission profiles from 1950 to 2100 (in red) and from 1990 to 2100 (in blue) are exhibited, each calculated following the respective different mathematical approaches.

The effect of the different emission profiles on the current radiative forcing differential is simulated and exhibited in Figure 57. The three black curves, resulting from the emission profiles of CH₄, N₂O and CO₂, respectively, represent the real impact of the Swiss agriculture sector on the climate since the beginning of its activity. These black radiative forcing profiles correspond to the ones of Figure 5, previously discussed in Section 6.2.

However, if the objective is to evaluate the Swiss agriculture’s climate impact only from a later time point than 1690, the three previously explained approaches (CASE 1, 2 and 3) can be utilized.

Considering only the additional relative atmospheric concentration, as done in CASE 1, leads to positive increasing radiative forcing differential curves for both reference times (i.e., 1950 and 1990) in the case of N₂O and CO₂. For these GHGs, the current radiative forcing levels when considering 1950 and 1990 as the reference time points are approximately half and one fifth, respectively, of the values resulting from considering the entire profile (black curve). For methane, considering only the relative concentration differential since 1950 results in a positive radiative forcing. However, if only the agriculture impact from 1990 is assessed, the radiative forcing differential due to methane would, already today, reach negative values, indicating a positive climate impact with respect to the 1990 reference year.

Considering, instead, agriculture emissions as starting from 1950 or 1990, as done in CASE 2, leads to the curves framed in green. For methane, the red curve quickly rises, reaching an overlap with the black RF differential on the time scale of 40-50 years. This sharp increase in forcing in the years immediately after t^* is an artifact of the mathematical approach considered in CASE 2 (??), while the red and black curves overlapping effectively means that, following the mathematical approach of CASE 2, emissions prior to 1950 stop playing a significant role on the radiative forcing of the '90s and later dates. The same behavior can be extrapolated for the blue curve, where emissions from 1990 stop having a forcing effect in approximately the 2030s (as depicted in ??). This overlapping behavior is true, even if on a much longer time scale, for N_2O , as previously exhibited in Figure 54. For CO_2 , when considering agriculture emissions as starting from either 1950 or 1990, the simulations lead to positive and increasing RF curves. As a result of the chosen mathematical approach (CASE 2), these curves will never decrease, but rather only plateau in case of persistent zero emissions. This finding is consistent with the known physical cumulative nature of CO_2 in the atmosphere.

It is important to remember that the surface temperature evolution occurs on a much longer timescale than that of the radiative forcing, as previously indicated Section 6.2. Therefore, the sharp increase in forcing in the years immediately after t^* , which is an artifact of the mathematical approach considered in CASE 2 (??), is felt in the evolution of the temperature anomaly for multiple centuries, effectively also changing the warming evolution from that of the black forcing curves.

In CASE 3, only the emissions after the "business-as-usual" year, and relative to that reference value, are considered. For all GHGs, the simulated red RF curves remain of positive value in 2021 as the emissions of that year are still greater than those of 1950. Instead, the blue radiative forcing curves exhibit a positive climate impact already today for CH_4 , N_2O and CO_2 alike. It is important to notice that this is a consequence of the mathematical approach followed, but is not representative of the physical behavior of long-lived GHGs and, especially, of CO_2 .

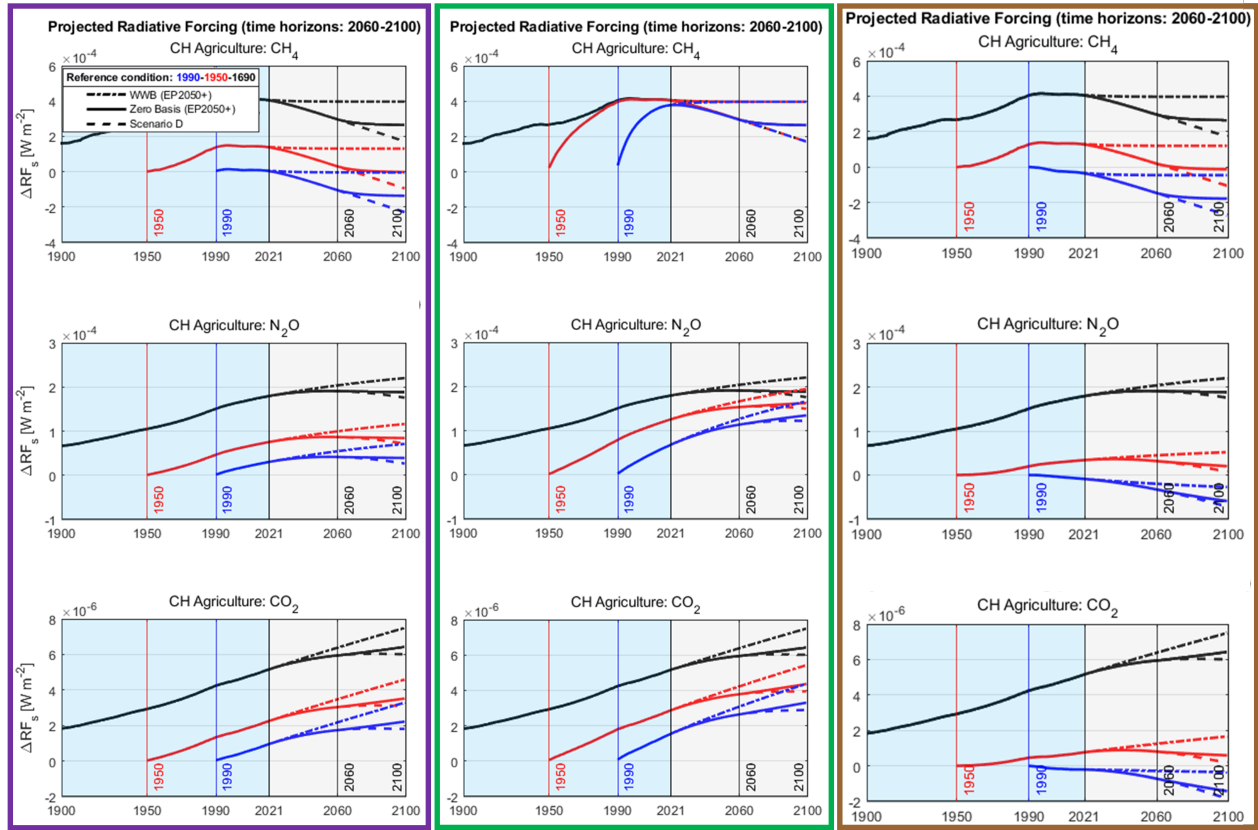


Figure 57. Radiative forcing evolution due to CH₄ (first row), N₂O (second row) and CO₂ (last row) emissions from 1690 to 2021 (in black), as well as the climate impact of the Swiss agricultural sector when a later reference year is considered (i.e., 1950, in red, and 1990, in blue), as the result of different mathematical approaches (i.e., CASE 1, framed in purple, CASE 2, in green, and CASE 3 in brown).

B.4 GWP* parameters calibration to describe LLCFs

As introduced and explained in previous literature^{12,32} and reported in Appendix A.2, CO₂-equivalent emissions following the GWP* metric are calculated using the following relationship:

$$E_{\text{CO}_2\text{we}} = g\text{GWP}_H \left(r \frac{\Delta E_{\text{SLCP}}}{\Delta t} H + s E_{\text{SLCP}} \right) \quad (62)$$

where CO₂we stands for CO₂-warming-equivalent, ΔE_{SLCP} the change in SLCP emission rate over the preceding Δt years, E_{SLCP} the SLCP emissions for that year, and r and s the weights assigned to the rate and stock contributions, respectively, with the constraint that $r + s = 1$.

All these GWP* parameters were calibrated to optimally describe the forcing generated by short-lived climate pollutants, more specifically methane, and do not perform well in generating an equivalence that represents the radiative forcing of a long-lived forcer such as nitrous oxide. Therefore, we set here to reconsider the standard parameters of the GWP* definition to try and improve the performance of this equivalence metric for LLCFs. Typically, GWP* is computed with the following parameter values: $\Delta t = 20$ yr, $H = 100$ yr, $g = 1.13$, $r = 0.75$ and $s = 0.25$. A sensitivity analysis was conducted in this study to improve the fit provided by GWP* equivalences when describing LLCFs. In this scope, the following values were analyzed for each parameter, as reported by Table 7.

Table 7. GWP* calibration of parameters to describe LLCFs.

	Values assessed	Selected final value
H [yr]	20, 100	100
Δt [yr]	20, 50, 100, 150, 220	150
r [-]	0 to 1, in 0.1 steps	0.6

An optimized fit of GWP* equivalences to the climate impact of LLCFs was found for the following calibration: $\Delta t = 150$ yr, $H = 100$ yr and $r = 0.6$. The s parameter is found by subtracting r from unity, hence $s = 1 - r = 0.4$, and g is a function of s as introduced by Smith *et al.*³²:

$$g(s) = \frac{1 - \exp\left(\frac{-s}{1-s}\right)}{s} = 1.22 \quad (63)$$

Figure 58 exhibits the true radiative forcing of N_2O emissions (black solid line), from the WWB scenario of the Swiss agriculture sector, compared with the CO_2 -equivalences as calculated by the "original" GWP* (blue dashed line) and the GWP* calibrated to better express LLCFs (orange dashed line).

Tuning of the GWP* mathematical expression with the new selected parameters values clearly improves the ability of this equivalence metric to describe the radiative forcing curves of long-lived climate forcers, such as N_2O , by reducing the overreacting behavior associated with the original metric calibration.

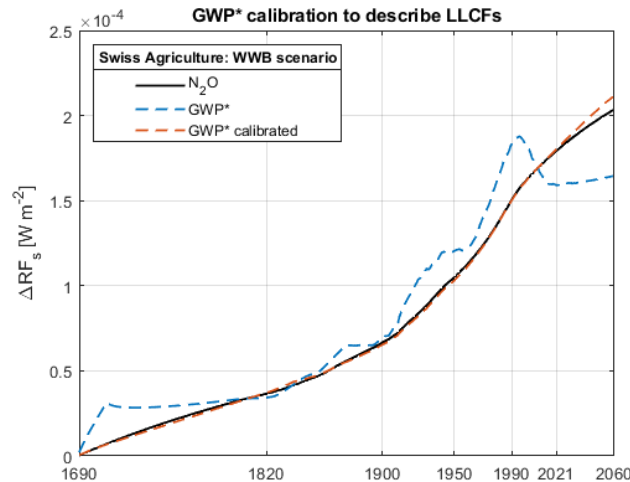
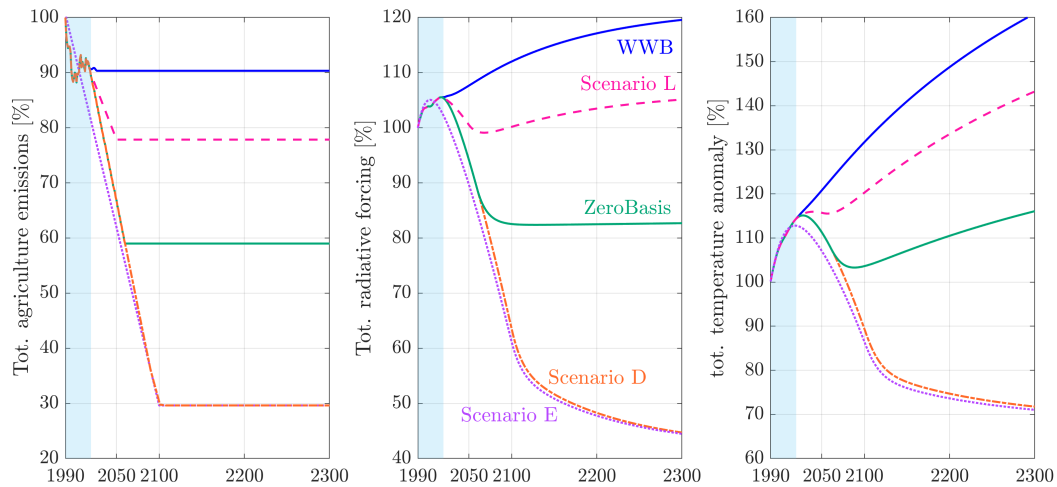


Figure 58. Improved fit of GWP* to the radiative forcing of LLCFs upon calibration as expressed by Table 7.

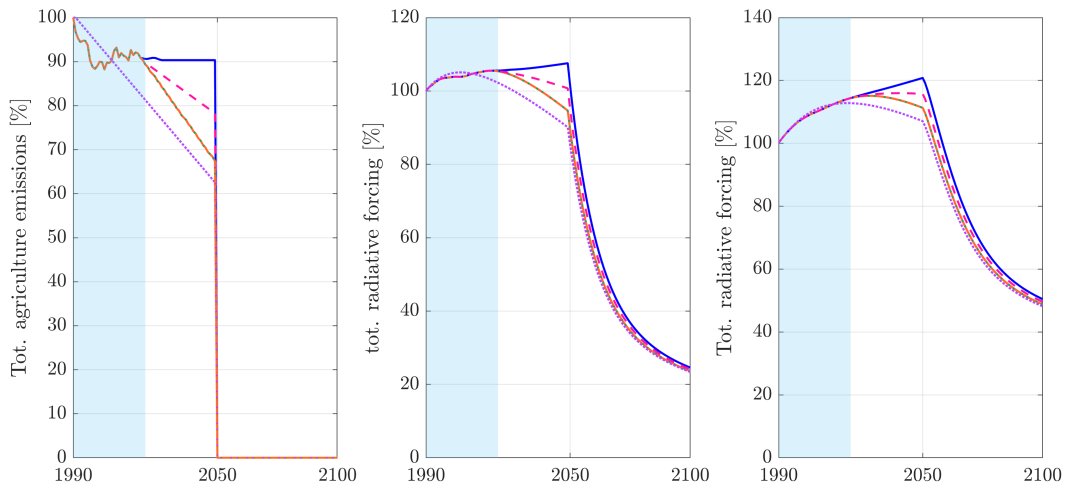
C Appendix Milestone 3

C.1 The rate of emissions decrease and the influence on peak warming

In this section we analyze, by means of simple curves, how the rate and beginning time of emissions reduction influence peak warming. The first plot (left-hand side) of Figure 59a exhibits five curves of agriculture GHG emissions reduction: the WWB (blue, solid line) and ZeroBasis (green, solid line) scenarios from the EP2050+, Scenario L ("Lower", pink, dashed line) where the emissions are reduced with a slower rate than in ZeroBasis, Scenario D ("Deeper", orange, dash-dotted line) where the emissions are reduced with the same rate as ZeroBasis but the emissions reduction continues until 2100, reaching a deeper absolute value, and Scenario E ("Early", purple, dotted line) where emissions reduction starts early (i.e., from 1990) proceeding at a steeper rate than the real, historical progression and linearly decreasing until emissions overlap with those of scenario D in 2100. The resulting forcing and temperature evolution curves are also shown.



(a) Analysis of the radiative forcing and temperature anomaly for emissions scenarios with different rates of reduction



(b) Employing a Target 2 policy scenario, where forcing is brought to net-zero in 2050, starting CDR deployment from that same year

Figure 59. The figure illustrates how the timing and rate of emissions reduction impact the peak warming, specifically in the context of Swiss agriculture-induced emissions. It demonstrates that if we would have followed a scenario with immediate emissions reduction (Scenario E) temperature anomaly would already have peaked. Conversely, a delay in reduction of emissions (and a lower rate of that), heightens and postpones the agriculture-induced peak warming. Adhering to the ZeroBasis projection of emissions reduction is now the only way to minimize the temperature peak.

In the WWB projection, GHG emissions remain constant after 2020, leading to a total forcing increase. This behavior can be divided into the methane and nitrous oxide contributions, where the concentration, and hence forcing, of CH_4 quickly adapts to changes in the emissions, following their trend, while the concentration of the longer-lived N_2O requires much longer to stabilize to changes in emissions, leading the increase seen in the total radiative forcing curve.

In the ZeroBasis projection, GHG emissions decrease until 2060 and remain constant afterwards. The total radiative forcing curves exhibits a similar behavior, as the N_2O forcing remains more or less constant in the ZeroBasis scenario, while that of CH_4 decreases following the trend in emissions of that GHG.

Conversely, the total radiative forcing of Scenario L decreases only momentarily, reaching a local minima, but later further increases approaching a steady state from below. The long term renewed increase in total forcing is driven by nitrous oxide. In fact, the reduction in N₂O emissions projected by Scenario L is not enough to stabilize the forcing (as occurs in the ZeroBasis), which instead keeps increasing. However, the local minima is driven by the methane forcing, as this decreases and then stabilizes following the emissions progression. As the forcing order of magnitude due to methane is greater than that of nitrous oxide, a local minima is generated following emissions reduction.

In the Scenario D and E projections, the total radiative forcing curves promptly decline following the emissions progressions, however further decreasing even after emissions have stabilized. In these scenarios, the sink in N₂O emissions is great enough to generate a decrease in the forcing of this GHG, which requires however more time to stabilize, therefore keeping the planetary system out of balance for longer.

The separate nitrous oxide and methane forcing contributions of the WWB, Zerobasis and Scenario D projections were previously discussed in Figure 5 and Figure 7 of Milestone 2.

The third chart on the right side of Figure 59a displays the temperature anomaly resulting from the various forcing evolutions. As previously discussed, temperature stabilization takes place over an extended timescale compared to the rate at which forcing adapts to perturbations. The data presented in this chart unmistakably illustrates that the projected reductions in emissions outlined in the WWB, Scenario L, and ZeroBasis scenarios are insufficient to arrest the upward trend in temperature. In fact, the temperature anomaly continues to rise over the long run in all these scenarios, ultimately reaching a stable state higher than current levels of warming.

The final temperature anomaly reached is determined by the level of final, constant forcing established by a given climate policy or emissions scenario. However, the timing and magnitude of the peak warming event are influenced by the initiation of emissions reduction and the rate at which it occurs. As demonstrated in Figure 59b, an earlier onset of emissions reduction leads to an earlier occurrence of peak warming. If the emissions trajectory of Scenario L had been followed, where emissions would have already experienced a consistent reduction since 1990, Swiss agriculture-induced warming would already be at its peak. In contrast, agriculture emissions remained more or less constant since 2000 and following the ZeroBasis scenario from now on, by means of emissions reduction or CDR deployment, is the only way to minimize the temperature peak. Instead, if we delay reduction, as in the case of the WWB scenario, and rely purely on CDR implementation from 2050, peak warming would increase by 10%.

However, even though the ZeroBasis scenario is the most effective in minimizing the temperature peak, it still falls short of achieving a sustained halt in warming. To achieve both a minimized peak warming and a steady-state temperature anomaly lower than current warming levels, a scenario with a similar rate of emissions reduction but greater absolute reduction (e.g., Scenario D) is required. The specific level of emissions reduction in this scenario depends on the climate policy's objective. For example, if the goal is long-term temperature stabilization at 1990 levels, the final constant forcing required by the climate policy can be calculated using Equation (26). The necessary emissions reduction can then be determined based on the composition of long-lived and short-lived climate forcers.

References

- (1) Neu, U. *Climate effect and CO₂ equivalent emissions of short-lived substances*; tech. rep. 5; Swiss Academy of Sciences (SCNAT), 2022, DOI: [10.5281/zenodo.6343974](https://doi.org/10.5281/zenodo.6343974).
- (2) Leach, N. J.; Jenkins, S.; Nicholls, Z.; Smith, C. J.; Lynch, J.; Cain, M.; Walsh, T.; Wu, B.; Tsutsui, J.; Allen, M. R. FaIRv2.0.0: a generalized impulse response model for climate uncertainty and future scenario exploration. *Geoscientific Model Development* **2021**, *14*, 3007–3036, DOI: [10.5194/gmd-14-3007-2021](https://doi.org/10.5194/gmd-14-3007-2021).
- (3) Smith, C. J.; Forster, P. M.; Allen, M.; Leach, N.; Millar, R. J.; Passerello, G. A.; Regayre, L. A. FAIR v1.3: a simple emissions-based impulse response and carbon cycle model. *Geoscientific Model Development* **2018**, *11*, 2273–2297, DOI: [10.5194/gmd-11-2273-2018](https://doi.org/10.5194/gmd-11-2273-2018).
- (4) Lee, D. et al. The contribution of global aviation to anthropogenic climate forcing for 2000 to 2018. *Atmospheric Environment* **2021**, *244*, 117834, DOI: [10.1016/j.atmosenv.2020.117834](https://doi.org/10.1016/j.atmosenv.2020.117834).
- (5) Brazzola, N.; Wohland, J.; Patt, A. Offsetting unabated agricultural emissions with CO₂ removal to achieve ambitious climate targets. *PLOS ONE* **2021**, *16*, ed. by Xu, Y., e0247887, DOI: [10.1371/journal.pone.0247887](https://doi.org/10.1371/journal.pone.0247887).
- (6) Sacchi, R.; Becattini, V.; Gabrielli, P.; et al. How to make climate-neutral aviation fly. *Nature Communication* **2023**, *14*, 3989.
- (7) Enting, I. Attribution of greenhouse gas emissions, concentrations and radiative forcing. *CSIRO Atmospheric Research technical paper* **1998**, 38.
- (8) Lightfoot, H. D.; Mamer, O. A. Calculation of Atmospheric Radiative Forcing (Warming Effect) of Carbon Dioxide at Any Concentration. *Energy Environment* **2014**, *25*, 1439–1454, DOI: <https://doi.org/10.1260/0958-305X.25.8.1439>.
- (9) Allen, M. R.; Friedlingstein, P.; Girardin, C. A.; Jenkins, S.; Malhi, Y.; Mitchell-Larson, E.; Peters, G. P.; Rajamani, L. Net Zero: Science, Origins, and Implications. *Annual Review of Environment and Resources* **2022**, *47*, 849–887, DOI: [10.1146/annurev-environ-112320-105050](https://doi.org/10.1146/annurev-environ-112320-105050).
- (10) Cain, M.; Lynch, J.; Allen, M. R.; Fuglestedt, J. S.; Frame, D. J.; Macey, A. H. Improved calculation of warming-equivalent emissions for short-lived climate pollutants. *npj Climate and Atmospheric Science* **2019**, *2*, 29, DOI: [10.1038/s41612-019-0086-4](https://doi.org/10.1038/s41612-019-0086-4).
- (11) Klöwer, M.; Allen, M. R.; Lee, D. S.; Proud, S. R.; Gallagher, L.; Skowron, A. Quantifying aviation's contribution to global warming. *Environmental Research Letters* **2021**, *16*, 104027, DOI: [10.1088/1748-9326/ac286e](https://doi.org/10.1088/1748-9326/ac286e).
- (12) Allen, M.; Tanaka, K.; Macey, A.; Cain, M.; Jenkins, S.; Lynch, J.; Smith, M. Ensuring that offsets and other internationally transferred mitigation outcomes contribute effectively to limiting global warming. *Environmental Research Letters* **2021**, *16*, 074009, DOI: [10.1088/1748-9326/abfcf9](https://doi.org/10.1088/1748-9326/abfcf9).
- (13) Geoffroy, O.; Saint-Martin, D.; Olivié, D. J. L.; Voltaire, A.; Bellon, G.; Tytéca, S. Transient Climate Response in a Two-Layer Energy-Balance Model. Part I: Analytical Solution and Parameter Calibration Using CMIP5 AOGCM Experiments. *Journal of Climate* **2012**, *26*, 1841–1857, DOI: [10.1175/JCLI-D-12-00195.1](https://doi.org/10.1175/JCLI-D-12-00195.1).
- (14) Myhre, G. et al. In *Climate Change 2013: The Physical Science Basis. Contribution of Working Group I to the Fifth Assessment Report of the Intergovernmental Panel on Climate Change: The Physical Science Basis. Contribution of Working Group I to the Fifth Assessment Report of*, Stocker, T., Qin, D., Plattner, G.-K., Tignor, M., Allen, S., Boschung, J., Nauels, A., Xia, Y., Bex, V., Migdley, P., Eds.; www.climatechange2013.org: 2013; Chapter 8, pp 1–44.
- (15) Boucher, O.; Reddy, M. Climate trade-off between black carbon and carbon dioxide emissions. *Energy Policy* **2008**, *36*, 193–200, DOI: [10.1016/j.enpol.2007.08.039](https://doi.org/10.1016/j.enpol.2007.08.039).

- (16) Shine, K. P.; Allan, R. P.; Collins, W. J.; Fuglestedt, J. S. Metrics for linking emissions of gases and aerosols to global precipitation changes. *Earth System Dynamics* **2015**, *6*, 525–540, DOI: 10.5194/esd-6-525-2015.
- (17) Tsutsui, J. Quantification of temperature response to carbon dioxide forcing in atmosphere–ocean general circulation models. *Climatic Change* **2017**, *140*, 287–305, DOI: <https://doi.org/10.1007/s10584-016-1832-9>.
- (18) Cummins, D. P.; Stephenson, D. B.; Stott, P. A. Optimal Estimation of Stochastic Energy Balance Model Parameters. *Journal of Climate* **2020**, *33*, 7909–7926, DOI: 10.1175/JCLI-D-19-0589.1.
- (19) Forster, P.; Storelvmo, T.; Armour, K.; Collins, W.; Dufresne, J.-L.; Frame, D.; Lunt, D.; Mauritsen, T.; Palmer, M.; Watanabe, M.; Wild, M.; Zhang, H. In *Climate Change 2021: The Physical Science Basis. Contribution of Working Group I to the Sixth Assessment Report of the Intergovernmental Panel on Climate Change*, Masson-Delmotte, V. et al., Eds.; Cambridge University Press: Cambridge, U.K., 2021; Chapter 7, pp 923–1054.
- (20) Für Energie (BFE), B. Energieperspektiven 2050+. **Last opened: 30.01.2023.**
- (21) Für Statistik (BFS), B. Schweizerische Zivilluftfahrtstatistik 2021 - 4. Bewegungen. **Last opened: 01.12.2022.**
- (22) N., W.; R., W.; J., R.; et al. Global warming overshoots increase risks of climate tipping cascades in a network model. *npj Climate and Atmospheric Science* **2022**, *13*, 75–82, DOI: 10.1038/s41558-022-01545-9.
- (23) O., H.-G. Metrics for linking emissions of gases and aerosols to global precipitation changes. *Earth System Dynamics* **2015**, *6*, 525–540, DOI: 10.5194/esd-6-525-2015.
- (24) Bericht des BAZL betreffend die Förderung der Entwicklung und des Einsatzes von nachhaltigen Flugtreibstoffen. *Bundesamt für Zivilluftfahrt (BAZL)* **2022**.
- (25) Riahi, K. et al. Mitigation pathways compatible with long-term goals. In IPCC, 2022: Climate Change 2022: Mitigation of Climate Change. Contribution of Working Group III to the Sixth Assessment Report of the Intergovernmental Panel on Climate Change. **2022**, DOI: 10.1017/9781009157926.005.
- (26) Joos, F. et al. Carbon dioxide and climate impulse response functions for the computation of greenhouse gas metrics: a multi-model analysis. *Atmospheric Chemistry and Physics* **2013**, *13*, 2793–2825, DOI: 10.5194/acp-13-2793-2013.
- (27) Shine, K. P.; Fuglestedt, J. S.; Hailemariam, K.; Stuber, N. Alternatives to the Global Warming Potential for Comparing Climate Impacts of Emissions of Greenhouse Gases. *Climatic Change* **2005**, *68*, 281–302, DOI: 10.1007/s10584-005-1146-9.
- (28) Ramaswamy, V.; Boucher, O.; Haigh, J.; Hauglustaine, D.; Haywood, G.; Myhre, G.; Nakajima, T.; Shi, G.; Solomon, S. In *Climate Change 2001: The Scientific Basis*, Joos, F., Srinivasan, J., Eds.; Cambridge University Press: Cambridge, U.K., 2001; Chapter 6, pp 349–416.
- (29) Myhre, G. et al. In *Climate Change 2013 – The Physical Science Basis*, Stocker, T., Qin, D., Plattner, G.-K., Tignor, M., Allen, S., Boschung, J., Nauels, A., Xia, Y., Bex, V., Migdley, P., Eds.; Cambridge University Press: Cambridge, U.K., 2013; Chapter 8, pp 659–740, DOI: 10.1017/CBO9781107415324.018.
- (30) Smith, C.; Nicholls, Z.; Armour, K.; Collins, W.; Forster, P.; Meinshausen, M.; Palmer, M.; Watanabe, M. *The Earth's Energy Budget, Climate Feedbacks, and Climate Sensitivity - Supplementary Material*; tech. rep.; IPCC, 2021.
- (31) Allen, M. R.; Shine, K. P.; Fuglestedt, J. S.; Millar, R. J.; Cain, M.; Frame, D. J.; Macey, A. H. A solution to the misrepresentations of CO₂-equivalent emissions of short-lived climate pollutants under ambitious mitigation. *npj Climate and Atmospheric Science* **2018**, *1*, 16, DOI: 10.1038/s41612-018-0026-8.

- (32) Smith, M. A.; Cain, M.; Allen, M. R. Further improvement of warming-equivalent emissions calculation. *npj Climate and Atmospheric Science* **2021**, *4*, 19, DOI: [10.1038/s41612-021-00169-8](https://doi.org/10.1038/s41612-021-00169-8).
- (33) Berntsen, T.; Fuglestvedt, J. Global temperature responses to current emissions from the transport sectors. *Proceedings of the National Academy of Sciences* **2008**, *105*, 19154–19159, DOI: [10.1073/pnas.0804844105](https://doi.org/10.1073/pnas.0804844105).